JETP Letters, Vol. 75, No. 12, 2002, pp. 605–609. Translated from Pis'ma v Zhurnal Éksperimental'noĭ i Teoreticheskoĭ Fiziki, Vol. 75, No. 12, 2002, pp. 729–733.

Measurement of the Neutron Interaction Time with Quantum Objects

A. I. Frank[1, *], I. V. Bondarenko[1], V. V. Vasil'ev[2], I. Anderson[3], G. Ehlers[3], and P. Hoghoj[3]

[1] *Frank Laboratory of Neutron Physics, Joint Institute for Nuclear Research, Dubna, Moscow region, 141980 Russia*

[2] *Institute for Theoretical and Experimental Physics, ul. Bol'shaya Cheremushkinskaya 25, Moscow, 117259 Russia*

[3] *Institut Laue–Langevin, BP 156-38042, Grenoble Cedex 9, France*

* *e-mail: frank@nf.jinr.ru*

Received April 29, 2002

The first experiments aimed at measuring neutron tunneling time in a quasi-bound resonance and Bragg diffraction time were carried out by the Larmor clock method. © *2002 MAIK "Nauka/Interperiodica".*

PACS numbers: 03.65.Xp; 03.75.Be

Interaction time and tunneling time. The problem of the interaction time in quantum mechanics has long been studied, at least theoretically. In the 1950s, Bohm [1] and Wigner [2] analyzed the problem of wave-packet interaction with an object on the basis of the causality principle. As a result, they obtained the following familiar formula for the packet delay time caused by interaction:

$$\Delta t = \hbar \frac{\partial \varphi}{\partial E}, \tag{1}$$

where φ is the phase shift of the particle wave function after the interaction act (scattering).

In 1966, Baz' analyzed theoretically the problem of scattering time for a particle in a three-dimensional potential. For a correct theoretical analysis of the problem, he suggested that spin precession in a constant magnetic field be used as a physically definite clock [3]. Then, Rybachenko used this concept in calculating the time of particle tunneling through a potential barrier [4]. Later, this problem was studied in numerous works. We refer to reviews [5, 6] and two recent papers [7, 8].

Baz's Larmor time is closely related to the Bohm–Wigner phase time (1). Indeed, the additional Larmor-precession angle caused by interaction can be identified with the phase difference $\Delta\varphi$ between two wave-function components corresponding to two spin z projections and differing in wavenumber:

$$k_\pm = k_0(1 \mp \mu B/E)^{1/2}, \quad E = \hbar^2 k_0^2/2m, \tag{2}$$

where k_0 is the neutron wavenumber in the absence of a field, μ is the magnetic moment, and B is the magnetic induction. According to Baz', we define the delay time associated with interaction as

$$\Delta t_\mathrm{L} = \Delta\varphi/\omega_\mathrm{L}, \quad \omega_\mathrm{L} = 2\mu B/\hbar, \tag{3}$$

where ω_L is the Larmor frequency. Then, taking into account that

$$2\mu B = \frac{\hbar^2}{2m}(k_+^2 - k_-^2) = \Delta E, \tag{4}$$

we arrive at the relationship

$$\Delta t_\mathrm{L} = \hbar \frac{\Delta\varphi}{\Delta E}, \tag{5}$$

coinciding with Eq. (1) in the limit $B \longrightarrow 0$.

Works [3, 4] are extensively cited in the studies of quantum interaction time, and the term "Larmor clock" has become common usage, although there has been some debate over the Larmor clock concept (see, e.g., [5, 9]).

Until recently, the problem of interaction time was investigated predominantly theoretically. The first experiments where light beams were used to measure tunneling time were carried out in the mid-1990s [10–12].

Experimental implementation of the Larmor clock concept in a neutron experiment faces considerable difficulties. In such an experiment, it is necessary to set off a relatively small factor $\omega_\mathrm{L}\tau$, where τ is the time of interaction with an object, against the background of a considerably greater velocity-dependent Larmor precession angle $\omega_\mathrm{L}(L/v)$, where L is the size of magnetic-field area and v is the neutron velocity.

The problem is solved by the so-called neutron spin echo method [13]. In this case, neutrons cover not one

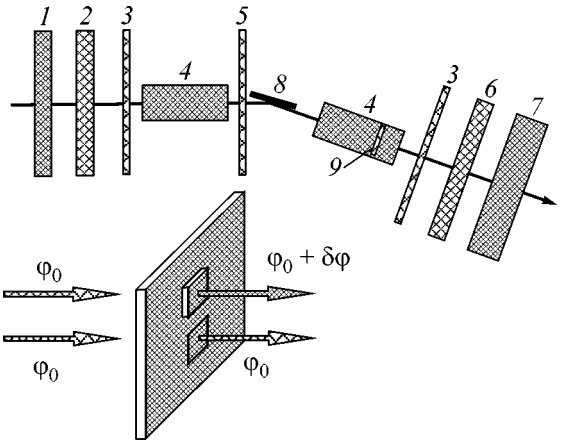

Fig. 1. Scheme of the experiment on the IN15 spectrometer: (*1*) velocity selector, (*2*) polarizer, (*3*) π/2 flippers, (*4*) precession solenoids, (*5*) π flipper, (*6*) polarization analyzer, (*7*) position-sensitive detector, (*8*) multilayer mirror monochromator, and (*9*) sample. The position of the sample in one of the two beams formed by the diaphragm is shown in the lower part of the figure.

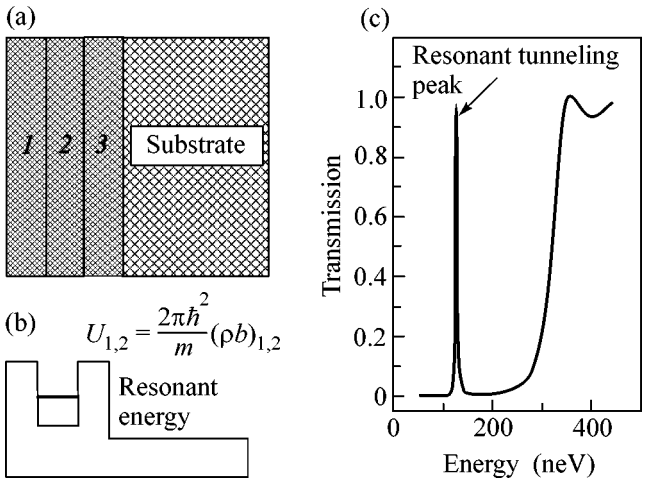

Fig. 2. Interference filter: (a) structure, (b) effective potential, and (c) transmission function.

but sequentially two flight bases $L_{1,2}$ with opposite directions of precession. If the neutron velocity is constant on the whole path and the condition

$$\int_{L_1} BDl = \int_{L_2} Bdl \qquad (6)$$

is met, the total Larmor phase on the path $L_1 + L_2$ becomes zero for any neutron velocity. A practical restriction on the monochromatization degree is imposed only by the degree of fulfillment of echo condition (6). The placement of a sample in one of the precession bases gives rise to a change in phase by $\omega_L\tau$.

The problem of interaction time was nearly solved by Hino *et al.* [14–16], who measured the additional precession angle arising when a sample under investigation was placed on the path of neutrons precessing in a magnetic field. However, the samples were ferromagnetic, and therefore the interpretation of the results in terms of interaction time is doubtful.

Experimental setup and method of measurement. We used the neutron spin-echo spectrometer IN15 of the Institute Laue–Langevin [17] to measure the neutron interaction time with objects. The experimental arrangement of the setup is shown in Fig. 1.

A sample was placed on the path of precessing neutrons inside a solenoid with a magnetic field. The precession phases were measured simultaneously in two beams, only one of which passed through the sample. To increase the reliability of measurements, the sample was periodically moved from one beam to the other. This method was previously used to measure the precession phase shift associated with the refraction in a sample [18, 19]. The high stability of the spectrometer and the two-beam technique allowed the phase shifts to be measured at a level of several degrees, and the accuracy of time measurement was 4×10^{-10} s.

Measurements of tunneling time in a quasi-bound resonance. The experiment was carried out with a so-called neutron interference filter consisting of three thin films applied on a substrate [20–22]. The interaction of long-wavelength neutrons with a substance is well described by the effective potential

$$U = \frac{2\pi\hbar^2}{m}\rho b,$$

where m is the neutron mass, ρ is the nuclear density, and b is the coherent-scattering length. Since the scattering length density ρb in the outer layers was larger than in the inner layer, the potential structure of the filter was a double humped barrier with a well in the middle. The choice of parameters ensured the existence of a quasi-bound state in this potential. In this case, the transmission function of the filter has a distinct resonance character (see Fig. 2).

We used a filter consisting of a Ti–Zr alloy film sandwiched between two Ni layers (doped with a small amount of solute nitrogen). The nitrogen dopant in nickel excluded its ferromagnetism. The filter was prepared by the method of magnetron sputtering onto a 0.6-mm-thick silicon substrate 150 mm in diameter. The thicknesses of the layers were 300–195–300 Å. The effective nickel potential is about 230 neV, whereas the effective potential of the Ti–Zr layer is close to zero. In this potential structure, there was only one resonance level with energy $E_0 \cong 127$ neV and a half width of 4 neV.

Measurements were carried out using cold neutrons with $\lambda = 20.1$ Å and the relative spectral halfwidth $\Delta\lambda/\lambda \cong 4.8\%$. Since the neutron energy was much higher than the filter resonance energy, the experiment was carried out in the grazing angle geometry. The sample was a stack of 32 individual filters of size 20 × 26 mm cut from one wafer after sputtering (see Fig. 3). The angular distribution of a beam with a calculated width of 3.2 mrad was formed by several slit diaphragms. The sample was situated into a precession coil in the position shown in Fig. 1. Neutrons with a zero angle of incidence can freely pass through the silicon substrate of the sample without touching the multilayer structure of the filter. With an increase in the grazing angle, the probability of the direct passage decreases and vanishes for $\tan\alpha \approx \alpha \approx d/L$, where d and L are the substrate thickness and length, respectively. In this case, neutrons, for which the resonance tunneling condition is not met, reflect from nickel films. As a result of reflection, they change their direction of motion and are easily separated from neutrons passed directly through the sample. With a further increase in the angle, secondary reflection from the nickel layer of the neighboring plate in the stack becomes possible. Doubly reflected neutrons leave the sample at the same angle as neutrons passed without reflection. They are indistinguishable from the latter neutrons and contribute to the background.

The count rate measured as a function of the grazing angle is shown in Fig. 4, where the minimum corresponds to the overlap angle of the direct beam. The increase in the count rate for large angles corresponds to the double reflection region. The results agree satisfactorily with the predictions. However, it was impossible to separate the resonance peak, whose calculated position was $\alpha_r = 24.8$ mrad, from the background in these measurements.

Nevertheless, the phase shift of neutron precession was measured over a relatively broad angular range (Fig. 5). The magnetic field on the sample was B = 190 G. As is seen in Fig. 5, the precession phase substantially increases near the expected resonance tunneling peak indicated by the arrow. The delay time at the maximum is equal to $(2.17 \pm 0.2) \times 10^{-7}$ s. For small angles corresponding to the direct passage, the delay time is close to a value of 1.9×10^{-8} s caused by the refraction in silicon.

Formula (1) yields 4.26×10^{-7} s for the tunneling time at the resonance maximum and 2.27×10^{-7} s for the time averaged over the transmission line. Thus, the experimental delay time agrees with the calculation within the experimental accuracy. It is highly probable that a considerable delay in the neutron-propagation time measured in the experiment is due precisely to the tunneling passage time in the quasi-bound resonance.

Experiment on measuring the Bragg diffraction time. In 1981, Baryshevskiĭ considered the problem of the diffraction of a neutron by a nonmagnetic crystal with allowance for the neutron spin precession in a constant magnetic field [23]. He found that the spin evolution in this case does not reduce to the simple Larmor precession and has a more complicated multifrequency character. Such a multifrequency precession has not yet

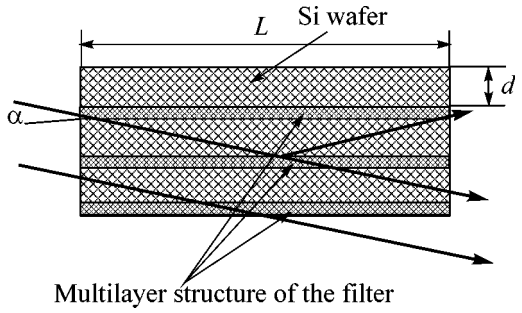

Fig. 3. Sample geometry in the tunneling time experiment.

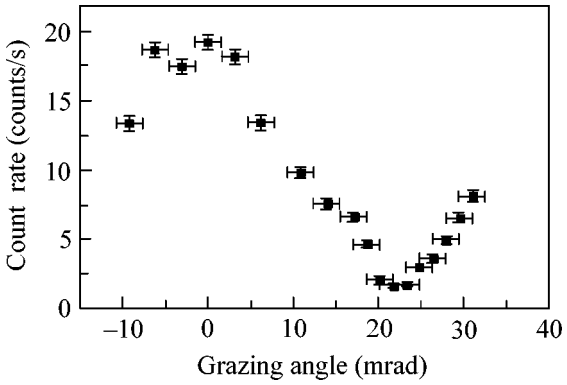

Fig. 4. Count rate vs. grazing angle in the tunneling time experiment.

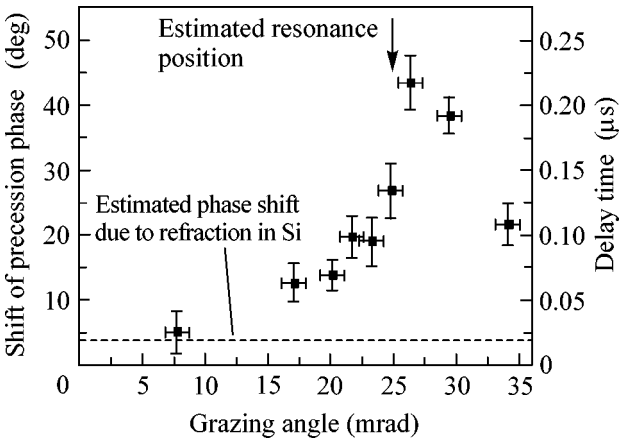

Fig. 5. Precession phase and delay time vs. grazing angle.

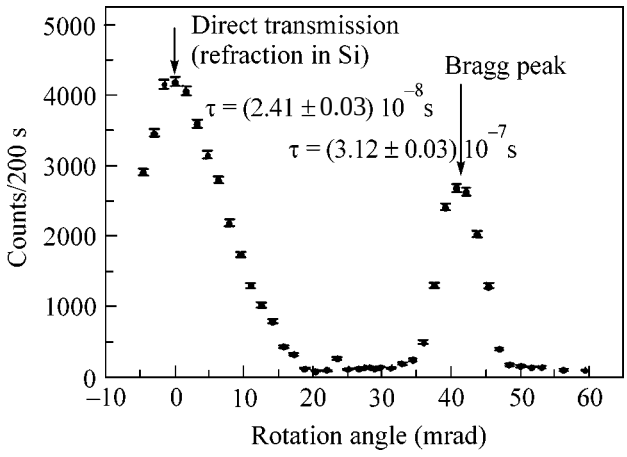

Fig. 6. Count rate vs. the rotation angle in the diffraction-time experiment. Delay times measured at two points are indicated by arrows.

been observed in neutron diffraction by a single crystal. Nevertheless, we attempted to carry out a similar experiment with an artificial one-dimensional "crystal"— a Bragg mirror. We note that, according to the aforesaid, the excess of the precession angle over the Larmor value can be related to the interaction time.

In this experiment, we again made use of a stack of samples each representing a silicon plates of size $0.7 \times 20 \times 35$ mm. Both sides of each plate were covered with a periodic thin-film structure consisting of 30 pairs of 130-Å-thick Ni–V alloy and 70-Å-thick Ti layers. This structure represents an interference mirror for neutrons with wavelengths 430–530 Å and an energy of 350 neV. The Ni–Ti film was covered with a 1000-Å-thick Gd film for the absorption of neutrons which were not reflected from the mirror. The plate length was chosen so that, if the Bragg condition was met, neutrons underwent two reflections before leaving the sample.

Measurements were made for wavelength $\lambda = 19.8$ Å ($\Delta\lambda/\lambda = 7.6\%$) and the results are shown in Fig. 6, where the right peak corresponds to the double Bragg reflection, whose calculated value is $\theta_B = 43$ mrad. The experimental value of the reflection coefficient at the peak is somewhat smaller than its theoretical value.

In the direct passage position, the delay time was equal to $(2.41 \pm 0.03) \times 10^{-8}$ s, which is close to a value of 2.37×10^{-8} s caused by the refraction in silicon. At the Bragg reflection peak, the delay time was $(3.12 \pm 0.03) \times 10^{-7}$ s.

DISCUSSION

We directly measured the extra precession phase arising when the sample under investigation was placed into a beam of precessing neutrons. On the basis of the Larmor-clock concept, we relate the detected phase shift to the delay time caused by the interaction time of a neutron wave with the object. In both experiments, the interaction time was found to be relatively long and was on the order of 0.2 μs. This is the time during which a neutron with a normal velocity component of several meters per second is localized in the interaction area with a size of about 10^{-5} cm. In the case of scattering through the quasi-bound state, the interaction time is of the same order as the state lifetime $\tau_r = \hbar/\Gamma$ but is not exactly equal to it. Here, $\Gamma \approx 4 \times 10^{-9}$ eV is the resonance width. In the diffraction experiment, the Bragg-peak width is $\Gamma \approx 10^{-7}$ eV. This corresponds to the resonance time $\tau_r \approx 7 \times 10^{-9}$ s, which is one-twentieth of the value measured in the experiment. However, this result is not as paradoxical as it may appear, because the quantity Δt entering the uncertainty relation $\Delta E \Delta t \geq \hbar$ is the uncertainty in the knowledge of the exact instant of collision and not of its duration (see, e.g., [24]).

We are grateful to V.E. Bunakov, V.G. Nosov, B. Farago, and G. Kali for stimulating discussions. This work was supported by the Russian Foundation for Basic Research (project no. 01-02-17005) and by INTAS (grant no. 00-00043).

REFERENCES

1. D. Bohm, *Quantum Theory* (Prentice-Hall, New York, 1951; Nauka, Moscow, 1965).
2. E. P. Wigner, Phys. Rev. **98**, 145 (1955).
3. A. I. Baz', Yad. Fiz. **4**, 252 (1966) [Sov. J. Nucl. Phys. **4**, 182 (1966)].
4. V. F. Rybachenko, Yad. Fiz. **5**, 895 (1967) [Sov. J. Nucl. Phys. **5**, 635 (1967)].
5. E. H. Hauge and J. A. Stovneng, Rev. Mod. Phys. **61**, 917 (1989).
6. R. Landauer and Th. Martin, Rev. Mod. Phys. **66**, 217 (1994).
7. C. R. Leavens and G. C. Aers, Phys. Rev. B **40**, 5387 (1989).
8. C. Bracher and M. Kleber, Ann. Physik (Leipzig) **4**, 696 (1995).
9. J. P. Falck and E. H. Hauge, Phys. Rev. B **38**, 3287 (1988).
10. P. Gueret, A. Baratoff, and E. Marclay, Europhys. Lett. **3**, 367 (1987).
11. M. Deutsch and J. E. Golub, Phys. Rev. A **53**, 434 (1996).
12. Ph. Balcou and L. Dutriaux, Phys. Rev. Lett. **78**, 851 (1997).
13. *Neutron Spin Echo*, Ed. by F. Mezei (Springer-Verlag, Heidelberg, 1980), Lecture Notes in Physics, Vol. 128.
14. M. Hino, N. Achiwa, S. Tasaki, *et al.*, Physica B (Amsterdam) **241–243**, 1083 (1998).
15. M. Hino, N. Achiwa, S. Tasaki, *et al.*, Phys. Rev. A **59**, 2261 (1999).
16. M. Hino, N. Achiwa, S. Tasaki, *et al.*, Phys. Rev. A **61**, 013607 (2000).

17. P. Schleger, B. Alefeld, J. F. Barthelemey, *et al.*, Physica B (Amsterdam) **241–243**, 164 (1998).
18. A. I. Frank, I. V. Bondarenko, A. V. Kozlov, *et al.*, in *Proceedings of the VIII International Seminar on Interactions of Neutrons with Nuclei (ISINN-8), Dubna, 2000*, E3-2000-192, p. 215.
19. A. I. Frank, I. V. Bondarenko, A. V. Kozlov, *et al.*, Physica B (Amsterdam) **297**, 307 (2001).
20. A. Steyerl, W. Drexel, S. S. Malik, and E. Gutsmiedle, Physica B (Amsterdam) **151**, 36 (1988).
21. I. V. Bondarenko, V. I. Bodnarchuk, S. N. Balashov, *et al.*, Yad. Fiz. **62**, 775 (1999) [Phys. At. Nucl. **62**, 721 (1999)].
22. I. V. Bondarenko, A. I. Frank, S. N. Balashov, *et al.*, Nucl. Instrum. Methods Phys. Res. A **440**, 591 (2000).
23. V. G. Baryshevskiĭ, Pis'ma Zh. Éksp. Teor. Fiz. **33**, 78 (1981) [JETP Lett. **33**, 74 (1981)].
24. A. I. Baz', Ya. B. Zel'dovich, and A. M. Perelomov, *Scattering, Reactions, and Decays in Nonrelativistic Quantum Mechanics* (Nauka, Moscow, 1966; Israel Program for Scientific Translations, Jerusalem, 1966).

Translated by R. Tyapaev

JETP Letters, Vol. 75, No. 12, 2002, pp. 610–616. From Pis'ma v Zhurnal Éksperimental'noĭ i Teoreticheskoĭ Fiziki, Vol. 75, No. 12, 2002, pp. 734–740.

QED Corrections to $\vec{A}(\vec{e}, e'B)X$ and $A(\vec{e}, e'\vec{B})X$ Reactions: The Case of Tensor Polarization[1]

G. I. Gakh and N. P. Merenkov

National Science Center "Kharkov Institute of Physics and Technology," 61108 Kharkov, Ukraine

Received May 13, 2002

The model-independent leading radiative corrections to polarization observables in semi-inclusive longitudinally polarized electron–nucleus scattering with the registration of a produced hadron and scattered electron in coincidence were calculated using the Drell–Yan representation in electrodynamics. The cases of a tensor-polarized target or a produced hadron with tensor polarization were considered. The exclusive process of the electrodisintegration of a polarized deuteron was also studied. © *2002 MAIK "Nauka/Interperiodica".*

PACS numbers: 25.30.Rw; 12.20.Ds; 13.88.+e

1. Over the last few years, much of the activity in QCD research has shifted from the determination of quark distribution functions and cross sections in leading order to the study of more detailed questions. This development was accompanied by an increased emphasis on semi-inclusive (SI) reactions [1]. As a result of this interest, some proposals for studying these phenomena have recently appeared. One of these is a new ELFE project [2]. ELFE (Electron Laboratory For Europe) is a project for developing a 15 to 30 GeV high-luminosity continuous-beam electron accelerator for scattering experiments from fixed nuclear targets. The goal of this project is to explore the quark and gluon structure of matter by exclusive and SI electron scattering from nuclei. The availability of polarized electron beam and targets is of particular importance for the investigation of the internal spin structure of hadrons, because the additional spin degrees of freedom allow one to isolate specific quark–gluon correlators and other higher twist matrix elements [3].

Some problems of electron–deuteron interaction can be investigated using tensor-polarized deuterons. Tensor-polarized deuteron targets have been designed in a number of laboratories. The polarization observables due to tensor polarization were measured in the elastic *ed* scattering [4]. The asymmetry in the reaction $\vec{d}\,(e, np)e'$ with a tensor-polarized deuteron was measured at Novosibirsk [5].

The significance of the tensor-polarized target in deep inelastic scattering (DIS) from the theoretical point of view was considered in [6]. The tensor structure functions in a polarized *pd* Drell–Yan process were investigated in [7].

Current experiments at modern accelerators reached a new level of precision, and this circumstance requires a new approach to data analysis and the inclusion of all possible systematic uncertainties. One important source of such uncertainties is the electromagnetic radiative effects caused by the physical processes which take place in higher orders of perturbation theory with respect to electromagnetic interaction. Earlier, we calculated the radiative corrections (RC) to the polarization observables in a DIS process (due to the tensor-polarized deuteron target) [8] and in an SI DIS process (due to the vector-polarized target or detected hadron with vector polarization) [9].[2]

In this paper, we give a covariant description of the polarization observables (due to the tensor polarization) in SI DIS of a longitudinally polarized electron beam off the tensor-polarized target (or production of tensor-polarized hadron)

$$e^-(k_1) + A(p_1) \longrightarrow e^-(k_2) + B(p_2) + X(p_x)\,, \qquad (1)$$

and we use the results obtained to calculate the model-independent QED RC by means of the electron structure function method using Drell–Yan representation [10] in electrodynamics.

We define the cross section for process (1), taking into account RC, in terms of the leptonic $L_{\mu\nu}$ and hadronic $H_{\mu\nu}$ tensors contraction

$$d\sigma = \frac{\alpha^2}{V(2\pi)^3}\frac{L_{\mu\nu}H_{\mu\nu}}{2q^4}\frac{d^3k_2}{\varepsilon_2}\frac{d^3p_2}{E_2}, \qquad (2)$$

where $V = 2k_1p_1$, ε_2 (E_2) is the energy of the scattered electron (detected particle B), and q is the 4-momentum of the virtual photon that probes the hadron block. Note that only in the Born approximation (without taking into account RC) $q = k_1 - k_2$. The hadronic tensor can be

[1] This article was submitted by the authors in English.

[2] Below, we will use notation **I** for [9].

0021-3640/02/7512-0610$22.00 © 2002 MAIK "Nauka/Interperiodica"

expressed via the hadron electromagnetic current J_μ of the $\gamma^*A \longrightarrow BX$ transition (γ^* is the virtual photon)

$$H_{\mu\nu} = \sum_X \langle p_1|J_\mu(q)|p_2, X\rangle\langle X, p_2|J_\nu(-q)|p_1\rangle \times \delta(p_x^2 - M_x^2),$$
$$p_x = q + p_1 - p_2,$$

where p_x (M_x) is the total 4-momentum (invariant mass) of the undetected hadron system.

By definition, the model-independent RC include the electromagnetic corrections to the leptonic piece of interaction only. Taking into account the leading contribution (terms proportional to $[\alpha\ln(Q^2/m_e^2)]^n$ in every order n of the perturbation theory), the leptonic tensor can be written in the standard form by means of the Drell–Yan representation in electrodynamics. This representation is defined by the double integral of the contraction of two electron-structure functions, which correspond to the radiation of the collinear photons and e^+e^- pairs by the initial and scattered electrons and the Born leptonic tensor $L^B_{\mu\nu}$, which depends on the scaled electron 4-momenta. For detail, see **I**, section 2.

Let us consider process (1) for the case of scattering off a tensor-polarized target (for example, deuteron target). The part of the hadronic tensor, which depends on the target quadrupole polarization tensor $Q_{\rho\sigma}$, can be written as

$$H_{\mu\nu} = H_{\mu\nu\rho\sigma}Q_{\rho\sigma},$$
$$\begin{aligned}H_{\mu\nu\rho\sigma} &= q_\rho q_\sigma[g_1\tilde g_{\mu\nu} + g_2\tilde p_{1\mu}\tilde p_{1\nu} + g_3\tilde p_{2\mu}\tilde p_{2\nu} + g_4(\tilde p_1\tilde p_2)_{\mu\nu} + ig_5[\tilde p_1\tilde p_2]_{\mu\nu}] + p_{2\rho}p_{2\sigma}[g_6\tilde g_{\mu\nu} + g_7\tilde p_{1\mu}\tilde p_{1\nu} + g_8\tilde p_{2\mu}\tilde p_{2\nu} + g_9(\tilde p_1\tilde p_2)_{\mu\nu} + ig_{10}[\tilde p_1\tilde p_2]_{\mu\nu}] \\ &+ (qp_2)_{\rho\sigma}[g_{11}\tilde g_{\mu\nu} + g_{12}\tilde p_{1\mu}\tilde p_{1\nu} + g_{13}\tilde p_{2\mu}\tilde p_{2\nu} + g_{14}(\tilde p_1\tilde p_2)_{\mu\nu} + ig_{15}[\tilde p_1\tilde p_2]_{\mu\nu}] \\ &+ (qN)_{\rho\sigma}[g_{16}(\tilde p_1 N)_{\mu\nu} + ig_{17}[\tilde p_1 N]_{\mu\nu} + g_{18}(\tilde p_2 N)_{\mu\nu} + ig_{19}[\tilde p_2 N]_{\mu\nu}] + (p_2N)_{\rho\sigma}[g_{20}(\tilde p_1 N)_{\mu\nu} + ig_{21}[\tilde p_1 N]_{\mu\nu} \\ &+ g_{22}(\tilde p_2 N)_{\mu\nu} + ig_{23}[\tilde p_2 N]_{\mu\nu}],\end{aligned} \quad (3)$$
$$N_\mu = \epsilon_{\mu\nu\rho\sigma}p_{1\nu}p_{2\rho}q_\sigma = (\mu p_1 p_2 q),$$
$$[ab]_{\mu\nu} = a_\mu b_\nu - a_\nu b_\mu, \quad (ab)_{\mu\nu} = a_\mu b_\nu + a_\nu b_\mu,$$
$$\tilde g_{\mu\nu} = g_{\mu\nu} - \frac{q_\mu q_\nu}{q^2}, \quad \tilde p_{i\mu} = p_{i\mu} - \frac{(qp_i)q_\mu}{q^2}, \quad i = 1, 2,$$

where g_i (i = 1–23) are the hadron semi-inclusive structure functions, which depend in general on four invariant variables. The set of these variables can be taken, for example, as q^2, (qp_1), (qp_2), and (p_1p_2).

We use the normalization of the tensor $Q_{\rho\sigma}$ such that the target spin-density matrix is defined as

$$\rho_{\rho\sigma} = -\frac{1}{3}\left(g_{\rho\sigma} - \frac{p_{1\rho}p_{1\sigma}}{M^2}\right) - \frac{i}{2M}\epsilon_{\rho\sigma\lambda\sigma}W_\lambda p_{1\delta} + Q_{\rho\sigma}, \quad (4)$$

where M (W_λ) is the target mass (polarization 4-vector). The quadrupole polarization tensor satisfies conditions $Q_{\rho\sigma} = Q_{\sigma\rho}$, $Q_{\rho\rho} = Q_{\rho\sigma}p_{1\sigma} = 0$.

In general, the traceless symmetrical tensor $Q_{\rho\sigma}$ has five independent components and is usually represented in the form

$$\begin{aligned}Q_{\rho\sigma} &= Q^{\alpha\beta}_{\rho\sigma}R_{\alpha\beta} = Q^{ll}_{\rho\sigma}R_{ll} \\ &+ Q^{tt-nn}_{\rho\sigma}R_{tt-nn} + Q^{lt}_{\rho\sigma}R_{lt} + Q^{ln}_{\rho\sigma}R_{ln} + Q^{tn}_{\rho\sigma}R_{tn}.\end{aligned} \quad (5)$$

Quantities $R_{\alpha\beta}$ on the right-hand side of Eq. (5) are the polarization degrees of the corresponding components $Q^{\alpha\beta}_{\rho\sigma}$. In the case of a polarized target, these quantities are specified by the procedure of the polarized-target preparation and do not depend on the reaction mechanism. On the contrary, the polarization characteristics of the final particles are determined by the reaction mechanism, and their measurement requires a second scattering from another target [11].

As concerns components $Q^{\alpha\beta}_{\rho\sigma}$, they can be represented as independent bilinear combinations of three mutually orthogonal 4-vectors, P^l (longitudinal), P^t (transversal), and P^n (normal), such that $(P^i)^2 = -1$, $P^ip_1 = 0$, $i = l, t, n$, namely,

$$\begin{aligned}Q^{ll}_{\rho\sigma} &= P^l_\rho P^l_\sigma - \frac{1}{2}(P^t_\rho P^t_\sigma + P^n_\rho P^n_\sigma), \\ Q^{tt-nn}_{\rho\sigma} &= \frac{1}{2}(P^t_\rho P^t_\sigma - P^n_\rho P^n_\sigma), \\ Q^{\alpha\beta}_{\rho\sigma} &= P^\alpha_\rho P^\beta_\sigma + P^\beta_\rho P^\alpha_\sigma \ \text{ if } \ \alpha \neq \beta.\end{aligned} \quad (6)$$

Due to the restriction on the spin-density matrix $\mathrm{Sp}\rho^2 \le (\mathrm{Sp}\rho)^2$, the following inequality has to be satisfied (compare with [12])

$$-\frac{W^2}{2} + \frac{3}{2}R^2_{ll} + \frac{1}{2}R^2_{tt-nn} + 2(R^2_{lt} + R^2_{ln} + R^2_{tn}) \le \frac{2}{3}. \quad (7)$$

In order to find the dependence of the cross section on the target tensor polarization, one has to use expansion (5) for $Q_{\rho\sigma}$ and then contract the hadronic and leptonic tensors in Eq. (2). For a covariant description of polarization phenomena with allowance for RC, it is convenient to parametrize the 4-vectors P^i in terms of the 4-momenta of particles participating in the process under consideration.

The use of a polarized Born cross section depending on the scaled electron 4-momenta under the integral in the Drell–Yan representation leads to some problems. It is clear that all components in expansion (5) are

attributes of the target only and cannot depend on radiation by the initial and scattered electrons. On the other hand, it may happen that in our theoretical calculations the 4-vectors P^i in Eq. (6), which are expressed through the 4-momenta, will change upon the scale transformation of the electron momenta: $k_{1,2} \longrightarrow \hat{k}_{1,2}$. Such a situation leads to the modification of $Q^{\alpha\beta}_{\rho\sigma}$, and we have to find a solution in this case.

For physical reasons, one can choose two different sets of 4-vectors P^i. For the first set (P^l, P^t, P^n), the longitudinal direction in the laboratory system is chosen along the 3-momentum of the initial electron, the transverse direction is in the plane ($\mathbf{k}_1$, $\mathbf{k}_2$), and the normal direction is perpendicular to the electron scattering plane. Note that the choice of two arbitrary vectors from the set defines also the choice of the third one. This set remains stabilized (not changed) under the scale transformation of the electron momenta, and the corresponding form of P^i is given by Eqs. (33) and (34) in **I**. In this case, there is no problem applying the ordinary Drell–Yan representation to the calculation of RC, and we have

$$\frac{d\sigma(k_1,k_2)}{d\Phi} = \iint \frac{dx_1dx_2}{x_2^2} D(x_1)D(x_2)\frac{d\sigma_B(\hat{k}_1,\hat{k}_2)}{d\hat{\Phi}}, \quad (8)$$
$$d\Phi = dxdydzdz_1dz_2,$$

where the notation for the kinematic variables and limits of integration is the same as in **I**. In the argument of the cross section, we omit those momenta which are not affected by the scale transformation. In accordance with expansion (5), the Born cross section in the integrand in the right-hand side of Eq. (8) reads

$$\frac{d\sigma_B(k_1,k_2)}{d\Phi} = Z[P_{ll}R_{ll} + P_{tt-nn}R_{tt-nn} + P_{lt}R_{lt} + P_{ln}R_{ln} + P_{tn}R_{tn}], \quad Z = \frac{\alpha^2 y V^6}{128\pi^2|\eta|Q^4}, \quad (9)$$

where

$$P_{ll} = 3\eta[(2\tau_1 z_1 - z)R_{20} - (y+2a)R_{16}] + \frac{1}{V^2\tau_1}[[(y+2a)^2 - 2ab]G_1 + [6\tau_1 z_1(\tau_1 z_1 - z) + 2\tau_1\tau_2 + z^2]G_6 - 2[\tau_1 z_2 + \tau_1 z_1(3a-3b+2) - z(y+3a)]G_{11}],$$

$$P_{lt} = \frac{1}{\sqrt{ab}}\Big[(2\tau_1 z_1 - z)\Big[\frac{2}{V^2}(\eta_2 G_6 + 2xybG_{11}) + \eta(y+2a)R_{20}\Big] - (y+2a)\Big[\frac{2}{V^2}(\eta_2 G_{11} + 2xybG_1) + \eta(y+2a)R_{16}\Big] + 2\eta\tau_1(\eta_2 R_{20} + 2xybR_{16})\Big],$$

$$P_{tt-nn} = \eta(y+2a)R_{16} + \frac{2}{V^2}(xybG_1 + \eta_2 G_{11}) + \frac{1}{2xyb}\Big[\eta(\eta_2(y+2a)+\eta_1)R_{20} + \frac{\eta_2^2 - \eta^2}{V^2}G_6\Big],$$

$$P_{ln} = \frac{-1}{\sqrt{ab}}\Big[(2\tau_1 z_1 - z)\Big(\frac{2}{V^2}\eta G_6 - \eta_1 R_{20}\Big) + (y+2a)\Big(\eta_1 R_{16} - \frac{2}{V^2}\eta G_{11}\Big) + 2\tau_1\eta^2 R_{20}\Big],$$

$$P_{tn} = 2\eta_1 R_{16} - \frac{4}{V^2}\eta G_{11} - \frac{\tau_1}{ab}\Big[\eta_2\Big(\frac{2}{V^2}\eta G_6 - \eta_1 R_{20}\Big) + \eta^2(y+2a)R_{20}\Big],$$

$$G_i = -2\frac{xy}{V}g_i + bg_{i+1} + (z_1 z_2 - \tau_2 xy)g_{i+2} + [z_2 + (1-y)z_1 - xyz]g_{i+3} - \lambda\eta g_{i+4},$$

$$R_i = \frac{\eta}{2}[(2-y)g_i + (z_1+z_2)g_{i+2}] + \frac{\lambda}{2}(\eta_1 g_{i+1} + \eta_3 g_{i+3}),$$

$$a = xy\tau_1, \quad b = 1 - y - a,$$

$$\eta_1 = y[z_2 - z_1(1-y) - xz(2-y) + 2x\tau_1(z_1+z_2)],$$

$$\eta_2 = z_2 + (1-y)z_1 - xyz - 2bz_1,$$

$$\eta_3 = (z_1 - z_2)[z_2 - z_1(1-y)] - xy[2\tau_2(2-y) - z(z_1+z_2)].$$

For the second set (P^L, P^T, $P^N = P^n$), the longitudinal (L) direction is chosen along the 3-momentum $\mathbf{q}$ of the intermediate heavy photon in the laboratory system, and the transverse direction is in the electron scattering plane. The specific form of this set is defined by Eq. (35) in **I**. Under the scale transformation of the electron momenta, the 4-vectors P^L and P^T begin to rotate in the electron scattering plane, because direction $\mathbf{q}$ is unstable.

To compute RC in this case, one needs to express these unstable 4-vectors through the stabilized ones P^l and P^t. The relation between them is given by the orthogonal matrix [see Eq. (36) in **I**]. The elements of this matrix are not affected by the scale transformation,

and we derive the modified Drell–Yan representation, which is a direct analog of Eq. (30) in [8],

$$\frac{d\sigma^u(k_1,k_2)}{d\Phi} = X_{\alpha\beta}(k_1,k_2) \times \int\int \frac{dx_1dx_2}{x_2^2} D(x_1)D(x_2)\frac{d\sigma_B^{\alpha\beta}(\hat{k}_1,\hat{k}_2)}{d\hat{\Phi}}, \quad (10)$$

where we use the upper index u to indicate that the target quadrupole polarization tensor is defined with respect to the unstable directions, and the summation over indices α and β is borne in mind. The principle moment of this modified representation is the appearance of the matrix $X_{\alpha\beta}(k_1, k_2)$ ahead of the integral, which depends on the nonscaled electron momenta. The elements X_{ll}, X_{tt}, and X_{lt} are the same as in Eq. (31) in [8], and the remaining ones have the very simple form

$$X_{ln} = \cos\theta_1 R_{LN} - \sin\theta_1 R_{TN},$$
$$X_{tn} = \cos\theta_1 R_{TN} + \sin\theta_1 R_{LN},$$
$$\cos\theta_1 = \frac{y(1+2x\tau_1)}{\sqrt{y(y+4x\tau_1)}}, \quad (11)$$

where R_{AB} are the polarization degrees of corresponding components of the tensor polarization defined with respect to the directions L, T, and N.

The partial cross sections under the integral sign in the right-hand side of Eq. (10) read

$$\frac{d\sigma_B^{\alpha\beta}(k_1,k_2)}{d\Phi} = ZP_{\alpha\beta}, \quad (12)$$

where the quantities $P_{\alpha\beta}$ are given after Eq. (9).

To obtain the Born approximation for the cross section on the left-hand side of Eq. (10), it is enough to substitute the ordinary δ function instead of the electron-structure functions in the integrand, and such procedure leads to the following result

$$\frac{d\sigma_B^u(k_1,k_2)}{d\Phi} = Z[P_{LL}R_{LL} + P_{TT-NN}R_{TT-NN} + P_{LT}R_{LT} + P_{LN}R_{LN} + P_{TN}R_{TN}], \quad (13)$$

where

$$P_{LL} = \frac{1}{\tau_1 V^2}[yhG_1 - 2G_{11}(2\tau_1(z_1-z_2)-yz) + \frac{G_6}{yh}\left((2\tau_1(z_1-z_2)-yz)^2 - \frac{\tau_1}{2xb}\left(h\eta^2 + \frac{\eta_1^2}{y}\right)\right)],$$

$$P_{LT} = \frac{1}{h\sqrt{ab}}\left[(2\tau_1(z_1-z_2)-yz)\left(\frac{2\eta_1 G_6}{yV^2} + h\eta R_{20}\right) - yh\left(\frac{2\eta_1 G_{11}}{yV^2} + h\eta R_{16}\right)\right],$$

$$P_{TT-NN} = \frac{1}{2xybh}\left[\left(\frac{\eta_1^2}{y} - h\eta^2\right)\frac{G_6}{V^2} + 2h\eta\eta_1 R_{20}\right],$$

$$P_{LN} = \frac{1}{y\sqrt{\tau_1 xbh}}\left[yh\left(\frac{2\eta G_{11}}{V^2} - \eta_1 R_{16}\right) - (2\tau_1(z_1-z_2)-yz)\left(\frac{2\eta G_6}{V^2} - \eta_1 R_{20}\right)\right],$$

$$P_{TN} = -\frac{1}{xb\sqrt{yh}}\left[2\eta\eta_1\frac{G_6}{yV^2} + \left(h\eta^2 - \frac{\eta_1^2}{y}\right)R_{20}\right].$$

It is easy to verify that the straightforward calculation based on the expansion of the tensor polarization by means of the set (P^L, P^T, P^N) gives the same answer.

Note that the Born cross section (13), when the tensor polarization components are defined relative to unstable (under scale transformation) directions, is simpler compared to cross section (9), if these components are defined with respect to stabilized ones. Allowing for RC changes the situation radically. In the last case, it is trivial because the RC does not mix different components. By contrast, in the first case the radiation of particles by electrons leads to a mixture of tensor-polarization components due to the rotation of P^L and P^T; therefore, the *RC* is more complicated.

2. Let us consider the tensor polarization of the detected particle B in process (1) provided with an unpolarized target A. In this case, all tensor-polarization degrees $R_{\alpha\beta}$ are defined by the reaction mechanism and can be measured in the second scattering (see, for example, [11], where the elastic electron–deuteron scattering with polarization transfer from electron to scattered deuteron was investigated).

Hadronic tensor $H_{\mu\nu}^{\alpha\beta}$ corresponding to the given polarization $R_{\alpha\beta}$ can easily be constructed using tensor $H_{\mu\nu}$ defined by Eq. (3). In order to do this, it is enough to change expressions $Q_{\rho\sigma}p_{2\rho}p_{2\sigma}$, $Q_{\rho\sigma}(qp_2)_{\rho\sigma}$, and $Q_{\rho\sigma}(p_2N)_{\rho\sigma}$ in $H_{\mu\nu}$ by $V_{\rho\sigma}^{\alpha\beta}p_{1\rho}p_{1\sigma}$, $V_{\rho\sigma}^{\alpha\beta}(qp_1)_{\rho\sigma}$, and $V_{\rho\sigma}^{\alpha\beta}(qp_1)_{\rho\sigma}$, respectively, where $V_{\rho\sigma}^{\alpha\beta}$ is the component of the final-particle quadrupole polarization tensor $V_{\rho\sigma}$ in expansion $V_{\rho\sigma} = V_{\rho\sigma}^{\alpha\beta}R_{\alpha\beta}$. This is an analog of the respective expansion for the target quadrupole polarization tensor. Besides, one needs to use another notation for the hadronic structure functions, $g_i \longrightarrow f_i$, $i = 1$–23, because, in general, they are different.

The given tensor polarization $R_{\alpha\beta}$ of the particle B is, by definition, the ratio of the partial cross section $d\sigma^{\alpha\beta}$, which can be derived by contraction of the leptonic tensor with $H^{\alpha\beta}_{\mu\nu}$, to the unpolarized cross section

$$R_{\alpha\beta} = d\sigma^{\alpha\beta}/d\sigma_{(un)}. \tag{14}$$

In the approximation used, RC to the unpolarized cross section is defined by Eq. (19) in **I**; therefore, our problem is the calculation of RC to the partial cross section. By full analogy with Eq. (6), components $V^{\alpha\beta}_{\rho\sigma}$ represent traceless independent bilinear combinations of three mutually orthogonal 4-vectors S^i, which satisfy conditions $(S^i)^2 = -1$, $S^i p_2 = 0$, $i = l, t, n$. If we take the longitudinal direction in the rest frame of the detected hadron opposite to the direction of 3-momentum $\mathbf{p}_1$, and if the transverse direction is in the plane $(\mathbf{k}_1, \mathbf{p}_1)$ (or in the plane $(\mathbf{k}_1, \mathbf{p}_2)$ in the laboratory system), the set (S^l, S^t, S^n) remains stabilized under the scale transformation of the electron momenta. The form of this set in terms of the 4-momenta is defined by Eqs. (14) and (15) in **I**, and the Drell–Yan representation of the partial cross section in this case reads

$$\frac{d\sigma^{\alpha\beta}(k_1, k_2)}{d\Phi} = \iint \frac{dx_1 dx_2}{x_2^2} D(x_1) D(x_2) \frac{d\sigma_B^{\alpha\beta}(\hat{k}_1, \hat{k}_2)}{d\hat{\Phi}},$$

$$\frac{d\sigma_B^{\alpha\beta}(k_1, k_2)}{d\Phi} = \frac{Z}{(2S_A + 1)} S^{\alpha\beta},$$

$$S_{ll} = \frac{1}{V^2\tau_2}[2[z(z_1 - z_2) - 2y\tau_2]H_{11} + d_1^2 H_6]$$

$$+ \frac{H_1}{2V^2 d_1^2}\left[\frac{2}{\tau_2}[z(z_1 - z_2) - 2y\tau_2]^2 - \frac{\eta_4^2 + \eta^2 d_1^2}{d_2^2}\right],$$

$$S_{lt} = \frac{1}{d_1^2 d_2 \sqrt{\tau_2}}\left[[z(z_1 - z_2) - 2y\tau_2]\left(\frac{2}{V^2}\eta_4 H_1 + \eta d_1^2 F_{16}\right)\right.$$

$$\left. + d_1^2\left(\frac{2}{V^2}\eta_4 H_{11} + \eta d_1^2 F_{20}\right)\right],$$

$$S_{tt-nn} = \frac{1}{2d_2^2}\left(2\eta\eta_4 F_{16} + \frac{\eta_4^2 - \eta^2 d_1^2}{V^2 d_1^2} H_1\right),$$

$$S_{ln} = \frac{1}{d_1 d_2 \sqrt{\tau_2}}\left[d_1^2\left(\frac{2}{V^2}\eta H_{11} - \eta_4 F_{20}\right)\right.$$

$$\left. + [z(z_1 - z_2) - 2y\tau_2]\left(\frac{2}{V^2}\eta H_1 - \eta_4 F_{16}\right)\right],$$

$$S_{tn} = \frac{1}{d_1 d_2^2}\left[\frac{2}{V^2}\eta\eta_4 H_1 - (\eta_4^2 - \eta^2 d_1^2)F_{16}\right], \tag{15}$$

$$H_i = G_i(g_k \longrightarrow f_k), \quad F_i = R_i(g_k \longrightarrow f_k),$$

$$d_1^2 = z^2 - 4\tau_1\tau_2, \quad d_2^2 = zz_1 - \tau_2 - z_1^2\tau_1,$$

$$\eta_4 = 2y\tau_2 - z(z_1 - z_2) - xy(z^2 - 4\tau_1\tau_2)$$
$$+ z_1[2\tau_1(z_1 - z_2) - yz],$$

where S_A is the target spin.

If the longitudinal direction is the same ($L = l$) but the transversal one (T) is chosen in the plane $(\mathbf{q}, \mathbf{p}_1)$ in the rest frame of the detected hadron (or in the plane $(\mathbf{q}, \mathbf{p}_2)$ in the laboratory system), the new set ($S^L = S^l$, S^T, S^N) has become unstable under substitution $k_{1,2} \longrightarrow \hat{k}_{1,2}$. It means physically that collinear radiation changes the direction of $\mathbf{q}$, and this leads to the rotation of vectors S^T and S^N around the longitudinal direction, which remains unchanged. The form of the 4-vectors S^T and S^N is defined by Eq. (17) in **I**. In this case we will use capital letters to label the tensor polarizations of the detected hadron and the respective partial cross sections

$$R_{AB} = d\sigma^{AB}/d\sigma_{(un)}. \tag{16}$$

To compute RC to the partial cross sections, one needs, as before, to express S^T and S^N through stabilized 4-vectors S^t and S^n. The relation between these 4-vectors is given by the orthogonal matrix [see Eq. (18) in **I**]. Then, it is necessary to find matrix Y which relates unstable $V^{AB}_{\rho\sigma}$ and stabilized $V^{\alpha\beta}_{\rho\sigma}$ components of the quadrupole polarization tensor to each other,

$$V^{AB}_{\rho\sigma} = Y^{AB}_{\alpha\beta} V^{\alpha\beta}_{\rho\sigma}. \tag{17}$$

The nonzero elements of the matrix Y are

$$Y_{ll}^{LL} = 1, \quad Y_{lt}^{LT} = Y_{ln}^{LN} = \cos\theta,$$

$$Y_{lt}^{LN} = -Y_{ln}^{LT} = \sin\theta,$$

$$Y_{tn}^{TN} = Y_{tt-nn}^{TT-NN} = \cos 2\theta,$$

$$Y_{tt-nn}^{TN} = -4Y_{tn}^{TT-NN} = 2\sin 2\theta, \tag{18}$$

$$\cos\theta = -\frac{\eta_4}{2d_2 d_3},$$

$$d_3^2 = zy(z_1 - z_2) + xyd_1^2 - (z_1 - z_2)^2\tau_1 - y^2\tau_2.$$

The Drell–Yan representation for the partial cross sections has the modified form

$$\frac{d\sigma^{AB}(k_1, k_2)}{d\Phi} = Y^{AB}_{\alpha\beta}(k_1, k_2)$$
$$\times \iint \frac{dx_1 dx_2}{x_2^2} D(x_1) D(x_2) \frac{d\sigma_B^{\alpha\beta}(\hat{k}_1, \hat{k}_2)}{d\hat{\Phi}}, \tag{19}$$

where the elements of the matrix Y depend on the nonscaled electron momenta, and the Born cross sections under the integral are defined by Eqs. (15).

To obtain the Born form of the partial cross sections on the left-hand side of Eq. (19), one can use δ function instead of D functions under the integral sign. Such a procedure gives

$$\frac{d\sigma_B^{AB}}{d\Phi}(k_1, k_2) = \frac{Z}{2S_A+1}S_{AB},$$

$$S_{LL} = S_{ll},$$

$$S_{LT} = -\frac{4d_3}{V^2 d_1^2\sqrt{\tau_2}}[(z(z_1-z_2)-2y\tau_2)H_1 + d_1^2 H_{11}], \quad (20)$$

$$S_{LN} = \frac{2d_3}{d_1\sqrt{\tau_2}}[(z(z_1-z_2)-2y\tau_2)F_{16} + d_1^2 F_{20}],$$

$$S_{TT-NN} = \frac{2d_3^2}{d_1^2 V^2}H_1, \quad S_{TN} = -4\frac{d_3^2}{d_1}F_{16}.$$

As in the case of the polarized target, the partial Born cross sections for unstable directions are simpler, but allowing for RC takes away the whole simplicity.

3. Consider now the special case of reaction (1), namely, the disintegration of polarized deuterons by longitudinally polarized electrons for an exclusive setup. In this case, the outgoing proton is detected in coincidence with the scattered electron, and the lost invariant mass is smaller than $m + m_\pi$; therefore, the undetected hadronic state X consists only of a neutron.

Theoretically, the problems of polarization phenomena caused by a tensor-polarized target in $\vec{d}(\vec{e}, e'p)n$ reactions were investigated in a number of papers. For detail, see review [13]. The experimental study of polarized exclusive deuteron disintegration is planned at future upgraded version of CEBAF at Jefferson Laboratory [14]. This will provide a test for the basic principles of our understanding of the electrodisintegration dynamics. Progress in constructing tensor-polarized deuteron targets will make it feasible to study reactions at sufficiently large Q^2. In this case, a direct separation of S- and D-wave contributions is possible, which is important for the understanding of short-distance NN interactions [15].

Our aim is to show how to calculate the model-independent RC for the process considered here. It is obvious that we have to use standard or modified Drell–Yan representation [like Eq. (8) or (10) for a semi-inclusive DIS process]. So, knowledge of the respective partial Born cross sections in terms of used invariant variables is necessary. One can derive them using the δ function in the definition of the hadronic tensor $H_{\mu\nu}$ to remove the integration with respect to z_2 in Eq. (12). Therefore, for the exclusive partial cross sections, we can use Eq. (12) with substitution $d\Phi \longrightarrow dxdydzdz_1$ in the left-hand side and $g_i \longrightarrow h_i/V$, $z_2 \longrightarrow z_1 + z - y(1-x) - \tau_1$ in the right-hand side, where h_i are structure functions of the deuteron electrodisintegration.

On the other hand, in the literature special kinematic variables are used. They are suitable for separation of the contributions into cross section caused by the longitudinal and transverse polarizations (and their interference) of the intermediate heavy photon. These are the energy ε_2 and the polar angle θ_2 of the scattered electron in the laboratory system [with the z axis along $\mathbf{q}$ and the x axis in plane ($\mathbf{q}$, $\mathbf{p}_2$)], the angle ϕ between the electron scattering plane and plane ($\mathbf{q}$, $\mathbf{p}_2$), and the proton scattering angle θ in c.m.s. of the reaction $\gamma^* + d \longrightarrow p + n$. In terms of these variables, the Born cross section looks as follows:

$$\frac{d\sigma}{d\varepsilon_2 d\cos\theta_2 d\phi d\cos\theta} = F\Big[h_{xx} + h_{yy} + \varepsilon\cos 2\phi(h_{xx} - h_{yy}) + \varepsilon\sin 2\phi(h_{xy} + h_{yx}) - 2\varepsilon\frac{q^2}{q_0^2}h_{zz} - \sqrt{2\varepsilon(1+\varepsilon)}\frac{\sqrt{-q^2}}{q_0} \times [\cos\phi(h_{xz} + h_{zx}) + \sin\phi(h_{yz} + h_{zy})] - i\lambda\sqrt{(1-\varepsilon^2)}(h_{xy} - h_{yx}) - i\lambda\sqrt{2\varepsilon(1-\varepsilon)}\frac{\sqrt{-q^2}}{q_0} \times [\cos\phi(h_{yz} - h_{zy}) - \sin\phi(h_{xz} - h_{zx})]\Big], \quad (21)$$

$$F = \frac{\alpha^2}{32\pi^2}\frac{\varepsilon_2}{\varepsilon_1}\frac{|\mathbf{p}_2|}{MW}\frac{(1-\varepsilon)^{-1}}{(-q^2)}, \quad \varepsilon^{-1} = 1 - 2\frac{\mathbf{q}_L^2}{q^2}\tan^2\left(\frac{\theta_e}{2}\right),$$

where θ_e and $\mathbf{q}_L$ are the scattering angle of the electron and virtual-photon 3-momentum in laboratory system, W is the total invariant energy of system p–n, q_0 and $\mathbf{p}_2$ are the virtual-photon energy and 3-momentum of the detected proton in c.m.s., and λ is the degree of the longitudinal polarization of the electron beam. The quantity ε represents the degree of the virtual-photon linear polarization. This formula is obtained in the one-photon-exchange approximation using the conservation of the electromagnetic current describing the $\gamma^* d \longrightarrow pn$ transition and P invariance of the hadron electromagnetic interaction.

The hadronic tensor $h_{\mu\nu}$ can be derived from $H_{\mu\nu}$ by the rule

$$H_{\mu\nu} \longrightarrow \frac{1}{V}h_{\mu\nu}\delta(z_2 - z_1 - z + y(1-x) + \tau_1), \quad g_i \longrightarrow h_i, \quad (22)$$

and its components have to be written in c.m.s.

To use the Drell–Yan representation, we have to express all variables and quantities in both sides of

Eq. (21) through invariant variables. The corresponding formulas read

$$Fd\varepsilon_2 d\cos\theta_2 d\phi d\cos\theta = \frac{\alpha^2}{32\pi^2}$$

$$\times \frac{[1+(1-y)^2+2xy\tau_1](1+2x\tau_1)}{xyV|\eta|(y+4x\tau_1)^2\sqrt{y(y+4x\tau_1)}} dxdydzdz_1,$$

$$W = \sqrt{V(\tau_1+y-xy)},$$

$$|\mathbf{p}_2| = \frac{1}{2}\sqrt{V(\tau_1-4\tau_2+y-xy)},$$

$$\mathbf{q}^2 = \frac{Vy(y+4x\tau_1)}{4(\tau_1+y-xy)},$$

$$q^2 = -xyV, \quad q_0 = \frac{1-2x}{2}\sqrt{\frac{Vy^2}{\tau_1+y(1-x)}},$$

$$\varepsilon = \frac{2(1-y-xy\tau_1)}{1+(1-y)^2+2xy\tau_1},$$

$$\cos\theta = \frac{2z-y-2\tau_1}{\sqrt{\tau_1-4\tau_2+y(1-x)}}\sqrt{\frac{\tau_1+y(1-x)}{y(y+4x\tau_1)}},$$

$$\cos\theta_2 = \frac{y(1-y-2x\tau_1)}{(1-y)\sqrt{y(y+4x\tau_1)}},$$

and the azimuthal angle ϕ can be obtained from the equation

$$\sin\phi = -\frac{\eta}{\sin\theta}$$

$$\times \frac{1}{\sqrt{xy(1-y-xy\tau_1)(\tau_1-4\tau_2+y-xy)}}.$$

The components of the hadronic tensor on the right-hand side of Eq. (21) can easily be written taking into account that in c.m.s.

$$q_z = -p_{1z} = |\mathbf{q}|, \quad p_{2z} = |\mathbf{p}_2|\cos\theta,$$

$$p_{2x} = |\mathbf{p}_2|\sin\theta, \quad N_y = W|\mathbf{p}_2||\mathbf{q}|\sin\theta,$$

and all other components of the corresponding 3-vectors are zeros.

REFERENCES

1. A. Schafer, Nucl. Phys. A **622**, 357c (1997).
2. H. Burkhardt (Ed.), ELFE at CERN, Conceptual Design Report CERN/NUPECC, Preprint CERN 99-10 (1999).
3. D. von Harrach, V. Metag, and A. Schafer, Nucl. Phys. A **622**, 46c (1997).
4. V. F. Dmitriev, D. M. Nikolenko, S. G. Popov, *et al.*, Phys. Lett. B **157**, 143 (1985).
5. M. V. Mostovoy, D. M. Nikolenko, K. T. Ospanov, *et al.*, Phys. Lett. B **188**, 181 (1987); S. I. Mishnev, D. M. Nikolenko, S. G. Popov, *et al.*, Phys. Lett. B **302**, 23 (1993).
6. P. Hoodbhoy, R. L. Jaffe, and A. Manohar, Nucl. Phys. B **312**, 571 (1989); R. L. Jaffe and A. Manohar, Nucl. Phys. B **321**, 343 (1989); P. Hoodbhoy, R. L. Jaffe, and E. Sather, Phys. Rev. D **43**, 3071 (1991).
7. S. Kumano and M. Miyama, Phys. Lett. B **497**, 149 (2000); S. Hino and S. Kumano, Phys. Rev. D **60**, 054018 (1999).
8. G. I. Gakh and N. P. Merenkov, Pis'ma Zh. Éksp. Teor. Fiz. **73**, 659 (2001) [JETP Lett. **73**, 579 (2001)].
9. A. V. Afanasev, I. Akushevich, G. I. Gakh, and N. P. Merenkov, Zh. Éksp. Teor. Fiz. **120**, 515 (2001) [JETP **93**, 449 (2001)].
10. S. D. Drell and T. M. Yan, Phys. Rev. Lett. **25**, 316 (1970).
11. R. G. Arnold, C. E. Carlson, and F. Gross, Phys. Rev. C **23**, 363 (1981).
12. L. I. Lapidus, Fiz. Élem. Chastits At. Yadra **15**, 493 (1984) [Sov. J. Part. Nucl. **15**, 223 (1984)].
13. V. V. Kotlyar, Yu. P. Mel'nik, and A. V. Shebeko, Fiz. Élem. Chastits At. Yadra **26**, 192 (1995) [Phys. Part. Nucl. **26**, 79 (1995)].
14. *The Science Driving the 12 GeV Upgrade of CEBAF* (Jefferson Laboratory, 2001).
15. L. L. Frankfurt and M. I. Strikman, Phys. Rep. **76**, 215 (1981); J. L. Forest, V. R. Pandharipande, S. C. Pieper, *et al.*, Phys. Rev. C **54**, 646 (1996).

JETP Letters, Vol. 75, No. 12, 2002, pp. 617–620. Translated from Pis'ma v Zhurnal Éksperimental'noĭ i Teoreticheskoĭ Fiziki, Vol. 75, No. 12, 2002, pp. 741–745.

Self-Action Dynamics of Ultrashort Electromagnetic Pulses

A. A. Balakin* and V. A. Mironov

Institute of Applied Physics, Russian Academy of Sciences, ul. Ul'yanova 46, Nizhni Novgorod, 603950 Russia

** e-mail: abal@appl.sci-nnov.ru*

Received April 19, 2002

The equation generalizing the nonlinear Schrödinger equation to the case of pulses with a duration of few field oscillation periods is analyzed. A change in the effective parameters (centroid, duration, and width) of the wave field on the pulse propagation path are determined by the moments method. The collapse of spatial structure is shown to occur, and its formation associated with the steepening of the pulse leading edge are numerically studied. © *2002 MAIK "Nauka/Interperiodica".*

PACS numbers: 41.20.Jb; 42.65.Re

The development of laser technique, optoelectronics, and semiconductor technology have culminated in the design of systems generating electromagnetic pulses with a duration of few oscillation periods (see [1, 2] and bibliography therein). A new theoretical problem therefore arises of studying the propagation of an ultrashort electromagnetic pulse and its interaction with substance. The situation where the approximation of a slowly varying wave amplitude becomes inappropriate also occurs in the case of nonlinear processes leading to a noticeable broadening of the temporal spectrum.

The following equation is one of the simplest generalizations of the linear and nonlinear Schrödinger equations (NSE) used for studying the spatiotemporal evolution of ultrashort electromagnetic pulses [3–6]:

$$\frac{\partial^2 u}{\partial z \partial \tau} + \Delta_\perp u - \alpha u + |u|^2 u = 0. \qquad (1)$$

This equation describes the reflectionless propagation of the wave field $u(z, \tau = z - v_{gr}t, \mathbf{r})$ along the z axis with group velocity v_{gr}; r is the vector perpendicular to the z axis. The quantity α is determined by the low-frequency dispersion of the medium. The scale invariance of the original equation allows it to be represented in the form of Eq. (1). The dimensionless coordinates z, $\mathbf{r}$, and "time" τ are scaled to the corresponding nonlinear characteristics (spatial and temporal) of the problem. The dimensionless field $u(\mathbf{r}, z, \tau)$ is normalized to the characteristic nonlinear field. In particular, this equation is used for studying the self-action of a relativistically strong laser radiation in rarefied plasmas [6] ($\omega_p/\omega_0 \ll 1$, where ω_p is the plasma frequency and ω_0 is the wave frequency). In this case, the dispersion parameter $\alpha < 0$ is determined by the plasma density.

For the envelope $\psi(z, \tau, \mathbf{r})$ of the wave field $u = \psi(z, \tau, \mathbf{r})\exp i\omega\tau$, one can easily obtain the following equation from Eq. (1):

$$i\omega\frac{\partial \psi}{\partial z} + \frac{\partial^2 \psi}{\partial z \partial \tau} + \Delta_\perp \psi - \alpha\psi + |\psi|^2\psi = 0. \qquad (2)$$

In the approximation of a long (on the wavelength scale $2\pi/\omega$) quasi-monochromatic pulse, the second term in this equation is small compared to the first one ($\partial^2\psi/\partial z\partial\tau \ll \omega(\partial\psi/\partial z)$), and it is ordinarily ignored. One can see that the evolution of such a "long" pulse is described by the NSE.

As the pulse duration shortens, new effects arise in the course of wave propagation along the path. They can be explained as follows. Let us transform the second term in Eq. (2) using the perturbation method. In the first approximation, which corresponds to the NSE, one has $\psi_z = i(\Delta_\perp\psi + |\psi|^2\psi)/\omega$. This allows the additional term in Eq. (2) to be written as

$$\psi_{z\tau} = i(\Delta_\perp\psi_\tau + |\psi|^2\psi_\tau)/\omega. \qquad (3)$$

The first term in Eq. (3) accounts for the "nonstationary" wave diffraction. In vacuum, it determines the Goya effect [7]; the transformation of the spectrum of spatially limited field distribution [8] gives rise to the diffraction precursor [3, 5] and the horseshoe-shaped spatial wave structure [5, 9]. The structural changes of pulse shape caused by the dependence of the wave-packet group velocity on the field amplitude [the second term in Eq. (3)] were mainly studied for one-dimensional systems (capillary and optical fibers; see, e.g., [10, 11]).

In this work, the spatiotemporal evolution of the finite-duration wave fields are considered on the basis of Eq. (1) and equivalent Eq. (2). We will first obtain some analytic relations and use them to qualitatively

analyze the characteristic features of the dynamics of spatially limited wave fields, and then present the results of the numerical study of Eqs. (1) and (2).

1. We use the moments method to qualitatively study the self-action dynamics of ultrashort pulses [12]. Note first that the parameters

$$I = \int |u_\tau|^2 d\tau d\mathbf{r}_\perp,$$
$$H = \int (|\nabla_\perp u|^2 + \alpha|u|^2 - |u|^4/2) d\tau d\mathbf{r}_\perp, \quad (4)$$
$$\mathbf{P} = \int (u_\tau^* \nabla u + u_\tau \nabla u^*) d\tau d\mathbf{r}_\perp,$$

generalizing the well-known NSE expressions (I is the "energy" or the "number of quanta," H is the Hamiltonian, and P is the "momentum" or energy flux) are conserved on the pulse propagation path.

Next, using the continuity equation

$$\frac{\partial}{\partial z}|u_\tau|^2 = -\mathrm{div}(u_\tau^* \nabla_\perp u + u_\tau \nabla_\perp u^*) + \frac{\partial}{\partial \tau}(|\nabla_\perp u|^2 - |u|^4/2 + \alpha|u|^2), \quad (5)$$

one can easily derive the following relations for the moments of the form $I_{n,m} = \int \tau^n \mathbf{r}_\perp^m |u_\tau|^2 d\tau d\mathbf{r}_\perp$ (m and n are integers). For the first-order moments $\bar{\tau} = \int \tau |u_\tau|^2 d\tau d\mathbf{r}_\perp$ and $\bar{\mathbf{r}}_\perp = \int \mathbf{r}_\perp |u_\tau|^2 d\tau d\mathbf{r}_\perp$ describing the behavior of the wave-field centroid, one has

$$\frac{\partial \bar{\tau}}{\partial z} = -H, \quad \frac{\partial \bar{\mathbf{r}}_\perp}{\partial z} = \mathbf{P}. \quad (6)$$

It follows that the wave-field centroid moves along the straight line determined by the initial conditions (e.g., at $z = 0$). For the axisymmetric wave packet ($\mathbf{P} = 0$), the centroid moves along the z axis. Depending on the sign of Hamiltonian H, the wave- packet group velocity can be both higher ($H < 0$) and lower ($H > 0$) than the pulse velocity in a linear medium. The center-of-mass shift to the leading ($H < 0$) or trailing ($H > 0$) pulse edge results in an appropriately convex (concave) horseshoe-shaped wave-field structure on the pulse propagation path.

The behavior of the squared characteristic wave-field duration $\overline{(\tau - \bar{\tau})^2} = \int (\tau - \bar{\tau})^2 |u_\tau|^2 d\tau d\mathbf{r}_\perp$ reflects another specific feature of the problem. From Eqs. (1) and (5), one finds

$$\frac{d^2 \overline{(\tau - \bar{\tau})^2}}{dz^2} = 4\int [|\Delta_\perp q + p|^2 - 2\alpha(|\nabla_\perp q|^2 - |\nabla_\perp u|^2)] d\tau d\mathbf{r}_\perp - 2\alpha H, \quad (7)$$

where the notation $q_\tau = u$ and $p_\tau = |u|^2 u - \alpha u$ is introduced.

The right-hand side of Eq. (7) is written in a form suitable for obtaining the results associated with its positive definiteness. In the linear case ($|u| \longrightarrow 0$ and $H > 0$), an obvious conclusion can be drawn from Eq. (7) that the wave packet spreads in the longitudinal direction. It is important that this result holds in the absence of dispersion ($\alpha = 0$), irrespective of the Hamiltonian sign. In a more general case ($\alpha \neq 0$), this conclusion is not quite clear. However, for the pulses of duration exceeding several field periods ($|\nabla_\perp u| > |\nabla_\perp q|$) and, hence, for $H < 0$, $\alpha > 0$, one again arrives at the conclusion that the wave-packet spreads during the course of system evolution.

Finally, as in the case of NSE, the following relation can be obtained for the effective wave-field width $\overline{r_\perp^2} = \int r_\perp^2 |u_\tau|^2 d\tau d\mathbf{r}_\perp$:

$$\frac{d^2 \overline{r_\perp^2}}{dz^2} = 8H - 16\alpha \int |u|^2 d\tau d\mathbf{r}_\perp. \quad (8)$$

Thus, in the case of negative Hamiltonian ($H < 0$ and $\alpha \geq 0$), the wave packet "collapses" in the transverse direction at a certain finite z that is determined from the initial field distribution and the value of Hamiltonian H. Contrary to the analogous NSE process, field singularity on the axis forms despite the pulse longitudinal spreading, which leads to a decrease in the linear value of the Hamiltonian.

For the axisymmetric wave packet and $\alpha = 0$, from Eqs. (6) and (8) one can obtain the expression

$$\overline{\mathbf{r}_\perp^2} - 4z\bar{\tau} = \overline{r_0^2}, \quad (9)$$

which relates the effective scales of $\overline{r_0^2}$ and $\bar{\tau}$ to each other during the process of system evolution ($\sqrt{\overline{r_0^2}}$ is the characteristic transverse scale of field at $z = 0$). This relation is a consequence of the formation of the horseshoe-shaped wave-packet structure. Formally, it has the same form as in the linear case. In the nonlinear case and $H < 0$, Eqs. (9) and (6) can be used to estimate, e.g., the distance

$$\bar{\tau}_0 = \sqrt{|H|\overline{r_0^2}}/2 \quad (10)$$

at which the wave-packet centroid shifts during the collapse.

2. Let us now discuss the results of the numerical integration of Eq. (1) in the axisymmetric case. The initial wave-field distribution was taken in the form of a Gaussian envelope with the carrier frequency ω_0:

$$u = u_0 \exp\left(-\left[\frac{\rho^2}{2a^2} + \frac{\tau^2}{2\tau_0^2}\right]\right) \exp i\omega_0 \tau. \quad (11)$$

The integration results were controlled using integrals (4).

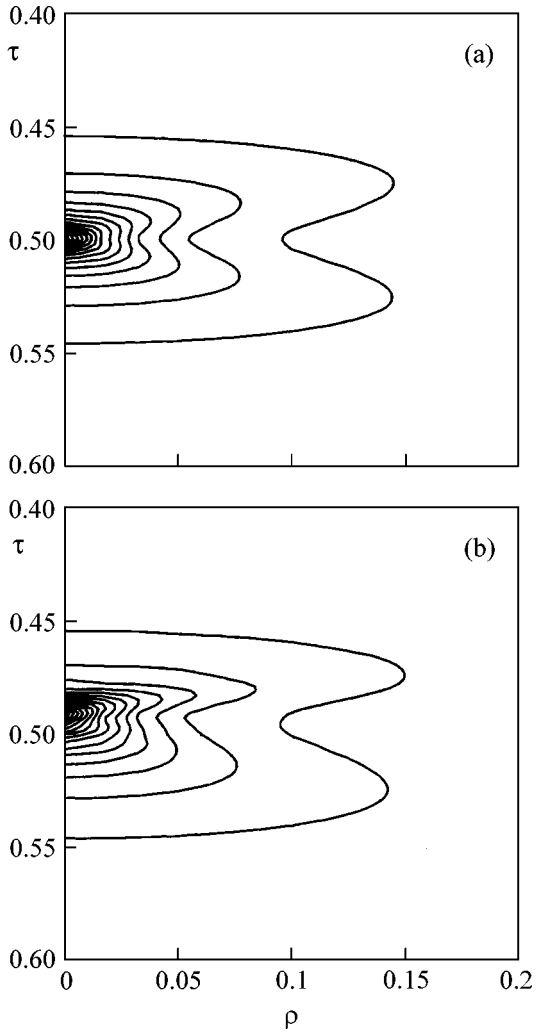

Fig. 1. Amplitude distribution map of (b) quasi-monochromatic ($\Delta\omega/\omega_0 = 10^{-3}$) and (a) short ($\Delta\omega/\omega_0 = 0.05$) pulses during the collapse at $\omega_0 z = 24.4$.

For a positive value of the Hamiltonian, the wave-field evolution proceeds qualitatively as in the linear case (in vacuum) [2, 5, 8]. The wave field spreads in the transverse direction. The pulse duration increases. The centroid shifts to the back boundary of the computational interval, in compliance with Eq. (6). As a result, the characteristic horseshoe-shaped structure is formed.

Let us consider the case of negative Hamiltonian ($H < 0$) in more detail. Using Eq. (10), one can easily see that the structural changes of shape (11) on the propagation path can be disregarded for $\alpha = 0$ if

$$\tau_0 > \sqrt{|H|a^2}/2\,. \qquad (12)$$

Under these conditions, the collapse takes on a local character (Fig. 1). The central part of the pulse has the maximal linear power and collapses first, after which the lateral parts are involved in this process. The peripheral parts (the regions near the leading and trailing edges) spread, because the linear power in these regions is lower than its critical value. As a result, the wave-field contour lines form the characteristic symmetric butterfly structure (Fig. 1a).

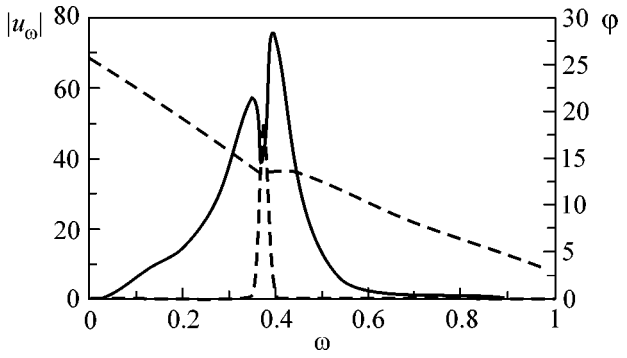

Fig. 2. (solid line; left axis) Spectrum of a short pulse ($\Delta\omega/\omega_0 = 0.05$) and (broken line; right axis) frequency dependence of the wave-field phase φ during the collapse at $\omega_0 z = 24.4$. Dotted line is the initial spectrum.

As the pulse duration decreases, the centroid shifts, and this is accompanied by a steepening of the pulse leading edge. The symmetry of the pattern breaks down. The collapse process is slightly accelerated. For the amplitudes considered, these effects become decisive at the spectral width $\Delta\omega/\omega \geq 0.01$. The corresponding wave-field evolution is shown in Fig. 1b. Note that the low-frequency dispersion does not stabilize the process of breaking the leading edge.

The above-mentioned self-compression of the pulse central part followed by the steepening of the leading edge should, evidently, be accompanied by a modification of the wave-field spectrum. Figure 2 shows the pulse spectrum on the axis of the system ($\rho = 0$) during the collapse process at $\omega_0 z = 24.4$. One can see that the self-action dynamics in the generalized NSE approach gives rise to a doublet in the wave-field spectrum. A more detailed study indicates that the spectrum of a quasi-monochromatic pulse virtually does not broaden during the collapse, so the formation of a doublet is the main effect in this case. For shorter initial pulses ($\Delta\omega/\omega > 0.01$), the wave-front broadening leads to an additional noticeable broadening of the spectrum. As the pulse duration shortens, the numerical computation of field evolution along z is limited by the accumulation of spectral harmonics near $\omega = 0$ and by breaking the integral relations (4).

To interpret the doublet formation in the spectrum, we note that the corresponding effect of spectrum modification in the focal region was discussed in [8] for the linear regime on the basis of the equations of type (2). It was demonstrated that the pulse central frequency decreases ahead of the focus and increases after passing it; the doublet appears for the "rays" perpendicular to the axis of the system, and this fact dominates its evolution dynamics. It is conceivable that, due to this fact,

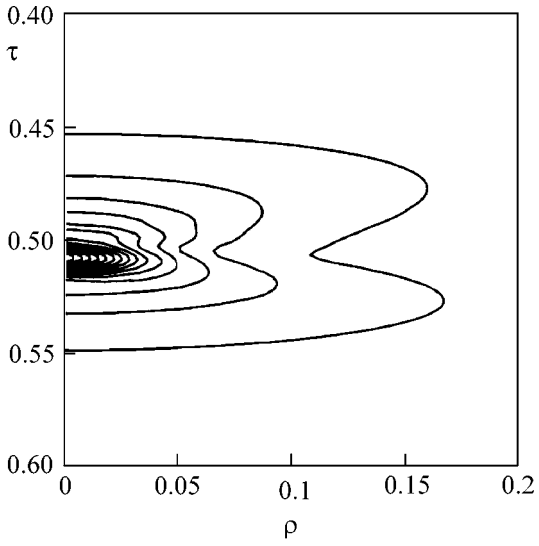

Fig. 3. Amplitude distribution map of the short pulse ($\Delta\omega/\omega_0 = 0.05$) after its compression by a quadratic phase corrector.

the doublet formation in the nonlinear regime predominates over the spectrum (up- or downfrequency) shift.

Thus, within the framework of the generalized NSE (1), wave-field collapse in a nonlinear medium is accompanied by a noticeable shortening of pulse duration (more than seven times at the halfwidth). This process provides a new method for creating intense ultrashort pulses with a duration of few field oscillations.

The following way can be suggested for further shortening the pulse duration. The frequency dependence of the wave-field phase φ in the spectrum of a pulse passed through a nonlinear medium has the form shown in Fig. 2. Then, using a linear quadratic phase corrector of the type used in the scheme of femtosecond pulse generation, one can compress the output pulse. As a result, the leading-edge steepening can be "converted" into the shortening of pulse duration. In this case, the field distribution in the central part becomes quasi-Gaussian (Fig. 3). Our calculations based on the appropriate approximation of the dependence in Fig. 2 for the field-maximum region showed that the pulse duration can additionally be decreased by a factor of 2 (cf. Figs. 1b and 3).

One more possibility is associated with the use of such pulses as an exciting pulse in the scheme of inverse Raman scattering in plasmas [13] with the object of its shortening and amplification.

We are grateful to A.A. Solodov for useful discussions. This work was supported by the Russian Foundation for Basic Research, project no. 02-02-17277.

REFERENCES

1. L. D. Bakhrakh and A. A. Bliskovitskiĭ, Usp. Fiz. Nauk **162** (12), 160 (1992) [Sov. Phys. Usp. **35**, 1086 (1992)].
2. IEEE J. Sel. Top. Quantum Electron. **2**, 679 (1996).
3. É. M. Belenov and A. V. Nazarkin, Pis'ma Zh. Éksp. Teor. Fiz. **53**, 188 (1991) [JETP Lett. **53**, 200 (1991)].
4. T. Brabec and F. Krausz, Phys. Rev. Lett. **78**, 3282 (1997); Rev. Mod. Phys. **72**, 545 (2000).
5. V. A. Mironov, Zh. Éksp. Teor. Fiz. **116**, 35 (1999) [JETP **89**, 18 (1999)].
6. P. Sprangle, B. Hafizi, and P. Serafim, Phys. Rev. E **59**, 3614 (1999).
7. S. Feng and H. G. Winful, Phys. Rev. E **61**, 862 (2000); A. B. Ruffin, J. V. Rudd, J. F. Whitaker, *et al.*, Phys. Rev. Lett. **83**, 3410 (1999).
8. G. Glur, T. D. Visker, and E. Wolf, Phys. Rev. Lett. **88**, 013901 (2002).
9. M. A. Porras, Phys. Rev. A **60**, 5069 (1999).
10. N. E. Andreev and L. M. Gorbunov, Pis'ma Zh. Éksp. Teor. Fiz. **56**, 144 (1992) [JETP Lett. **56**, 139 (1992)].
11. V. E. Zakharov and E. A. Kuznetsov, Zh. Éksp. Teor. Fiz. **113**, 1892 (1998) [JETP **86**, 1035 (1998)].
12. S. N. Vlasov, V. A. Petrishchev, and A. I. Talanov, Izv. Vyssh. Uchebn. Zaved., Radiofiz. **14**, 1353 (1971).
13. V. Malkin, G. Shvets, and N. Fisch, Phys. Rev. Lett. **82**, 4448 (1999); Phys. Plasmas **7**, 2232 (2000).

Translated by V. Sakun

JETP Letters, Vol. 75, No. 12, 2002, pp. 621–624. Translated from Pis'ma v Zhurnal Éksperimental'noĭ i Teoreticheskoĭ Fiziki, Vol. 75, No. 12, 2002, pp. 746–749.

Zakharov–Benney Resonance as a Mechanism for Generating Extremely Short Pulses in Uniaxial Crystals

S. V. Sazonov* and A. F. Sobolevskiĭ

Kaliningrad State University, Kaliningrad, 236041 Russia

** e-mail: sazonov@phys.tsu.ru, nst@alg.kaliningrad.ru*

Received April 30, 2002

The possibility of generating an extremely short (without high-frequency filling) pulse of an extraordinary wave in a uniaxial crystal by means of nonlinear interaction with a quasi-monochromatic ordinary wave in the regime of Zakharov–Benney resonance is discussed. It is shown that the appropriate conditions can be created in crystals with positive birefringence, and stable extremely short extraordinary solitons can be created in the spectral range of normal dispersion at the threshold intensity of input pulse on the order of 10^{13}–10^{14} W/cm^2. © *2002 MAIK "Nauka/Interperiodica".*

PACS numbers: 42.65.Re; 42.65.Tg

In recent years, considerable interest has been shown in the problem of the interaction between extremely short pulses (ESPs) or video pulses and substance [1]. Such pulses carry one (or even a half) period of electromagnetic oscillations, and the character of their interaction with substance may be essentially different from that in the case of quasi-monochromatic pulses with a well-defined carrier frequency [2]. Among other things, the generation of ESPs is a topical problem because of their possible use in information-optical systems: with shortening pulse duration τ_p, the potential transmission capacity of such systems increases. At present, the τ_p values for ESP vary in the range from hundreds and tens of femtoseconds [3, 4] to a few [5] femtoseconds. The possibility of generating attosecond pulses is also under discussion [1, 5]. The mechanisms based on Cherenkov radiation in a quadratically nonlinear medium [3], mode locking [6], compression of phase-modulated signals in dispersive media [4], continuous energy transfer from the input quasi-monochromatic pulse to the Stokes component as a result of stimulated Raman scattering [7–9], etc. have been proposed and implemented [1].

In this work, the possibility of ESP generation through nonlinear intermode interactions in uniaxial crystals is considered.

Let a quasi-monochromatic pulse with carrier frequency ω lying in the transparent range of the crystal ($\omega \ll \omega_0$, where ω_0 is the characteristic optical resonance frequency at which the absorption occurs) be incident on the crystal along the z direction perpendicular to the crystal optical axis y. The polarization plane of the incident pulse is normal to the principal plane, i.e., to the (y, z) plane, and is parallel to the x axis. Hence, the incident pulse is polarized in the plane of the ordinary wave. For this propagation geometry, the wave normals and rays are codirected, as a result of which the longitudinal wave component is absent [10] and only the ordinary E_o and extraordinary E_e pulse electric-field components associated with the corresponding P_o and P_e polarization components are involved in the dynamics.

In the low-frequency transparent region, the nonlinearity and dispersion can be taken into account additively in the polarization expansion in powers of the field and its derivatives [1, 11]. Then,

$$P_o = \chi_o E_o + 2\chi_{eo} E_e E_o - \kappa_0 \partial^2 E_o/\partial t^2, \qquad (1)$$

$$P_e = \chi_e E_e + \chi_{eo} E_o^2 + \chi_{ee} E_e^2 - \kappa_e \partial^2 E_e/\partial t^2, \qquad (2)$$

where $\chi_o = \chi_{xx}^{(1)}$ and $\chi_e = \chi_{yy}^{(1)}$ are the tensor components of low-frequency susceptibility, $\chi_{eo} = \chi_{xxy}^{(2)} = \chi_{xyx}^{(2)} = \chi_{yxx}^{(2)}$ and $\chi_{ee} = \chi_{yyy}^{(2)}$ are the nonzero tensor components of quadratic low-frequency susceptibility (the term "low-frequency" should be understood in the sense that $\omega = 0$ is formally set in the corresponding expressions [11, 12]), and $\kappa_{o,e} = 0.5(\partial^2\chi_{o,e}/\partial\omega^2)_{\omega=0}$ are the coefficients allowing for the dispersion of electron response; $\kappa_{o,e} > 0$, because the electronic dispersion in the equilibrium medium is positive.

Note that the symmetry properties of a uniaxial medium, i.e., invariance about the inversion of coordinates transverse to the optical axis (then $P_o \longrightarrow -P_o$ and $E_o \longrightarrow -E_o$) and its absence for the inversion about the longitudinal coordinates ($P_e \longrightarrow -P_e$ and $E_e \longrightarrow -E_e$), are taken into account in Eqs. (1) and (2).

By substituting Eqs. (1) and (2) into the right-hand sides of the corresponding Maxwell wave equations, applying the approximation of unidirectional propaga-

tion along the z axis [2, 11, 12], and taking into account that $|\chi_e - \chi_o| \ll \chi_e, \chi_o$, one obtains

$$\frac{\partial E_0}{\partial z} + \frac{n_o}{c}\frac{\partial E_0}{\partial t} + a\frac{\partial}{\partial t}(E_e E_o) - \delta_o\frac{\partial^3 E_o}{\partial t^3} = \frac{c}{2n_o}\Delta_\perp\int_{-\infty}^{t} E_o dt', \tag{3}$$

$$\frac{\partial E_e}{\partial z} + \frac{n_e}{c}\frac{\partial E_e}{\partial t} + aE_o\frac{\partial E_o}{\partial t} + bE_e\frac{\partial E_e}{\partial t} - \delta_e\frac{\partial^3 E_e}{\partial t^3} = \frac{c}{2n_o}\Delta_\perp\int_{-\infty}^{t} E_e dt'. \tag{4}$$

Here, c is the speed of light in vacuum; $n_{o,e} = \sqrt{1 + 4\pi\chi_{o,e}}$ are the ordinary and extraordinary refractive indices, respectively; $a = 4\pi\chi_{eo}/n_o c$; $b = 4\pi\chi_{ee}/n_o c$; $\Delta_\perp$ is the transverse Laplacian; and $\delta_{o,e} = 2\pi\kappa_{o,e}/n_o c$.

Note that the approximation of slowly varying envelope (SVE) [4] was not used for the moment, and Eqs. (3) and (4) contain the field strengths rather than their envelopes. However, it is straightforward to show that, in the SVE approximation, the system of Eqs. (3) and (4) transforms to the well-known system describing the second harmonic generation (SHG) [4] (in this case, the fundamental harmonic belongs to the ordinary component).

The energy transfer from the fundamental to second harmonic is most efficient if the phase- and group-matching conditions are fulfilled (the phase and group velocities should be the same for both frequencies) [4]. In our case, these conditions can be written, respectively, in the form

$$(n_o - n_e)/c = \omega^2(4\delta_e - \delta_o), \quad (n_o - n_e)/c = 3\omega^2(4\delta_e - \delta_o). \tag{5}$$

It follows from Eqs. (5) that both conditions cannot be satisfied in the collinear regime. In the stationary (continuous) regime, there is only the phase-matching condition, which is expressed by the first relation in Eqs. (5). Because the positive values of δ_o and δ_e usually differ only slightly from one another, the stationary collinear SHG regime can be implemented in a uniaxial crystal with negative birefringence ($n_o > n_e$).

Apart from the SHG, the system of Eqs. (4) and (5) can describe the regime of energy transfer from a high-frequency ordinary component to the fundamental harmonic of extraordinary component (optical detection). This can be demonstrated by representing E_o in the form

$$E_o = \xi e^{i(\omega t - k_o z)} + \text{c.c.}, \tag{6}$$

where ξ is the slowly varying envelope and k_o is the wavenumber of the ordinary wave. We also assume that E_e has no carrier frequency. By inserting Eq. (6) into Eqs. (3) and (4), neglecting the fast oscillating terms, and taking into account that $|\partial\xi/\partial t| \ll \omega\xi$, one arrives at the following system of equations describing the interaction between E_e and ξ in the regime of Zakharov–Benney resonance (ZBR):

$$i\frac{\partial\xi}{\partial z} + g\frac{\partial^2\xi}{\partial\tau^2} = \omega a E_e\xi + \frac{c}{2n_o\omega}\Delta_\perp\xi, \tag{7}$$

$$\frac{\partial E_e}{\partial z} + bE_e\frac{\partial E_e}{\partial\tau} - \delta_e\frac{\partial^3 E_e}{\partial\tau^3} = -a\frac{\partial}{\partial\tau}(|\xi|^2) + \frac{c}{2n_o}\Delta_\perp\int_{-\infty}^{\tau} E_e d\tau', \tag{8}$$

where $g = 3\delta_0\omega$, $\tau = t - z/v_g$, and the group velocity v_g of the ordinary component is given by the expression $1/v_g = dk_o/d\omega = n_o/c + 3\delta_o\omega^2$.

In Eq. (8), the ZBR condition is taken into account, according to which the group velocity of the short-wavelength (ordinary) wave is equal to the phase velocity of the long-wavelength (extraordinary) component [13]; i.e., $v_g = c/n_e$. In our case, this can be rewritten as

$$(n_e - n_o)/c = 3\delta_o\omega^2. \tag{9}$$

If the diffraction is neglected ($\Delta_\perp = 0$), Eqs. (7) and (8) transform to the system studied in [14]. If, in addition, the intrinsic nonlinearity and dispersion of the extraordinary component are also neglected ($b = \delta_e = 0$), Eqs. (7) and (8) transform to the integrable Yadjima–Oikawa system [15], i.e., to the unidirectional variant of the Zakharov system [16]. The corresponding single-soliton two-parametric solution in the laboratory frame of coordinates has the form

$$\xi = \xi_m e^{-i(\Omega t - qz)}\operatorname{sech}\left(\frac{t - z/V}{\tau_p}\right), \quad E_e = -E_{em}\operatorname{sech}^2\left(\frac{t - z/V}{\tau_p}\right), \tag{10}$$

where $\xi_m = (6\delta_o/a\tau_p)\sqrt{\omega\Omega}$; $E_{em} = 6\delta_o/a\tau_p^2$; $q = \Omega/V + g(\Omega^2 + \tau_p^{-2})$; the velocity V is given by the expression $1/V = 1/v_g - 2g\Omega$; and the parameter Ω has a meaning of the nonlinear redshift of the short-wavelength component, because $\Omega > 0$ [see expression for ξ_m and Eqs. (6) and (10)].

The ordinary component is an envelope soliton, whereas the extraordinary component is a video soliton. One can see from Eqs. (7) and (8) that, if $E_e = 0$ at the input of the crystal, then the ordinary envelope pulse can produce an extraordinary video pulse inside the medium. In this case, every ordinary photon undergoes redshift, because it gives up a portion of its energy

to the extraordinary wave. This explains the nonlinear shift $\omega \longrightarrow \omega - \Omega$. Due to the positive sign of electronic dispersion, the group velocity of the ordinary component (along with that of the extraordinary one) is positively shifted, $1/v_g = n_o/c + 3\delta_o\omega^2 \longrightarrow n_o/c + 3\delta_o(\omega - \Omega)^2 \approx n_o/c + 3\delta_o\omega^2 - 6\delta_o\omega\Omega = 1/v_g - 2g\Omega$. This expression coincides with the expression for $1/v$ given above.

The intrinsic nonlinearity and dispersion of the extraordinary component are the effects of the same order of smallness. For this reason, they can be ignored if [see Eq. (8)] $bE_{em}^2 \ll a\xi_m^2$. Substituting the expressions for E_{em} and ξ_m in this inequality, one obtains $\omega\tau_p - \Omega\tau_p \gg b/a = \chi_{ee}/\chi_{eo}$. Assuming that χ_{ee} and χ_{eo} are of the same order of magnitude, one has $(E_{em}/\xi_m)^2 \ll 1$ (i.e., the intensity of the extraordinary component is relatively low). Since the ordinary component is quasimonochromatic, one has $\omega\tau_p \gg 1$. Then, the condition under discussion can rather easily be satisfied over a broad range of parameters Ω and τ_p.

On further propagation, the ordinary component can be removed, e.g., by a polaroid plate cut into the sample parallel to its optical axis. Then, the dynamics of the remaining extraordinary component, according to Eq. (8), will obey the Korteweg–de Vries equation, for which the E_e pulse of form (10) can play the role of input signal. From this point on, the evolution will be determined by the relations between the parameters of this signal and the coefficients b and δ_e, but either one or several video solitons will necessarily be produced [13].

From the experimental point of view, the stability of solution (10) to the self-focusing is an important problem. We will use the averaged Lagrangian method to examine this issue [17]. Since the solution (10) is obtained for $b = \delta_e = 0$, we will consider the stability problem under the same conditions. In this case, the system of Eqs. (7) and (8) can be obtained from the Lagrangian density

$$L = \frac{i}{2\omega}\left(\xi\frac{\partial\xi^*}{\partial z} - \xi^*\frac{\partial\xi}{\partial z}\right) + 3\delta_o\left|\frac{\partial\xi}{\partial\tau}\right|^2 - \frac{c}{2n_o\omega^2}|\nabla_\perp\xi|^2 + \frac{1}{2}\frac{\partial U}{\partial z}\frac{\partial U}{\partial\tau} - \frac{c}{2n_0}(\nabla_\perp U)^2 + a|\xi|^2\frac{\partial U}{\partial\tau}, \quad (11)$$

where the function U is related to E_e by the expression $E_e = \partial U/\partial\tau$.

Let us take expressions (10) with substitution $1/\tau_p \longrightarrow R(z, \mathbf{r}_\perp)$, $\xi_m \longrightarrow A(z, \mathbf{r}_\perp)$, $E_{em} \longrightarrow -B(z, \mathbf{r}_\perp)R(z, \mathbf{r}_\perp)$, and $qz \longrightarrow -\omega n_o\Phi(z, \mathbf{r}_\perp)/c$, where A, B, and R are "slow" functions and Φ is "fast" function of the longitudinal and transverse $\mathbf{r}_\perp$ coordinates, as a trial solution. Substituting this solution in Eq. (11) and retaining only the derivatives for fast variables [17], one obtains the following average Lagrangian after the integration over τ:

$$\Lambda \equiv \frac{1}{2}\int_{-\infty}^{+\infty} L d\tau = \frac{n_o}{cR}A^2\frac{\partial\Phi}{\partial z} - \delta_o A^2 R - 3\delta_o\frac{\Omega^2 A^2}{R} + \frac{n_o}{2cR}A^2(\nabla_\perp\Phi)^2 - 2\delta_o\omega\Omega B^2 R - \frac{2}{3}aA^2B.$$

Variation of this Lagrangian with respect to A, B, R, and Φ leads to the system of equations of ideal fluid dynamics on a plane (continuity equation and Cauchy integral):

$$\frac{\partial\rho}{\partial z} + \nabla_\perp(\rho\mathbf{V}_\perp) = 0, \qquad \frac{\partial\Phi}{\partial z} + \frac{\mathbf{V}_\perp^2}{2} + \int\frac{dp}{\rho} = 3\frac{c}{n_o}\delta_o\Omega^2, \quad (12)$$

where the coordinate z plays the role of time, $\mathbf{V}_\perp = \nabla_\perp\Phi$, and the "pressure" p is related to the "density" $\rho = A^2/R$ by the "equation of state"

$$\frac{dp}{d\rho} = 6\frac{c}{n_o}\delta_o\left(\frac{a}{6\delta_o\sqrt{\omega\Omega}}\right)^4\rho^2. \quad (13)$$

The expressions for A and B are: $A = 6\delta_o R\sqrt{\omega\Omega}/a$ and $B = -6\delta_o R/a$. In the one-dimensional case ($\nabla_\perp = 0$), one obtains $R = 1/\tau_p = \text{const}$, and the trial solutions transform to Eq. (10).

Evidently, the stability of solution (10) is equivalent to the stability of ideal flow of type (12) and (13): $dp/d\rho > 0$. It follows from Eq. (13) that this condition is fulfilled, because the dispersion of electron response is positive ($\delta_o > 0$).

The ZBR mechanism of video pulse generation is closely similar to the Cherenkov mechanism [3, 4]. The difference is that the generation regime in the latter case is noncollinear and is not solitonic. The angle γ between the propagation directions of the ESP and the generating pulse, whose spectrum contains two close edge frequencies ω_1 and ω_2 with wavenumbers k_1 and k_2, is given by the expression [4]

$$\cos\gamma = \frac{k_2(\omega_2) - k_1(\omega_1)}{k(\omega_2 - \omega_1)},$$

where $k(\omega_2 - \omega_1)$ is the wavenumber determined by the dispersion law at frequency $\omega_2 - \omega_1$. The velocity of the nonlinear polarization wave at the difference frequency should exceed the wave phase velocity in a medium at the same frequency:

$$\frac{\omega_2 - \omega_1}{k_1(\omega_2) - k_1(\omega_1)} > \frac{\omega_2 - \omega_1}{k(\omega_2 - \omega_1)}.$$

By passing to the limit $\omega_2 \longrightarrow \omega_1$ and setting $\gamma = 0$ in this inequality, one obtains the ZBR condition.

From Eq. (9), it follows that the ZBR regime considered above can be implemented in crystals with positive birefringence ($n_e > n_o$). Since n_e and n_o are close, one can write $n_e - n_o \approx (n_e^2 - n_o^2)/2n_o = 2\pi(\chi_e - \chi_o)/n_o$. In addition, $\delta_o = 2\pi\kappa_o/n_o c \approx 2\pi\chi_o/n_o c\omega_0^2$, and condition (9) takes the form $(\chi_e - \chi_o)/3\chi_o \approx (\omega/\omega_0)^2$. For crystalline quartz, $n_e = 1.55$ and $n_o = 1.54$ [18]. Then, $(\chi_e - \chi_o)/3\chi_o \approx 0.01$. Hence, $\omega/\omega_0 \approx 0.1$. Taking $\omega_0 \sim 10^{16}$ s^{-1} [19], one finds $\omega \sim 10^{15}$ s^{-1}. Inasmuch as $\omega\tau_p \gg 1$ for the input pulse, its duration is $\tau_p \sim$ 10–100 fs. According to Eq. (13), the duration of the generated video soliton is of the same order. Therefore, by appropriately choosing the carrier frequency of the input signal, one can satisfy the ZBR condition and thereby implement efficient ESP generation.

Let us estimate the input intensity for which a video soliton can be created in a crystal. For $b = \delta_e = \Delta_\perp = 0$, one has from Eq. (8) $E_e \sim (1/v - 1/v_g)^{-1}a|\xi|^2 \sim -a|\xi|^2/2g\Omega$. Substituting this in Eq. (7) with $\Delta_\perp = 0$, one arrives at the nonlinear Schrödinger equation (NSE)

$$i\frac{\partial\xi}{\partial z} + g\frac{\partial^2\xi}{\partial\tau^2} + \beta|\xi|^2\xi = 0,$$

where $\beta = \omega a^2/2g\Omega$ [strictly speaking, this is not an equation, because the coefficient β contains the parameter Ω of the solitonic solution to the system of Eqs. (7) and (8)].

It is known [13] that the NSE soliton can be created only if the threshold condition $\xi_0\tau_{p0} > \sqrt{g/\beta}$ is met, where ξ_0 and $\tau_{p0} \sim \tau_p$ are the input pulse amplitude and duration, respectively. Then, using the expression for β, a, and g, one gets $\xi_0 > (\chi_o/\chi_{eo})\sqrt{\omega\Omega}/\omega_0^2$.

Since $\chi_o/\chi_{eo} \sim \chi^{(1)}/\chi^{(2)} \sim \hbar\omega_0/d$ [1], where $\hbar$ is the Planck's constant and d is the characteristic value of dipole transition moment for the quantum transitions involved in the interaction with pulse, one has $\xi_0 > \xi_{th} \sim \hbar\sqrt{\omega\Omega}/d\omega_0\tau_p$. Taking $\Omega \sim 1/\tau_p \sim 10^{14}$ s^{-1}, $\omega \sim 10^{15}$ s^{-1}, $\omega_0 \sim 10^{16}$ s^{-1}, $d \sim 10^{-20}$ CGSE, one obtains for the threshold intensity $I_{th} \sim c\xi_{th}^2/4\pi \sim 10^{13}$–$10^{14}$ W/cm^2. Then, the intensity of the created video soliton is $I_e \approx cE_{em}^2/4\pi \sim c\xi_m^2/4\pi\omega\tau_p \sim I_{th}/\omega\tau_p \sim 0.1I_{th} \sim 10^{12}$–$10^{13}$ W/cm^2.

Although not rigorous, the above estimate procedure nevertheless yields reasonable values of threshold intensities, which can easily be attained by modern lasers.

The fact that conditions (5) and (9) are fulfilled in crystals with opposite signs of birefringence should be favorable for the effective separation of video soliton creation from SHG.

This work was supported by the Russian Foundation for Basic Research, project no. 02-02-17710a.

REFERENCES

1. T. Brabec and F. Krausz, Rev. Mod. Phys. **72**, 545 (2000).
2. A. I. Maĭmistov, Kvantovaya Élektron. (Moscow) **30**, 287 (2000).
3. D. H. Auston, K. P. Cheung, J. A. Valdmanis, and D. A. Kleinman, Phys. Rev. Lett. **53**, 1555 (1984).
4. S. A. Akhmanov, V. A. Vysloukh, and A. S. Chirkin, *The Optics of Femtosecond Pulses* (Nauka, Moscow, 1988).
5. A. V. Kim and M. Yu. Ryabikin, Usp. Fiz. Nauk **169**, 58 (1999).
6. T. W. Hönsch, Opt. Commun. **80**, 71 (1990).
7. É. M. Belenov, P. G. Kryukov, A. V. Nazarkin, and I. P. Prokopovich, Zh. Éksp. Teor. Fiz. **105**, 28 (1994) [JETP **78**, 15 (1994)].
8. A. Nazarkin and G. Korn, Phys. Rev. A **58**, R61 (1998).
9. Fam Le Kien, J. Q. Liang, M. Katsuragawa, *et al.*, Phys. Rev. A **60**, 1562 (1999).
10. M. Born and E. Wolf, *Principles of Optics* (Pergamon, Oxford, 1968; Nauka, Moscow, 1973).
11. É. M. Belenov and A. V. Nazarkin, Pis'ma Zh. Éksp. Teor. Fiz. **51**, 252 (1990) [JETP Lett. **51**, 288 (1990)].
12. I. V. Mel'nikov, D. Mihalache, F. Moldoveanu, and N.-C. Panoiu, Phys. Rev. A **56**, 1569 (1997).
13. R. K. Dodd, J. C. Eilbeck, J. D. Gibbon, and H. C. Morris, *Solitons and Nonlinear Wave Equations* (Academic, London, 1984; Mir, Moscow, 1988).
14. E. S. Benilov and S. P. Burtzev, Phys. Lett. A **98**, 256 (1983).
15. N. Yadjima and M. Oikawa, Prog. Theor. Phys. **56**, 1719 (1976).
16. V. E. Zakharov, Zh. Éksp. Teor. Fiz. **62**, 1745 (1972) [Sov. Phys. JETP **35**, 908 (1972)].
17. S. K. Zhdanov and B. A. Trubnikov, *Quasigaseous Unstable Media* (Nauka, Moscow, 1991).
18. R. Stiober and S. Morse, *Microscopic Identification of Crystals* (The Ronald Press, New York, 1972; Mir, Moscow, 1974).
19. S. A. Kozlov and S. V. Sazonov, Zh. Éksp. Teor. Fiz. **111**, 404 (1997) [JETP **84**, 221 (1997)].

Translated by V. Sakun

JETP Letters, Vol. 75, No. 12, 2002, pp. 625–630. Translated from Pis'ma v Zhurnal Éksperimental'noĭ i Teoreticheskoĭ Fiziki, Vol. 75, No. 12, 2002, pp. 750–755.

Radiation of a Charge Moving over the Diffraction Grating

Yu. A. Pobedin

ul. Stankevicha 1, kv. 14, Voronezh, 394018 Russia

Received December 26, 2001; in final form, April 29, 2002

The states of a charged particle with a finite free path are determined in the field of a resonant electromagnetic wave. The exact resonance conditions, the modulation and beam instability mechanisms, the charge and current densities (Ohm's law) are obtained for the collisionless beam of resonance particles. Quantum theory of radiation is developed for the resonant adiabatic interaction between a particle and a wave taking into account the interaction with a constant magnetic field induced at the grating surface by the charge and nonresonant waves. The radiation power, the spectrum, and the range of generated frequencies are determined. The results obtained can be used in the plasma and solid-state theories and in electronics. © *2002 MAIK "Nauka/Interperiodica".*

PACS numbers: 41.60.-m; 42.79.Dj

1. The theoretical [1] and experimental studies in the optical range (Smith–Purcell effect [2]) have aroused persistent interest in the generation of electromagnetic field by an electron beam passing over the surface of a diffraction grating perpendicular to its grooves. This effect has found use in O-type devices based on long-duration interaction in the millimeter and submillimeter range with grating in an open single-mode resonator (orotron-type devices [3]). In the oscillation regime, the grating interacts with particles to produce slow surface waves of diffraction radiation with phase velocities $v_{ph} \ll c$, where c is the speed of light [4] (the diffraction radiation, i.e., the beam field scattered by grating, also contains fast harmonics that break away from the surface; we will ignore these in what follows [4]).

The available theories of frequency generation are based on the known approximate classical theory of energy exchange in plasma [5], where a particle and the resonant wave propagate in the same direction with close phase v_{ph} and particle v velocities. Quantum theories of energy exchange supplement the classical theory (see, e.g., [6]).

These theories do not apply in the case of finite free path $L = Nd$ (d is the lattice period and $N \gg 1$ is the number of periods) of a particle in the field and in the case of prolonged interaction, i.e., under conditions of adiabatic interaction in the system, $\omega T \gg 1$ [ω is the oscillation frequency and $T = L/v$ (by order of magnitude) is the interaction time]. So, the theory of the effect has not been fully elaborated to date. The field of slow waves is negligible outside the resonator [4]. In this work, the quantum nonrelativistic theory of the resonant adiabatic interaction between a particle and a wave is developed. The periodic potential of the electron–wave interaction is considered as a barrier with finite spatial and temporal "widths" L and T [7]. It is assumed that the classical resonance conditions in the barrier region $|\alpha| = |\Delta v|/v_{ph} < 1$, where $v = v - v_{ph}$ (α characterizes the relative velocity mismatch), and $\lambda \gg \lambda_B$, where λ and λ_B are the field and the particle wavelengths, respectively, are fulfilled. The radiation processes and beam instability are caused by the tunneling transitions (quantum parametric resonance [7]) of particles with energies (in the wave-fixed system of coordinates) falling within the forbidden gaps in the familiar problem of a particle in the periodic potential with cyclic boundary conditions.

This effect is of interest as an experimentally well-elaborated model of the processes occurring in real systems and media with finite particle free path in a field. Among such processes are, e.g., the interaction with Langmuir waves and the beam instability in confined plasmas. In solid-state theory, these are the interaction of particles with the long-wavelength phonons in defect crystals and the channeling, with L being the length of the undistorted region of the crystal or channel.

We will ignore the interparticle interaction in a rarefied beam and develop the single-particle theory. The three-dimensional Schrödinger equation will be solved with the inclusion of all interactions typical of this system: the interaction with a constant uniform focusing magnetic field $\mathcal{H} = (0, 0, \mathcal{H})$ (the z axis lies in the grating plane along the direction of particle motion, the x axis is parallel to the grooves, and the y axis is perpendicular to the grating plane) with vector potential $\mathbf{A}_{\mathcal{H}} = (0, x\mathcal{H}, 0)$; the interaction with nonresonant harmonics; and the interaction with a z-periodic potential $V(\mathbf{r})$ (with period d) of a charge induced at the grating surface. This charge causes primary beam modulation [8], which excites the grating. The theory is developed for arbitrary wave amplitudes in the nonrelativistic approximation.

0021-3640/02/7512-0625$22.00

2. The scalar potential of a field produced by slow waves can be written in the form

$$\Phi(\mathbf{r}, t) = \sum_{m \neq 0} r_m(x, y)\cos(k_m z - \omega t + \eta_m), \quad (1)$$

where $k_m = \omega/v_m = 2\pi m/d$, v_m is the phase velocity of the mth wave, $\pi \geq \eta_m \geq -\pi$ is the phase, $r_m(x, y) = r_m(x)\exp(-k_m^y y)$, $k_m^y = (1 - (v_m/c)^2)^{1/2}$, and $r_m(x)$ is the amplitude of the mth wave with the known x distribution [4]. The vector potential $\mathbf{A}_f$ has the same form ($\mathbf{A}_f$ and Φ correspond to the magnetic and electric field, respectively) as in the classical theory of orotron [4]. In the Lorentz gauge, $|\mathbf{A}_f| \sim c^{-1}|\Phi|$. In what follows, $\mathbf{A}_f$ is ignored.

The Hamiltonian of a particle moving over the grating is

$$\hat{H} = \frac{1}{2m_e}\left(\hat{\mathbf{p}} + \frac{e}{c}\mathbf{A}_{\mathscr{H}}\right)^2 + \frac{e\hbar}{cm_e}\hat{\boldsymbol{\sigma}}\mathscr{H} + W(\mathbf{r}, t),$$

where $2\pi\hbar$ is the Planck's constant; m_e and e are the electron mass and charge, respectively; $\hat{p} = (\hat{p}_x, \hat{p}_y, \hat{p}_z)$ and $\hat{\boldsymbol{\sigma}}$ are, respectively, the momentum and spin operators; and $W = V - e\Phi$.

The solution to the Schrödinger equation is sought in the form

$$\Psi = \kappa(x)\chi(\mathbf{r}, t)\exp(i\hbar(p_y y - E_\perp t)), \quad (2)$$

where p_y is the transverse momentum component and $E_\perp$ is the energy of transverse motion.

Let $\mathscr{H}$ be such that V and Φ change weakly in the region of transverse motion comparable in size to the Larmor radius. We ignore the derivatives of χ with respect to x and y assuming that χ is a "slow" function of these variables. It is known that the motion of a wave packet in the field $\mathscr{H}$ coincides with the motion of a classical particle with coordinates x_0 and y_0. By writing in the Larmor region $W = W(z, t; x_0, y_0)$ and $\chi = \chi(z, t; x_0, y_0)$, where x_0 and y_0 are parameters, we obtain the following equation with separable variables:

$$\kappa\left[\frac{\partial^2\chi}{\partial z^2} - \frac{2m_e}{\hbar^2}\left(W - i\hbar\frac{\partial}{\partial t}\right)\chi\right]$$

$$= -\chi\left[\frac{d^2\kappa}{dx^2} + \frac{2m_e}{\hbar^2}\left(E_\perp - \frac{m_e}{2}\left(\frac{e\mathscr{H}}{cm_e}\right)^2(x - x_0)^2\right)\kappa\right],$$

where $x_0 = cp_y/e\mathscr{H}$. The coordinate part of the well-known solution for κ is [9]

$$\kappa = \exp\left(-\frac{e}{2c\hbar}\mathscr{H}(x - x_0)^2\right)H_n\left(\sqrt{\frac{e}{c\hbar}\mathscr{H}}(x - x_0)\right),$$

where H_n are the Hermitian polynomials, $E_\perp \equiv E_{n,\sigma} = \left(n + \frac{1}{2} + \sigma\right)\frac{e\hbar}{cm_e}\mathscr{H}$, $\sigma = \pm\frac{1}{2}$, and n are integers. Appending the spin part of the above-mentioned solution and the exponential multiplier in Eq. (2) to κ, one obtains the wave function of transverse motion $\Psi_{n,\sigma}(x, y, t)$.

Let us assume that the particle is at resonance with the mth wave from Eq. (1) and pass on to the coordinate system comoving with this wave. To do this, we introduce the variable $2u = k_m z - \omega t + \eta_m$ [$u(L, T) \geq u \geq u(0, 0)$]; $\Delta u = k_m\alpha L/(1 + \alpha) = \pi m\alpha N/(1 + \alpha)$ is the "effective" barrier width and $\tau = t - \eta_m/\omega$ ($T > \tau > 0$) is the "local" time; the variables $z' = z$ and $t' = t$ relate to the "cloud" of nonresonant harmonics; and $t_0 = \eta_m/\omega$ is the origin for t'. The equation for χ in the new variables takes the form

$$\left[\left(\hat{H}_r - i\hbar\frac{\partial}{\partial\tau}\right) - \left(\hat{H}_{cl-lc} - i\hbar\frac{\partial}{\partial t'}\right)\right]\chi = 0,$$

where

$$\hat{H}_r = \frac{1}{2m_e^*}\hat{\mathscr{P}}^2 - \frac{1}{2}\omega\hat{\mathscr{P}} - W_m(u),$$

$m_e^* = 4m_e k_m^{-1}$ is the effective "mass" of a particle in the field of the resonant wave, $\hat{\mathscr{P}} = -i\hbar(\partial/\partial u)$ is the operator of generalized momentum, $W_n = er_m\cos 2u$,

$$\hat{H}_{cl-lc} = \frac{1}{2m_e}(\hat{P}_{z'}^2 - \{\hat{P}_{z'}, \hat{\mathscr{P}}\}) - W_{cl-lc},$$

$\{\hat{P}_{z'}, \hat{\mathscr{P}}\}$ is the anticommutator of $\hat{P}_{z'}$ and $\hat{\mathscr{P}}$, and

$$W_{cl-lc} = e\sum_{m' \neq m} r_{m'}(x_0, y_0)\cos(k_{m'}z' - \omega t' + \eta_{m'}).$$

We will seek a solution to this equation in the form

$$\chi(u, \tau; z', t') = \psi_{cl-lc}\varphi(u)\exp(i(\mathscr{P}_{\text{sh}}u - \Omega'\tau)), \quad (3)$$

where $\mathscr{P}_{\text{sh}} = 2k_{\text{sh}}/k_m = 4\Omega_{\text{sh}}/\omega$, $\hbar k_{\text{sh}}$ is the longitudinal momentum of the wave-matching particle ($\alpha = 0$), $\hbar\Omega' = E'$ is the particle energy in the comoving coordinate system, and

$$\hbar\Omega_{\text{sh}} = E_{\text{sh}} = \frac{\hbar^2}{2m_e^*}\mathscr{P}_{\text{sh}}^2.$$

We assume that, due to the resonance and to the "smoothness" of V caused by a high particle velocity relative to the grating, χ slowly varies along z'. The corresponding variation $\Delta z = \Delta u/k_m$ is small compared to the variation Δu of u. This allows the derivatives of χ with respect to z' to be ignored in $\hat{H}_{cl-lc}$. Then, the

variables in the equation become separable, and one should seek the solutions to the equation

$$\psi_{cl-lc}\left\{\left[\frac{1}{2m_e^*}\hat{\mathcal{P}}^2 - ((E_{\rm sh}+E')+W_m)\right]\varphi\right\} = \varphi\left(W_{cl-lc} + i\hbar\frac{\partial}{\partial t}\right)\psi_{cl-lc} \quad (4)$$

(hereafter, z' and t' are unprimed).

Assuming that the separation constant is zero, one obtains the equations

$$\left(\frac{d}{dt} - \frac{i}{\hbar}W_{cl-lc}\right)\psi_{cl-lc} = 0, \quad (5)$$

$$\left[\frac{d^2}{du^2} + (\mathcal{P}^2 + 2q\cos 2u)\right]\varphi = 0, \quad (6)$$

where

$$\mathcal{P}^2 = \frac{2m_e^*}{\hbar^2}(E_{\rm sh}+E') \neq 0, \quad q = \frac{1}{\hbar^2}em_e^* r_m(x_0, y_0),$$

$$E' \equiv E'_{\mathcal{P}} = \frac{\hbar^2}{2m_e^*}\mathcal{P}^2 - E_{\rm sh}.$$

One can assume that the interaction switches on instantaneously, because the switching-on time is $\Delta t \sim \lambda/v$ ($L \gg \lambda$) [6]. The quantity V can be expanded in terms of the reciprocal lattice vectors K_m; taking into account the relation between z and t, one has $V(z;\ x_0,\ y_0) = \sum_m V_m(x_0,\ y_0)\cos(k_m v t)$. Substituting $V(t)$ into Eq. (5) with the initial condition $\psi_{cl-lc}(t_0) = 1$ and using the generating function for the Bessel functions J, we obtain

$$\psi_{cl-lc} = \psi_{cl}\psi_{lc}, \quad (7)$$

where

$$\psi_{lc} = \prod_m \exp(iV'_m \sin(k_m z_0)) \times\left\{J_0(V'_m) + \sum_{m'\neq m} J_{m'}(V'_m)\exp(im'(k_m z + \pi))\right\},$$

$$V'_m = V_m(x_0, y_0)(\hbar k_m v)^{-1} = dV_m(2\pi\hbar m v)^{-1} = V_m(\hbar\omega(1+\alpha))^{-1}, \quad z_0 = vt_0,$$

$$\psi_{cl} = \prod_{m'\neq m}\left\{J_0(\vartheta_{m'}) + \sum_{m''\neq 0} J_{m''}(\vartheta_{m'}) \times \exp(im''(k_{m'}z - \omega t + \eta_{m',m}))\right\},$$

$$\vartheta_{m'} = \gamma_{m'}(x_0, y_0)\sin\left(\frac{1}{2}(\omega t - \eta_m)\right),$$

$$\eta_{m',m} = \frac{1}{2}(2\eta_{m'} - \eta_m + \pi),$$

$$\gamma_{m'} = 2er_m(x_0, y_0)(\hbar\omega)^{-1}.$$

Assume that, contrary to the results in [8], which apply to small impact parameters or far off the grating, the impact parameter y_0 is considerably larger than the atomic or interatomic distances. Since the interaction between an electron and the grating is coulombic, one can put $V_m \sim 1/y_0$. It follows from the well-known properties of the Bessel functions that this interaction dominates during the period of grating excitation or far off the grating, where $r_{m'}$ are negligible, while $\psi_{cl} \sim 1$. The influence of electron–grating interaction decreases ($\psi_{lc} \longrightarrow 1$) with an increase in y_0, ω, and v and a decrease in d. As $r_{m'}$ increases, the interaction with cloud modulates the wave function (3): ψ_{cl} decreases with increasing $r_{m'}$ to reach its minimum at $\vartheta_{m'} = \pm\gamma_{m'}$ and it is maximal ($\psi_{cl} = 1$) at the $\vartheta_{m'}$ zeros. Setting $q = 0$ in Eq. (6), one gets $\varphi = c_{\mathcal{P}}^{(\pm)}\varphi_{\rm in}^{(\pm)}$ and $C_{\mathcal{P}}^{(\pm)} = {\rm const}$, where $\varphi_{\rm in}^{(\pm)} = \exp(\pm i\mathcal{P}u)$. Then, the function χ for the incident $\mathcal{P}^+$ particle overtaking the wave ($\mathcal{P} > 0$) or $\mathcal{P}^-$ particle lagging behind the wave ($\mathcal{P} < 0$) is

$$\hat{\chi}_{\rm in}^{(\pm)} = C_{\mathcal{P}}^{(\pm)}\hat{\psi}_{\mathcal{P}}^{(\pm)}(u)\exp(-i\Omega'_{\mathcal{P}}(\tau),$$

where $\psi_{\mathcal{P}}^{(\pm)}(u) = \exp(i(\mathcal{P}_{\rm sh} \pm \mathcal{P})u)$, and, except for the factors containing η_m, one has in the variables z and t

$$\chi_{\rm in}^{(\pm)} = c_{\mathcal{P}}^{(\pm)}\psi_{\mathcal{P}}^{(\pm)}(z)\exp(-i\Omega_{\mathcal{P}}^{(\pm)}t),$$

where

$$\psi_{\mathcal{P}}^{(\pm)}(z) = \exp(ik_z^{(\pm)}z), \quad k_z^{(\pm)} \equiv k^{(\pm)} = \frac{1}{2}k_m(\mathcal{P}_{\rm sh} \pm \mathcal{P}),$$

$$\hbar\Omega_{\mathcal{P}}^{(\pm)} = E_{\mathcal{P}}^{(\pm)} = \frac{\hbar^2}{2m_e^*}(\mathcal{P}_{\rm sh} \pm \mathcal{P})^2.$$

Assuming that the period of $\chi_{\rm in}^{(\pm)}$ is L and using the quantization condition for $K^{(\pm)}$, we obtain for the quantization conditions for the $\mathcal{P}_{\rm sh}$ and $\mathcal{P}$ numbers: $\mathcal{P}_{\rm sh} = 2h_0/mN$ and $\mathcal{P} = 2h/mN$, where h and h_0 are integers. Then πmN is the period of $\hat{\chi}_{\rm in}^{(\pm)}$, and $c_{\mathcal{P}}^{(\pm)} = (\pi mN)^{-1/2}$.

3. The particles are in the tunnel states if the solutions to the Mathieu equation (6) with parameter $q < 0$ are unstable, i.e., if $\mathcal{P}$ lies in the intervals [10]

$$b_{2s+1}(q) > \mathcal{P}^2 > a_{2s+1}(q), \quad a_{2s}(q) > \mathcal{P}^2 > b_{2s}(q). \quad (8)$$

The energy bands (measured from E_{sh}) given by Eq. (6) for the incident particles with the indicated scatter of $\mathcal{P}$ are

$$\frac{\hbar^2}{2m_e^*}b_{2s+1} > E'_{\mathcal{P}} > \frac{\hbar^2}{2m_e^*}a_{2s+1},$$

$$\frac{\hbar^2}{2m_e^*}a_{2s} > E'_{\mathcal{P}} > \frac{\hbar^2}{2m_e^*}b_{2s},$$

where $a_l(q)$ and $b_l(q)$ are the eigenvalues corresponding to the Mathieu functions $ce_l(u, -q)$ and $se_l(u, -q)$ [10]. The fundamental system of solutions to Eq. (6) is given by the functions $\varphi_{\mathcal{P}}^{(\pm)} = \tilde{D}_{\mathcal{P}}^{(\pm)}\exp(\pm(\mu + i\mathcal{P})u)$ orthonormalized to πmN, where $\mu(q, \mathcal{P})$ is the characteristic index, $\mathrm{Im}\,\mu = 0$, $\tilde{D}_{\mathcal{P}}^{(\pm)}(u, q) = \sum_r (-1)^r C_r^{(l)}(q)\exp(\pm i(r - l)u)$, and $C_r^{(l)}(q)$ are the known coefficients [10]. Let us represent $\mathcal{P} = l + \beta$, where l is the integral part of $\mathcal{P}$, $1 > \beta$, $\beta = 2g/mN$, and g are integers. In the tunnel solution to Eq. (6) $\varphi_{\mathcal{P}} = \xi_1\varphi_{\mathcal{P}}^{(+)} + \xi_2\varphi_{\mathcal{P}}^{(-)}$, we retain both terms if the condition for quantum parametric resonance $\mu \lesssim 1/\Delta u$ is fulfilled. To determine $\xi_{1,2}$, we solve, instead of the boundary-value problem, the equivalent time-dependent problem [6] through matching $\tilde{\chi}_{\mathrm{in}}^{(\pm)}$ and χ (3) with $\varphi = \varphi_{\mathcal{P}}$ at $\tau = 0$. Using the orthogonality conditions, we obtain for the wave functions of the $\mathcal{P}^+$ particles

$$\xi_1^{(+)} = \xi G_l^{(+)}, \quad \xi_2^{(+)} = \xi\frac{\mu}{\mu - i\mathcal{P}}G_l^{(-)},$$

$$\xi = c_{\mathcal{P}}^{(\pm)}\left(\frac{2\tanh\left(\frac{1}{2}\mu\pi mN\right)}{\mu\pi mN}\right)^{1/2},$$

$$G_l^{(+)} = C_l^{(l)}(q) + \mu\sum_{r\neq l}(-1)^r\frac{C_r^{(l)}(q)}{\mu - i(r-l)},$$

$$G_l^{(-)} = C_l^{(l)}(q) + (\mu - i\mathcal{P})\sum_{r\neq l}(-1)^r\frac{C_r^{(l)}(q)}{\mu - i(r-l)}.$$

For the wave functions of the $\mathcal{P}^-$ particles, $\xi_1^{(-)} = \xi_2^{(+)}$ and $\xi_2^{(-)} = \xi^{(+)}$.

Substituting $\varphi_{\mathcal{P}}$ into Eq. (4) and returning to z and t, we obtain the desired wave functions of the tunnel nonstationary states in the form of a decomposition in the plane waves $\psi_{\mathcal{P}}^{(\pm)}(z)$:

$$\Psi_{n,\sigma,\mathcal{P}} = \mathcal{K}_{n,\sigma}^{cl-lc}\left[\xi_1^{(+)}D_{\mathcal{P}}^{(+)}\exp\left(\frac{1}{2}(\mu k_m z - \Gamma_{\mathcal{P}}t)\right)\psi_{\mathcal{P}}^{(+)}(z)\right.$$
$$\times\exp(-i\Omega_{\mathcal{P}}^{(+)}t) + \xi_2^{(+)}D_{\mathcal{P}}^{(-)} \qquad (9)$$
$$\left.\times\exp\left(-\frac{1}{2}(\mu k_m z - \Gamma_{\mathcal{P}}t)\right)\psi_{\mathcal{P}}^{(-)}(z)\exp(-i\Omega_{\mathcal{P}}^{(-)}t)\right],$$

where $\mathcal{K}_{n,\sigma}^{cl-lc} = \psi_{n,\sigma}\psi_{cl-lc}$, $\Gamma_{\mathcal{P}}(q, \omega) = \omega\mu$ is the decay constant of the $|\mathcal{P}^+\rangle$ state (growth increment for the $|\mathcal{P}^-\rangle$ state), and $D_{\mathcal{P}}^{(\pm)}$ is equal to $\tilde{D}_{\mathcal{P}}^{(\pm)}$ with the multipliers containing coefficients η_m that arise upon passing from u, τ to z, t.

A twofold degenerate (according to the symmetry of the potential $W_m(u)$ in the comoving system of coordinates) $E'_{\mathcal{P}}$ level in the field of resonance wave (accidental degeneracy) splits into two levels upon passing to the laboratory frame: $E_{\mathcal{P}}^{(+)} > E_{sh}$ and $E_{\mathcal{P}}^{(-)} < E_{sh}$. The spontaneous transition frequency is $(\Delta\omega)_{\mathcal{P}} = \Omega_{\mathcal{P}}^{(+)} - \Omega_{\mathcal{P}}^{(-)} = \omega\mathcal{P}$. By averaging $\tilde{D}_{\mathcal{P}}^{(\pm)}$ on πmN, so that $\bar{\bar{D}}_{\mathcal{P}}^{(\pm)} = C_l^{(l)}(q)$, ignoring the derivative of $\mathcal{K}_{n,\sigma}^{cl-lc}$ with respect to t, as was done when deriving Eq. (4), and using the relation between z and t, we obtain the following expression for the spontaneous radiation power of an individual particle [11]:

$$M_{n,\sigma,\mathcal{P}} = -\frac{1}{2}\hbar\omega\mathcal{P}\frac{\partial}{\partial t}(Y_{\mathcal{P}}^{(+)} - Y_{\mathcal{P}}^{(-)})$$
$$= \frac{\hbar\omega^2\mu}{2\pi mN}\mathcal{P}\left|C_l^{(l)}(q)\right|^2\left|\mathcal{K}_{n,\sigma}^{cl-lc}\right|^2\left(\left|\xi_1^{(+)}\right|^2\exp(2\mu u)\right.$$
$$\left.+\left|\xi_2^{(+)}\right|^2\exp(-2\mu u)\right),$$

where

$$Y_{\mathcal{P}}^{(\pm)} = \left|C_{\mathcal{P}}^{(\pm)}\right|^2\left|\xi_1^{(+)}\right|^2\left|\bar{\tilde{D}}_{\mathcal{P}}^{(\pm)}\right|^2\left|\mathcal{K}_{n,\sigma}^{cl-lc}\right|^2\exp(\pm 2\mu u)$$

are the average populations of the $E_{\mathcal{P}}^{(\pm)}$ levels; $M_{n,\sigma,\mathcal{P}}$ is determined classically, because $\hbar\omega\mathcal{P} = 4\alpha E_{sh}$.

The oscillation in the presence of electron–wave interaction is caused by the population inversion of the $E_{\mathcal{P}}^{(\pm)}$ levels pumped by an external source. The absorption power of the $\mathcal{P}^-$ particles is $-M_{n,\sigma,\mathcal{P}}$. Since $C_l^{(l)}(q)$ is a sign-variable nonperiodical function of q [10], the oscillation may be quenched "accidentally" at the zeros of this function.

Is was found experimentally that the spectrum of generated frequencies has the form of bands [4] alternating with the bands where the oscillation is absent. We assume that such a spectrum is caused by the thermal straggling of the $\mathcal{P}$ numbers in the beam. Indeed, the particle–wave resonance has a finite width. Using the quantization conditions for $\mathcal{P}$ numbers and the relation between $\mathcal{P}$ and α (which can be obtained using the definition of $k^{(\pm)}$ to represent the $\mathcal{P}$ number as $2\Delta k/k_m$, after which, by writing $\alpha = \Delta k/k_{sh}$, where $\Delta k = k - k_{sh}$, one obtains $\alpha = \mathcal{P}/\mathcal{P}_{sh}$), we find the minimal value of $\alpha \neq 0$ for $h = 1$: $\alpha_{min} = 2/mN\mathcal{P}_{sh}$. Since the phase velocities of the $m \pm 1$ harmonics are $v_{m\pm1} = mv_m/(m \pm 1)$, one has $v|\alpha_{m-1}| > |\alpha_{m+1}|$ for identical velocities v ($\alpha_{m\pm1}$ is the relative velocity mismatch with the $m \pm 1$ wave). Putting $\alpha = -\alpha_{m+1}$, we obtain the velocity for a particle at resonance with the m and $m + 1$ harmonics: $v_{max} = 2mv_m/(2m + 1)$. It follows that the maximal $\alpha_{max} \lesssim 1/(2m + 1)$. Hence, the straggling of $\mathcal{P}$ numbers in the beam of particles resonant to the mth wave is

$$\frac{\mathcal{P}_{sh}}{2m+1} \gtrsim |\mathcal{P}| \geq \frac{2}{mN}. \qquad (10)$$

For the $\mathcal{P}$ numbers satisfying Eq. (10) and lying within $a_{2s+1} > \mathcal{P}^2 > a_{2s}$ and $b_{2s+2} > \mathcal{P}^2 > b_{2s+1}$ [10], the incident particles with energies

$$\frac{\hbar^2}{2m_e^*}a_{2s+1} > E'_{\mathcal{P}} > \frac{\hbar^2}{2m_e^*}a_{2s},$$

$$\frac{\hbar^2}{2m_e^*}b_{2s+2} > E'_{\mathcal{P}} > \frac{\hbar^2}{2m_e^*}b_{2s+1}$$

belonging to the allowed energy bands in the periodic potential pass through the barrier without resonance-induced energy dissipation. We call these states the overbarrier states.

The energies $E'_{\mathcal{P}}$ of a beam of resonant $\mathcal{P}^{\pm}$ particles with $\mathcal{P}$-number straggling given by Eq. (10) form the alternating energy bands of the overbarrier and tunnel states positioned symmetrically about E_{sh}. Accordingly, the frequency spectrum generated by a beam with thermal straggling of $\mathcal{P}$ numbers also has the form of bands, because the oscillation regions with widths $\omega\sqrt{b_{2s+1}} > (\Delta\omega)_{\mathcal{P}} > \omega\sqrt{a_{2s+1}}$ and $\omega\sqrt{a_{2s}} > (\Delta\omega)_{\mathcal{P}} > \omega\sqrt{b_{2s}}$ [see Eq. (8)] alternate with the gaps $\omega\sqrt{a_{2s+1}} > (\Delta\omega)_{\mathcal{P}} > \omega\sqrt{a_{2s}}$ and $\omega\sqrt{b_{2s+2}} > (\Delta\omega)_{\mathcal{P}} > \omega\sqrt{b_{2s+1}}$, where the oscillation does not occur.

A change in the position of resonator mirrors [4] does not change the oscillation frequencies; it merely changes the frequency of the orotron oscillatory circuit to extract the desired harmonic. The frequency tuning can be caused by changing the accelerating voltage in the case of a mono- or quasi-monoenergetic beam with $\mathcal{P}$-number straggling not exceeding the widths given by Eq. (8). In this case, the frequency is tuned jumpwise through the radiationless transition from one band of quantum parametric resonance to another, and it changes "smoothly" within the bands because the β manifold is quasi-discrete.

The gap widths decrease with increasing q, and the gaps become asymptotically narrow, because $a_{2s+1} \sim a_{2s}$ and $b_{2s+2} \sim b_{2s+1}$ at $|q| \gg 1$ [10]; accordingly, the oscillation bandwidths, i.e., the range of generated frequencies, increase. The number of bands l_{max} is equal to the integral part of $\mathcal{P}_{max} = \mathcal{P}_{sh}/(2m + 1)$ [see Eq. (10)]. The maximal oscillation frequency is $-\omega_{max} \lesssim \omega\mathcal{P}_{sh}/(2m + 1)$, and the minimal frequency is $\omega_{min} = 2\omega/mN$. Evidently, the beam radiation in the states with different m, σ and equal $\mathcal{P}$ numbers within the interval (10) is coherent, as is the radiation of particles with equal $\mathcal{P}$ but different x_0, y_0. The intensity of coherent radiation increases with the number of particles having the same $\mathcal{P}$ number. This may be accomplished by increasing the beam volume, i.e., its thickness [8] and width.

The radiation power of an individual particle increases with ω and $\mathcal{P}$. However, as $\mathcal{P}$ increases, while q, ω = const, the oscillation bandwidths and the value of μ decrease (cf. stability diagram for the solutions to the Mathieu equation [10]), thereby reducing the coherent radiation power because of a decrease in μ and in the number of particles occurring in the tunnel states, as happens in the Smith–Purcell effect (low-intensity coherent radiation from the narrow tunnel bands with $\mathcal{P} \gg 1$ and large numbers $l \gg 1$).

The particles pass through the barrier without dissipation of the longitudinal energy in the velocity-matched states ($\mathcal{P} = 0$), whose wave functions can be obtained from Eq. (4) with φ = const = 1, $u = 0$, and $W_n = er_m$. Then,

$$\Psi_{n,\sigma,0} = \mathcal{K}_{n,\sigma}^{cl-lc}\exp\left(i\left(k_{sh}z - \left(\Omega_{sh} + \frac{1}{\hbar}er_m\right)t\right)\right). \qquad (11)$$

4. The charge density [9] for the particles with $\mathcal{P} \neq 0$ is $\rho_{n,\sigma,\mathcal{P}} = \rho_{n,\sigma,0}\rho_{\mathcal{P}}$, where $\rho_{n,\sigma,0} = e\left|\mathcal{K}_{n,\sigma}^{cl-lc}\right|^2 = e|\Psi_{n,\sigma,0}|$ is the charge density for $\mathcal{P} = 0$ (11), $\rho_{\mathcal{P}} = |\psi_{\mathcal{P}}|^2$, and $\psi_{\mathcal{P}}$ are the functions from Eq. (9) without $\mathcal{K}_{n,\sigma}^{cl-lc}$. Because $\left|\mathcal{K}_{n,\sigma}^{cl-lc}\right|^2$ is the envelope for any $\rho_{\mathcal{P}}$, the modulation caused by the characteristic interactions in the system is independent of the particle state in the field of the resonant wave. For instance, if the interaction with the cloud of nonresonant harmonics dominates, the beam "shrinks" at the minima of $|\psi_{cl}|^2$ (7) to form bunches ("large" particles with the modulation wavelength $\lambda_m = cl/m$ starting at the time t_0).

In the bunch $\rho_{\mathcal{P}} = \rho_{\mathcal{P}}^{st} + \rho_{\mathcal{P}}^{(+)} + \rho_{\mathcal{P}}^{(-)}$, where

$$\rho_{\mathcal{P}}^{st} = |c_{\mathcal{P}}|^2 |\xi_1||\xi_2| \left|\tilde{D}_{\mathcal{P}}^{(+)}\right| \left|\tilde{D}_{\mathcal{P}}^{(-)}\right| \cos 2(\mathcal{P}u + \eta_D),$$

$$\rho_{\mathcal{P}}^{(\pm)} = |c_{\mathcal{P}}|^2 |\xi_{1,2}|^2 \left|\tilde{D}_{\mathcal{P}}^{(\pm)}\right|^2 \exp(\pm(\mu k_m z - \Gamma_{\mathcal{P}} t)),$$

$$\eta_d = \frac{1}{2}\arg \xi_1 \tilde{D}_{\mathcal{P}}^{(+)} (\xi_2 \tilde{D}_{\mathcal{P}}^{(-)})^*,$$

i.e., along with $\rho_{n,\sigma,0}$, the beam contains a stable interference fraction with charge density $\rho_{\mathcal{P}}^{st}$ for any q and two unstable tunneling fractions with densities $\rho_{\mathcal{P}}^{(\pm)}$. The beam instability in the states $|n, \sigma, \mathcal{P} = \text{const}\rangle$ (9) with the increment and decrement $\Gamma_{\mathcal{P}}(q, \omega)$ is caused by the quantum parametric resonance.

In the expression for the longitudinal current-density component j [9], we ignore $\frac{\partial}{\partial \tau}\mathcal{H}_{n,\sigma}^{cl-lc}$ and pass on to $\partial/\partial u$. Then

$$j_{n,\sigma,\mathcal{P}} = i\frac{e v_{\text{sh}}}{2\mathcal{P}_{\text{sh}}} \left|\mathcal{H}_{n,\sigma}^{cl-lc}\right|^2 \left(\psi_{\mathcal{P}}^* \frac{\partial}{\partial n}\psi_T - \text{c.c.}\right).$$

Setting $v_{\text{sh}} = eT_m U/2m_e L$, where $T_m = L/v_{\text{sh}}$ and U is the accelerating voltage, we arrive at the Ohm's law for the system considered:

$$j_{n,\sigma,\mathcal{P}} = \Lambda_{n,\sigma,\mathcal{P}} U,$$

where

$$\Lambda_{n,\sigma,\mathcal{P}} = \Lambda_{n,\sigma,0}\Lambda_{\mathcal{P}}, \quad \Lambda_{n,\sigma,0} = \frac{e^2 T_m}{2m_e L}\left|\mathcal{H}_{n,\sigma}^{cl-lc}\right|$$

is the electrical conductivity determined by the characteristic interactions. The conductivity caused by the resonant electron–wave interaction is

$$\Lambda_{\mathcal{P}} = \frac{i}{2}\left(\psi_{\mathcal{P}}^* \frac{\partial}{\partial n}\psi_{\mathcal{P}} - \text{c.c.}\right) = \Lambda_{\mathcal{P}}^{st} + \Lambda_{\mathcal{P}}^{(+)} + \Lambda_{\mathcal{P}}^{(-)},$$

where

$$\Lambda_{\mathcal{P}}^{st} = \left|C_l^{(l)}(q)\right|^2 |\xi_1||\xi_2| \sqrt{1 + \left(\frac{\mu}{\mathcal{P}_{\text{sh}}}\right)^2} \sin^2(\mathcal{P}u + \eta_{\xi,\mu}),$$

$$\Lambda_{\mathcal{P}}^{(\pm)} = \left|C_l^{(l)}(q)\right|^2 |\xi_{1,2}|^2 (1 \pm \alpha)\exp(\pm 2\mu u),$$

$$\eta_{\xi,\mu} = \frac{1}{2}\left(\arg \xi_1 \xi_2^* + \arctan\frac{\mu}{\mathcal{P}_{\text{sh}}}\right)$$

are the conductivities $\Lambda_{n,\sigma,0}$ and $\Lambda_{\mathcal{P}}^{st}$ for the stable fractions of current density $j_{n,\sigma,0}$ and $j_{\mathcal{P}}^{st}$ and the conductivities $\Lambda_{\mathcal{P}}^{(\pm)}$ for the two unstable fractions.

5. The resonance states obtained in this work can be found in other systems as well. The "memory" of the system is contained in the $\mathcal{H}$ function; the latter differs, e.g., from the solid-state $\mathcal{H}$ function, in particular, by the cloud effect, whose potentials are expanded in the time-dependent harmonics, as opposed to Eq. (1). The wave functions of the resonant positively charged particles have the same form, but u is replaced by $u + \pi/2$.

REFERENCES

1. I. M. Frank, Izv. Akad. Nauk SSSR, Ser. Fiz. **6**, 3 (1942); V. L. Ginzburg and I. M. Frank, Zh. Éksp. Teor. Fiz. **16**, 15 (1946).
2. S. L. Smith and M. Purceell, Phys. Rev. **91**, 1069 (1953).
3. F. S. Rusin and R. D. Bogomolov, Izv. Vyssh. Uchebn. Zaved., Radiofiz. **11**, 756 (1968).
4. V. P. Shestopalov, *Diffraction Electronics* (Khar'k. Gos. Univ., Khar'kov, 1976).
5. E. M. Lifshitz and L. P. Pitaevskiĭ, *Course of Theoretical Physics*, Vol. 10: *Physical Kinetics* (Nauka, Moscow, 1979; Pergamon, Oxford, 1981).
6. M. V. Fedorov, Usp. Fiz. Nauk **153**, 213 (1981) [Sov. Phys. Usp. **24**, 801 (1981)].
7. Yu. A. Pobedin, Zh. Éksp. Teor. Fiz. **96**, 1476 (1990) [Sov. Phys. JETP **70**, 833 (1990)]; Pis'ma Zh. Tekh. Fiz. **18** (3), 78 (1992) [Sov. Tech. Phys. Lett. **18**, 89 (1992)].
8. D. B. Chang and G. C. McDaniel, Phys. Rev. Lett. **63**, 1066 (1989).
9. L. D. Landau and E. M. Lifshitz, *Course of Theoretical Physics*, Vol. 3: *Quantum Mechanics: Non-Relativistic Theory* (Nauka, Moscow, 1963; Pergamon, New York, 1977).
10. N. W. McLachlan, *Theory and Application of Mathieu Functions* (Clarendon, Oxford, 1947; Inostrannaya Literatura, Moscow, 1963).
11. R. H. Pantell and H. E. Puthoff, *Fundamentals of Quantum Electronics* (Wiley, New York, 1969; Mir, Moscow, 1972).

Translated by V. Sakun

JETP Letters, Vol. 75, No. 12, 2002, pp. 631–634. Translated from Pis'ma v Zhurnal Éksperimental'noĭ i Teoreticheskoĭ Fiziki, Vol. 75, No. 12, 2002, pp. 756–759.

Fluctuation Interaction of Ising Subsystems

V. M. Rozenbaum* and A. N. Morozov

Institute of Surface Chemistry, National Academy of Sciences of Ukraine, Kiev, 03164 Ukraine

**e-mail: vrozen@mail.kar.net*

Received April 26, 2002

A phase diagram of two Ising subsystems σ and *s* has been constructed on a Bethe lattice with a coordination number 4 (a simplified analog of a square lattice). In contrast to the known Ashkin–Teller model, the interaction between these two subsystems is of a purely fluctuational nature; i.e., it does not manifest itself in the ground state and nullifies the sums of the products of average spins $\langle\sigma\rangle\langle s\rangle$ (interactions of this type are realized in lattice-type adsorbed systems with dipolelike intermolecular interactions and strong azimuthal angular dependence of the adsorption potential of symmetry C_4). Apart from conventional states, i.e., a high-temperature disordered state ($\langle\sigma\rangle = \langle s\rangle = 0$) and a low-temperature ordered state ($\langle\sigma\rangle$ and $\langle s\rangle \neq 0$), this system can also exist in a correlated state ($\langle\sigma s\rangle \neq 0$ at $\langle\sigma\rangle = \langle s\rangle = 0$). In the theory of orientational phase transitions, this state corresponds to a fundamentally different, intermediate (on the temperature axis) phase in which a preferred direction of long molecule axes arises in the absence of spontaneous polarization. The results of Monte Carlo simulation on a square lattice agree with the conclusions obtained on a Bethe lattice. The characteristics of the orientational phase transition in a 2×1 monolayer of CO molecules adsorbed on the NaCl(100) surface are discussed. © *2002 MAIK "Nauka/Interperiodica".*

PACS numbers: 64.60.Cn; 68.35.Rh; 05.50.+q

The simplest example of a system with fluctuation interactions is a square lattice with sites *nm* each containing two spin variables $\sigma_{nm} = \pm 1$ and $s_{nm} = \pm 1$ and interactions between nearest-neighbor sites that are described by the Hamiltonian [1]

$$H = \sum_{nm} [-J_1(\sigma_{nm}\sigma_{n,m+1} + s_{nm}s_{n,m+1} + \sigma_{nm}\sigma_{n+1,m} + s_{nm}s_{n+1,m}) - J_2(\sigma_{nm}s_{n,m+1} + s_{nm}\sigma_{n,m+1} - \sigma_{nm}s_{n+1,m} - s_{nm}\sigma_{n+1,m})]. \quad (1)$$

The ground state of this Hamiltonian $H_0 = -4NJ_1$ (N is the number of lattice sites) at $J_1 \geq J_2 \geq 0$ is independent of the interaction constant J_2 of spins of the different sublattices. Attempts to analyze the states of such a system in terms of the self-consistent-field (SCF) approximation without allowance for the interactions of thermodynamic fluctuations fail completely, since the sum of the products of average spins $\langle\sigma\rangle\langle s\rangle$ vanishes and the result is independent of J_2. Therefore, the interactions of the spin subsystems σ and *s* that are described by Hamiltonian (1) will be called fluctuational. While discussing models with interacting Ising subsystems, one cannot but mention the well-known isotropic Ashkin–Teller model [2]

$$H_{AT} = \sum_{nm} [-J_1(\sigma_{nm}\sigma_{n,m+1} + s_{nm}s_{n,m+1} + \sigma_{nm}\sigma_{n+1,m} + s_{nm}s_{n+1,m}) - J_4(\sigma_{nm}s_{nm}s_{n,m+1}\sigma_{n,m+1} + \sigma_{nm}s_{nm}\sigma_{n+1,m}s_{n+1,m})]. \quad (2)$$

The main features of the phase diagram of this model can be reproduced even in the SCF approximation [3, 4].

The systems with fluctuation interaction of type (1) are discrete analogs of a wider class of systems with a continuously degenerate ground state, which include the dipole short-range interaction model [5]

$$H_{Dip} = \sum_{nm} [D_1(\mathbf{e}_{nm}\mathbf{e}_{n,m+1} + \mathbf{e}_{nm}\mathbf{e}_{n+1,m}) + D_2(e^x_{nm}e^x_{n,m+1} + e^y_{nm}e^y_{n+1,m})]. \quad (3)$$

Here, $\mathbf{e}_{nm}$ are unit vectors and e^x_{nm} and e^y_{nm} are their projections onto the axes of the square lattice. The degenerate ground state $H_0 = -N|D_2|$ is realized at $0 < D_1 < -D_2$. This case corresponds to the parameters of the real dipole interaction $D_1 = \mu_2/a^3$ and $D_2 = -2\mu^2/a^3$ (where μ is the dipole moment and *a* is the lattice parameter) [6–8] or to the parameters of quadrupole interactions $D_1 = 3Q^2\sin^2 2\theta/4a^5$, $D_2 = -15Q^2\sin^2 2\theta/4a^5$ (Q is the quadrupole moment) of nonpolar molecules oriented quasi-normally to the surface plane (at a small angle θ to its normal) [1]. In the systems of adsorbed molecules with a strong azimuthal angular dependence of the adsorption potential of symmetry C_4, only four discrete orientations of vectors $\mathbf{e}_{nm}$ along the axes of the square lattice (as, e.g., in the 2×1 monolayer of CO molecules adsorbed on the NaCl(100) surface [9]) can prove to be acceptable. If the orientations of $\mathbf{e}_{nm}$ are

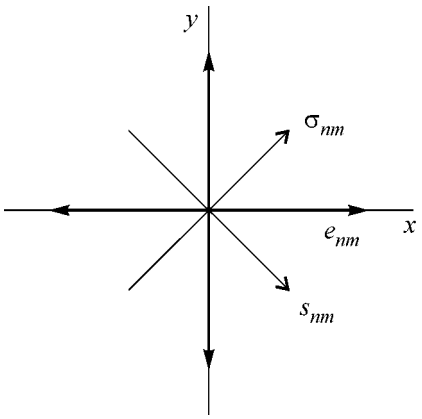

Fig. 1. Correspondence of four orientations of vectors $\mathbf{e}_{nm}$ to four pairs of values of spin variables $\sigma_{nm} = \pm 1$ and $s_{nm} = \pm 1$ (schematic).

characterized by spin variables σ_{nm} and s_{nm} (Fig. 1),

$$\mathbf{e}_{nm} = \frac{1}{2}((-1)^n(\sigma_{nm} + s_{nm}), (-1)^m(\sigma_{nm} - s_{nm}), 0), \quad (4)$$

then Hamiltonian (3) reduces to (1) with $J_1 = -D_2/4$ and $J_2 = -D_2/4 - D_1/2$. At the orientations of $\mathbf{e}_{nm}$ along the diagonals of the square lattice, i.e., $\mathbf{e}_{nm} = 2^{-1/2}((-1)^n\sigma_{nm}, (-1)^m s_{nm}, 0)$, the case of noninteracting Ising subsystems [10] is realized.

Thus, Hamiltonian (1) determines not only a new and interesting model in the theory of phase transitions but also has concrete applications in the investigation of orientational states of lattice systems of adsorbed molecules. Since the exact solution for such a model on a square lattice is not available and since the SCF approximation cannot describe fluctuation interactions, it is natural to resort to a corresponding model on a Bethe lattice (according to the known Baxter approach [4], solutions obtained for this lattice can be considered to be exact). A Monte Carlo simulation permits one to control to what extent such a description corresponds to a square lattice. The results obtained using these approaches are presented in this paper.

The partition function for Hamiltonian (1) on a Bethe lattice with a coordination number equal to four can be written as

$$Z = \sum_{i=1}^{4} x_i^2 y_i^2, \quad (5)$$

where the magnitudes of x_i and y_i for the sites located deep in a Cayley tree (i.e., at an infinitely far distance from its boundary) are determined by the set of equations

$$x_i = \sum_{j=1}^{4} \Lambda_{ij}^{(x)} x_j y_j^2, \quad y_i = \sum_{j=1}^{4} \Lambda_{ij}^{(y)} y_j x_j^2. \quad (6)$$

The indices $i, j = 1, 2, 3, 4$ here correspond to the following values of the pairs of spin variables σ and s: +1, +1; –1, –1; +1, –1; and –1, +1. The matrices $\Lambda^{(x)}$ and $\Lambda^{(y)}$ of 4×4 dimension have a block form:

$$\Lambda^{(x)} = \begin{pmatrix} A & C \\ C & B \end{pmatrix}, \quad \Lambda^{(y)} = \begin{pmatrix} B & C \\ C & A \end{pmatrix},$$

$$A = \begin{pmatrix} e^{2(K_1+K_2)} & e^{-2(K_1+K_2)} \\ e^{-2(K_1+K_2)} & e^{2(K_1+K_2)} \end{pmatrix}, \quad (7)$$

$$B = \begin{pmatrix} e^{2(K_1-K_2)} & e^{-2(K_1-K_2)} \\ e^{-2(K_1-K_2)} & e^{2(K_1-K_2)} \end{pmatrix}, \quad C = \begin{pmatrix} 1 & 1 \\ 1 & 1 \end{pmatrix},$$

where $K_{1,2} = J_{1,2}/k_B T$ (k_B is the Boltzmann constant and T is the absolute temperature). The average values of spin variables are determined by the equations

$$\langle\sigma\rangle = Z^{-1}\sum_{i=1}^{4} \sigma_i x_i^2 y_i^2, \quad \langle s\rangle = Z^{-1}\sum_{i=1}^{4} s_i x_i^2 y_i^2,$$
$$\langle\sigma s\rangle = Z^{-1}\sum_{i=1}^{4} \sigma_i s_i x_i^2 y_i^2. \quad (8)$$

Note first of all that the symmetry of the problem provides for the equality $\langle\sigma\rangle = \pm\langle s\rangle$. Without loss of generality, we can assume that $\langle\sigma\rangle = \langle s\rangle$ and, thereby, at $\langle\sigma\rangle = \langle s\rangle > 0$, the right-hand orientation of the average values of the vectors $\mathbf{e}_{nm}$ in Fig. 1 becomes preferred. In this case, $x_3 = x_4$ and $y_3 = y_4$. The condition $\langle\sigma\rangle = \langle s\rangle = 0$ is met for one more pair of equalities, namely, $x_1 = x_2$ and $y_1 = y_2$. After applying the additional requirement that $\langle\sigma s\rangle = 0$, we have $x_1 = x_2 = y_3 = y_4$ and $x_3 = x_4 = y_1 = y_2$.

To analyze solution to the set of equations (6), it is convenient to deal with eigenvalues of the matrices $\Lambda^{(x)}$ and $\Lambda^{(y)}$

$$\lambda_1 = a_1, \quad \lambda_2 = b_1,$$
$$\lambda_{3,4} = \frac{1}{2}[a_2 + b_2 \mp \sqrt{(a_2 - b_2)^2 + 16}], \quad (9)$$

which are expressed through the eigenvalues of the matrices A and B

$$a_1 = 2\sinh 2(K_1 + K_3), \quad a_2 = 2\cosh 2(K_1 + K_3),$$
$$b_1 = 2\sinh 2(K_1 - K_3), \quad b_2 = 2\cosh 2(K_1 - K_3). \quad (10)$$

In addition, it is convenient to designate the ratios of the variables x_i and y_i as

$$\xi_{ij} = x_i/x_j, \quad \eta_{ij} = y_i/y_j \tag{11}$$

($\xi_{34} = \eta_{34} = 1$ in view of the condition $x_3 = x_4$, $y_3 = y_4$ assumed above) and to introduce the parameters

$$\gamma_{3,4} = \frac{1}{4}[\sqrt{(a_2 - b_2)^2 + 16} \pm (a_2 - b_2)],$$
$$\varphi = \frac{\xi_{31}^2 + \gamma_4\eta_{24}}{1 + \gamma_4\eta_{24}}, \quad \psi = \frac{\eta_{24}^2 + \gamma_4\xi_{31}}{1 + \gamma_4\xi_{31}}. \tag{12}$$

In these designations, the solution corresponding to the case $\langle\sigma\rangle = \langle s\rangle = \langle\sigma s\rangle = 0$ takes on the form

$$\xi_{21} = \eta_{12} = 0, \quad \xi_{31}^2 = \eta_{24}^2 = \frac{\lambda_3\gamma_3 + \lambda_4\gamma_4}{\lambda_3\gamma_4 + \lambda_4\gamma_3} = \frac{b_2}{a_2},$$
$$x_1^2 = y_4^2 = (\lambda_4\varphi)^{-1}. \tag{13}$$

In the range of values $a_2b_2 \geq 16$, i.e., at sufficiently low temperatures, there exists another solution with $\langle\sigma\rangle = \langle s\rangle = 0$ and $\langle\sigma s\rangle \neq 0$, namely,

$$\xi_{21} = \eta_{12} = 0, \quad \xi_{31}\eta_{24} = \frac{1}{4}\sqrt{\frac{b_2}{a_2}}(\sqrt{a_2b_2} \mp \sqrt{a_2b_2 - 16}),$$
$$x_1^2 = (\lambda_4\varphi)^{-1}, \quad y_4^2 = (\lambda_4\psi)^{-1}, \tag{14}$$
$$\langle\sigma s\rangle = \frac{\eta_{34}^2 - \xi_{31}^2}{\eta_{34}^2 + \xi_{31}^2} \geq 0.$$

Solutions with $\langle\sigma\rangle = \langle s\rangle \geq 0$ arise when the condition

$$\lambda_4^2\varphi\psi - (\lambda_1\eta_{24}^2\varphi + \lambda_2\psi)\lambda_4 - 3\lambda_1\lambda_2\eta_{24}^2 = 0 \tag{15}$$

is fulfilled if ξ_{21} and η_{12} tend to unity according to the laws

$$\xi_{21} \xrightarrow[\varepsilon \to 0]{} 1 - 2\varepsilon, \quad \eta_{12} \xrightarrow[\varepsilon \to 0]{} 1 + 2\delta\varepsilon,$$
$$\delta = \frac{2\lambda_2}{\lambda_4\varphi - \lambda_2}. \tag{16}$$

It is evident that if $a_2b_2 \leq 16$, we should introduce the values of ξ_{31} and η_{24} from Eq. (13) into Eqs. (15) and (16). In this case, Eq. (15) determines the line of the coexistence of a disordered high-temperature phase I and an ordered low-temperature phase II with $\langle\sigma\rangle = \langle s\rangle > 0$ (Fig. 2). When the condition $a_2b_2 > 16$ is fulfilled, we should substitute the values of ξ_{31} and η_{24} from Eq. (14) into Eqs. (15) and (16). Then, Eq. (15) determines the line of the coexistence of phases II and III and the condition $a_2b_2 = 16$ leads to the coexistence of phases III and I, where phase III is characterized by zero averages of $\langle\sigma\rangle$ and $\langle s\rangle$ but a nonzero value of $\langle\sigma s\rangle$. It is expedient to explain the physical meaning of this phase in terms of the average values of the vectors $\mathbf{e}_{nm}$ (see Fig. 1 and Eq. (4)): $\langle\mathbf{e}_{nm}\rangle = 0$, $\langle(e_{nm}^x)^2\rangle = (1 + \langle\sigma s\rangle)/2 > \langle(e_{nm}^y)^2\rangle = (1 - \langle\sigma s\rangle)/2$; i.e., no preferred orientation exists in the system, but the orientations parallel to the x axis are more preferable than those parallel to the y axis.

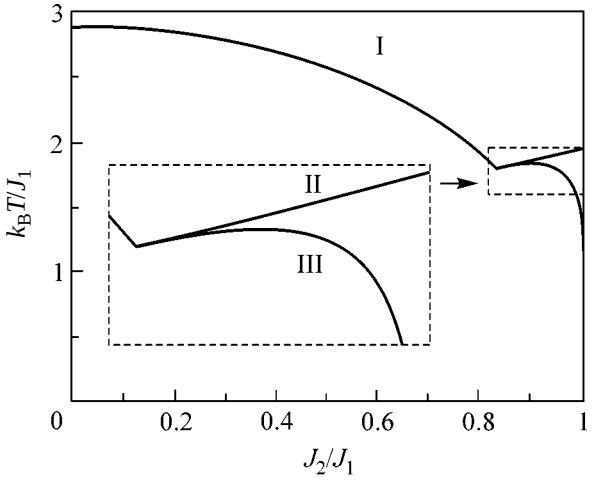

Fig. 2. Phase diagrams of two fluctuation-interacting Ising subsystems (1) on a Bethe lattice with a coordination number equal to 4. For phases I, II, and III, $\langle\sigma\rangle = \langle s\rangle = \langle\sigma s\rangle = 0$, $\langle\sigma\rangle = \langle s\rangle \neq 0$, and $\langle\sigma s\rangle \neq 0$ at $\langle\sigma\rangle = \langle s\rangle = 0$, respectively.

An analysis of the diagram given in Fig. 2 shows that the dimensionless temperatures $\tau \equiv k_BT/J_1$ of phase transitions I–II decrease from a value of 2.89 corresponding to the Ising model on the Bethe lattice ($\exp(2K_1) = 2$) to 1.79 at the point of coexistence of phases I, II, and III, where the ratio of the interactions $\kappa \equiv J_2/J_1$ takes on a value equal to 0.84. Phase III exists in the range of sufficiently large values of κ: $0.84 < \kappa < 1$. The dimensionless temperatures τ of the I–III and III–II phase transitions vary from 1.79 at the point of coexistence of the three phases to values equal to 1.94 and 0, respectively. The zero temperature of the transition into the phase with $\langle\mathbf{e}_{nm}\rangle = 0$ at $J_2 = J_1$ was noted in [1], but the appearance of phase III due to fluctuation interactions was not noticed in [1]. The results of Monte Carlo simulation on a square lattice, even for a relatively small cluster such as 10×10 with periodic boundary conditions, agree with the suggested phase diagram. The difference is only in the values of τ for the lines of phase transitions, which are always lower than on the Bethe lattice. The magnitude of τ decreases from 2.27 (a value characteristic of the Ising model on a square lattice ($\sinh 2K_1 = 1$)) to 1.8 at the point of coexistence of three phases and remains approximately constant along the I–III line. At $J_2 = J_1$ and $\tau < 1.8$, the conditions of existence of phase III are fulfilled: $\langle\sigma s\rangle > 0$, $\langle\sigma\rangle = \langle s\rangle = 0$.

For adsorbed systems with quasi-normal molecular orientations with respect to the surface plane, in which quadrupole intermolecular interactions are dominant,

the parameter κ is equal to 0.6; and the corresponding value of τ, according to Monte Carlo calculations, is equal to 2.1. Estimating the energy Q^2/a^5 of quadrupole interactions between neighboring CO molecules on the NaCl(100) surface as being equal to 1.63 meV [1] ($Q = 1.62 \times 10^{-26}$ esu and $a = 5.64/\sqrt{2}$ Å) and using the value $\theta \approx 25°$ for the experimentally determined slopes of molecules toward the normal to the surface [9], we obtain $J_1/k_B \approx 10.4$ K and $T_c \approx 22$ K. The disappearance of the Davydov splitting of spectrum lines characteristic of the low-temperature 2×1 orientational structure occurs in the temperature range of 17.5–21.5 K [11], which agrees well with the calculated value of T_c. This latter value can be refined by introducing an additional interaction of Ising subsystems of the Ashkin–Teller type (see (4)) with a negative coefficient J_4 ($J_4/J_1 = -0.207$ for CO/NaCl(100)) [1]. The investigation of the generalized Ashkin–Teller model with fluctuation interactions seems to be very promising, since in this model also, new phase states observed in real systems can be obtained.

REFERENCES

1. V. M. Rozenbaum and S. H. Lin, J. Chem. Phys. **112**, 9083 (2000).
2. J. Ashkin and E. Teller, Phys. Rev. **64**, 178 (1943).
3. R. V. Ditzian, J. R. Banavar, G. S. Grest, and L. P. Kadanoff, Phys. Rev. B **22**, 2542 (1980).
4. R. J. Baxter, *Exactly Solved Models in Statistical Mechanics* (Academic, London, 1982).
5. V. M. Rozenbaum, Zh. Éksp. Teor. Fiz. **111**, 669 (1997) [JETP **84**, 368 (1997)].
6. P. I. Belobrov, R. S. Gekht, and V. A. Ignatchenko, Zh. Éksp. Teor. Fiz. **84**, 1097 (1983) [Sov. Phys. JETP **57**, 636 (1983)].
7. V. M. Rozenbaum and V. M. Ogenko, Fiz. Tverd. Tela (Leningrad) **26**, 1448 (1984) [Sov. Phys. Solid State **26**, 877 (1984)].
8. S. Prakash and C. L. Henley, Phys. Rev. B **42**, 6574 (1990).
9. J. Heidberg, E. Kampshoff, R. Kühnemuth, *et al.*, Surf. Sci. **269/270**, 128 (1992).
10. V. M. Rozenbaum and V. M. Ogenko, Pis'ma Zh. Éksp. Teor. Fiz. **35**, 151 (1982) [JETP Lett. **35**, 184 (1982)].
11. J. Heidberg, M. Grunwald, M. Hustedt, and F. Traeger, Surf. Sci. **368**, 126 (1996).

Translated by S. Gorin

JETP Letters, Vol. 75, No. 12, 2002, pp. 635–637. Translated from Pis'ma v Zhurnal Éksperimental'noĭ i Teoreticheskoĭ Fiziki, Vol. 75, No. 12, 2002, pp. 760–762.

Nonergodic Dynamics of a System of Nuclear Spins 1/2 with Identical Spin–Spin Coupling Constants

M. G. Rudavets and É. B. Fel'dman*

Institute of Problems of Chemical Physics, Russian Academy of Sciences, Chernogolovka, Moscow region, 142432 Russia

** e-mail: feldman@icp.ac.ru*

Received April 29, 2002

The exact solution for the evolution of nuclear spin polarizations in a system with spin–spin coupling constant g identical for all spin pairs is obtained on the condition that only one (first) spin is polarized at zero time. It is shown that the polarization $P_1(t)$ of the first spin has the form of periodic time pulsations with the period $4\pi/g$. In every period, the function $P_1(t)$ changes from its initial value $P(0) = 1$ to 1/3 during the time on the order of $t \approx 4\pi/Ng$, if the number of spins $N \gg 1$, and remains in the state $P_1(t) = 1/3$ virtually during the entire period. A simple classical model within the framework of mean-field theory explains the physical nature of the nonergodic dynamics of the system. © *2002 MAIK "Nauka/Interperiodica".*

PACS numbers: 76.60.-k; 33.25.+k

The study of the long-time asymptotic behavior of the longitudinal spin order is of importance in gaining structural information on the crystalline and amorphous solids from the spin-diffusional NMR experiments [1]. In statistical physics, these studies are carried out by invoking the ergodic hypothesis [2], which allows the description [3] of the quasi-equilibrium state of a many- particle spin system. Although the use of the ergodic hypothesis is well justified in some cases (see, e.g., [4]), the numerical and analytic analyses of the one-dimensional dynamics of nuclear-spin systems with dipolar interaction have demonstrated [5–7] that the quasi-equilibrium states that are established in these systems in times from hundred microseconds to several milliseconds are nonergodic.

In this letter, the dynamics of a three-dimensional system of nuclear spins is studied in a constant magnetic field $\mathbf{H}_0$, whose direction specifies the z axis. The spin–spin coupling constant g is taken to be identical for all spin pairs. The Hamiltonian of this system has the form

$$H = \omega\sum_{n=1}^{N} I_{nz} + \frac{g}{2}\sum_{m\neq n}^{N}\{\zeta I_{mz}I_{nz} - I_{mx}I_{nx} - I_{my}I_{ny}\}, \quad (1)$$

where $\omega = \gamma H_0$, γ is the gyromagnetic ratio, N is the number of spins in the system, ζ is the arbitrary constant, and $I_{n\alpha}$ is the operator of projection of spin n onto the axis $\alpha = x, y, z$. At $N = 3$ or 4, this model describes the proton spin dynamics in the CH_3, CH_4, and NH_4Cl molecules. However, the main advantage of this model is that it provides the possibility of exactly treating the dynamics of a multispin system for any N. We assume that the density matrix $\sigma(t)$ at $t = 0$ corresponds to the high-temperature approximation [8] $\sigma(0) = I_{1z}$; i.e., the polarization at zero time is concentrated only on spin 1. The polarization of spin n at time t is given by the formula

$$P_n(t) = \mathrm{tr}\{e^{iHt}I_{1z}e^{-iHt}I_{nz}\}/\mathrm{tr}\{I_{1z}^2\}. \quad (2)$$

The correlation function in Eq. (2) does not change if Hamiltonian (1) is replaced by

$$H' = -\frac{g}{2}\mathbf{I}^2, \quad \mathbf{I} = \sum_{n=1}^{N}\mathbf{I}_n, \quad (3)$$

where $\mathbf{I}$ is the total spin of a cluster of N spins. Among the set of polarizations $P_n(t)$ (2), it is sufficient to calculate only the polarization $P_1(t)$ of spin 1, because the total polarization of all spins does not change with time; i.e., $\sum_{n=1}^{N} P_n(t) = 1$, and the polarizations of all spins, except for spin 1, are always equal to each other. So, we will calculate

$$P_1(\tau) = \mathrm{tr}\{e^{i\tau\mathbf{I}^2}I_{1z}e^{-i\tau\mathbf{I}^2}I_{1z}\}/\mathrm{tr}\{I_{1z}^2\}, \quad (4)$$

where the dimensionless time $\tau = \frac{1}{2}gt$ is introduced. Equation (4) is calculated by the method of coupled angular momenta [9]. With this method, the whole N-spin cluster is divided into two subsystems A and B. The subsystem A includes only spin 1, and the subsystem B includes the remaining $N - 1$ spins. The total

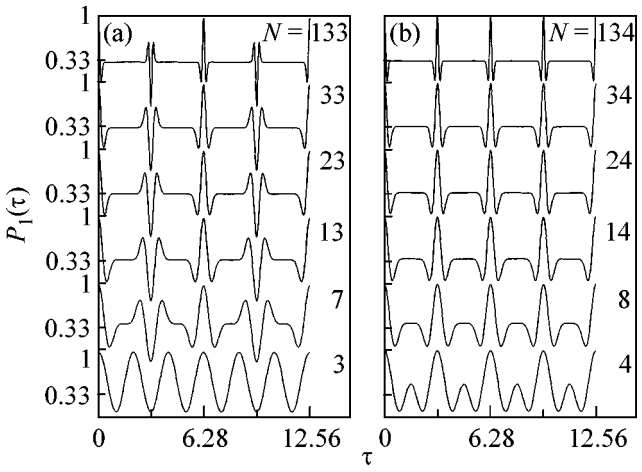

Fig. 1. Dependence of the polarization $P_1(\tau)$ of the first spin on the dimensionless time $\tau = gt/2$ for different numbers N of spins in the spin cluster: (a) odd N [Eq. (9)] and (b) even N [Eq. (11)].

spin of the system is $\mathbf{I} = \mathbf{I}_A + \mathbf{I}_B$. The quantum states $|I_A m_A\rangle$ and $|I_B m_B\rangle$ of the subsystems A and B are related to the state $|I_A, I_B, I, m\rangle$ of the whole N-spin cluster by the Clebsch–Gordan coefficients as [9, 10]

$$|I_A, I_B, I, m\rangle = \sum_{\substack{m_A = \pm\frac{1}{2} \\ m_B = m - m_A}} C^{Im}_{I_A m_A, I_B m_B} |I_A m_A\rangle |I_B m_B\rangle, \quad (5)$$

where $I_A = 1/2$ and $m_A = \pm 1/2$ are, respectively, the quantum numbers of spin 1 and its z component, and I_B and m_B are, respectively, the quantum numbers of the total spin and its z component for subsystem B. Making use of the fact that basis (5) is complete and orthonormalized at fixed $I_A = 1/2$ and I_B, one can write the correlation function $P_1(t)$ in Eq. (4) as

$$P_1(\tau) = 2^{-(N-2)} \sum_{I_B = I_B^{\min}}^{(N-1)/2} w(I_B) \times \sum_{\substack{\left|I_B - \frac{1}{2}\right| \le I \le \left|I_B + \frac{1}{2}\right| \\ \left|I_B - \frac{1}{2}\right| \le I' \le \left|I_B + \frac{1}{2}\right|}} \sum_{\substack{-I \le m \le I \\ -I' \le m' \le I'}} \delta_{m,m'} e^{i\tau\{I(I+1) - I'(I'+1)\}} \times \left(\sum_{m_A = \pm\frac{1}{2}} m_A C^{I'm'}_{\frac{1}{2} m_A, I_B m - m_A} C^{Im}_{\frac{1}{2} m_A, I_B m - m_A} \right)^2, \quad (6)$$

where

$$w(I_B) = \frac{2I_B + 1}{N} \binom{N}{I_B + (N+1)/2} \quad (7)$$

is the total number of m states in the subsystem B for a given spin I_B; $I_B^{\min} = 0$ for the odd number N of spins and $I_B^{\min} = 1/2$ for the even number N of spins [10]. The polarization $P_1(\tau)$ in Eq. (6) is the sum of the constant $\overline{P_1}$ and the oscillating $P_1^{\text{osc}}(\tau)$ parts:

$$P_1(\tau) = \overline{P_1} + P_1^{\text{osc}}(\tau). \quad (8)$$

For the odd number N of spins in the cluster, the sum in Eq. (6) is equal to

$$\overline{P_1} = \frac{N+2}{3N}, \qquad P_1^{\text{osc}}(\tau) = \sum_{k=0}^{(N-1)/2} A_k(N) \cos(\tau(N-2k)), \quad (9)$$

where

$$A_k(N) = \frac{2^{4-N}}{3N} \left(\frac{N+1}{2} - k\right)\left(\frac{N-1}{2} - k\right) \binom{N}{k}. \quad (10)$$

For the even number N of spins,

$$\overline{P_1} = \frac{N + 2 - 2^{1-N} \binom{N}{N/2}}{3N}, \qquad P_1^{\text{osc}}(\tau) = \sum_{k=0}^{N/2-1} A_k(N) \cos(\tau(N-2k)), \quad (11)$$

where the coefficient $A_k(N)$ is given by Eq. (10). The expression for $\overline{P_1}$ in Eq. (9) is presented without derivation in [6].

Equations (8)–(11) show that the time-averaged polarization

$$\overline{P_1} = \lim_{T \to \infty} \frac{1}{T} \int_0^T P_1(\tau) d\tau \quad (12)$$

of the first spin in the N-spin cluster is different from the polarization of each of the remaining spins. At $N \gg 1$, one-third of the initial polarization $P_1(0) = 1$ remains on the first spin, while the polarization of each of the remaining spins is $2/(3N)$. The intuitively anticipated equalization of the polarizations of all spins after a large time interval as a result of spin diffusion [11] does not occur in this model; i.e., the dynamics of the model is nonergodic. Figure 1a demonstrates the time evolution of the polarization $P_1(\tau)$ of the first spin in the clusters with an odd total number N of spins. In accordance with Eq. (9), the evolution of polarization $P_1(t)$ is periodic with period $4\pi/g$. At $N \gg 1$, the polarization $P_1(t)$ changes in time $t \approx 4\pi/Ng$ from the initial value $P_1(0) = 1$ to the stationary plateau, which is retained during

almost all the evolution period, except for the narrow time interval on the order of $t \approx 4\pi/Ng$. This stationary polarization virtually coincides with the average polarization given by Eq. (12). Due to the presence of the stationary plateau in the polarization profile and to the periodicity of polarization pulsation, the nonergodic behavior of polarization in this model is more pronounced than in the linear chains and rings of nuclear spins with the *XY* Hamiltonian [12, 13].

Figure 1b demonstrates the time evolution of the polarization $P_1(\tau)$ of the first spin in the clusters with an even total number N of spins. In this case, the period of function $P_1(t)$ in Eq. (11) is $2\pi/g$. The salient features of the function $P_1(t)$ are the same for the even and odd numbers N. At $N \longrightarrow \infty$, the average polarization $\overline{P_1(t)}$ on the first spin is always 1/3. The system dynamics is nonergodic for any N.

We now substantiate qualitatively the nonergodic dynamics by invoking a simple classical mean-field model for the spin systems with infinite-range interaction. Consider $N \gg 1$ classical moments coupled to each other by the infinite-range interaction. Each of the $N-1$ moments creates on the moment 1 the same field of order N^{-1}, and, hence, all $N-1$ moments create a finite field $O(1)$. To estimate $\overline{P_1(t)}$, we assume that $N-1$ moments create on the moment 1 the effective field $\mathbf{H}_{\text{ef}}(t)$, which is equally probable for all directions and has zero mean. By decomposing the polarization of moment 1 into the parallel $P_1^{\parallel}(t)$ and perpendicular $P_1^{\perp}(t)$ components with respect to $\mathbf{H}_{\text{ef}}(t)$, we find that, after averaging over the ensemble of N spin clusters, the contribution from the $P_1^{\perp}(t)$ components to the polarization on the moment 1 is zero, so that the polarization $\overline{P_1(t)}$ is determined only by the z projections of the $P_1^{\parallel}(t)$ components and equal to

$$\overline{P_1(t)} = \langle \cos^2\theta \rangle = 1/3, \qquad (13)$$

where θ is the angle between the z axis and $\mathbf{H}_{\text{ef}}(t)$, and the averaging is over the angles. Thus, the classical mean-field arguments yield a finite (= 1/3) time-averaged polarization of the first spin. Although the numerical value $\overline{P_1(t)}$ in Eq. (13) coincides with its quantum value given by Eqs. (9)–(11), it is difficult to explain classically, e.g., the recovery of initial polarization after $t = 4\pi/g$, which corresponds to the lowest frequency of the quantum system. This can be done only by using the exact quantum result given by Eqs. (9)–(11) and demonstrating the periodicity (reversibility) of the spin dynamics.

At first glance, the obtained polarization "localization" (nonergodicity) on the first spin [$\overline{P_1(t)} = 1/3$ instead of expected $O(1/N)$] can be qualitatively explained as the manifestation of the reversibility of quantum dynamics. Our preliminary calculations show, however, that the polarization localization $\overline{P_1(t)}$ also occurs in the case where the first spin is subjected to an additional time-dependent random field described by the telegraphic process [14]. In this case, the spin dynamics is irreversible and nonergodic.

The exact solution of the many-particle dynamics of the system with Hamiltonian (1) has become possible due to the simple form of spin–spin interactions. The theory describing spin dynamics of the nuclear-spin systems with dipole–dipole interactions is as yet not sufficiently developed to explain the ergodic diffusional behavior observed by modern NMR methods [15].

We are grateful to D.É. Fel'dman and S.V. Iordanskiĭ for helpful discussions. This work was supported by the Russian Foundation for Basic Research, project no. 01-03-33273.

REFERENCES

1. S. Zhang, B. H. Meier, and R. R. Ernst, Phys. Rev. Lett. **69**, 2149 (1992).
2. L. D. Landau and E. M. Lifshitz, *Course of Theoretical Physics*, Vol. 5: *Statistical Physics* (Nauka, Moscow, 1995; Pergamon, Oxford, 1980).
3. D. N. Zubarev, *Nonequilibrium Statistical Thermodynamics* (Nauka, Moscow, 1974; Consultants Bureau, New York, 1974).
4. F. S. Dzheparov, Zh. Éksp. Teor. Fiz. **116**, 1398 (1999) [JETP **89**, 753 (1999)].
5. R. Brüschweiler and R. R. Ernst, Chem. Phys. Lett. **264**, 393 (1997).
6. J. S. Waugh, Mol. Phys. **95**, 731 (1998).
7. E. B. Fel'dman and S. Lacelle, J. Chem. Phys. **108**, 4709 (1998).
8. C. P. Slichter, *Principles of Magnetic Resonance, with Examples from Solid State Physics* (Harper & Row, New York, 1963; Mir, Moscow, 1967).
9. E. P. Wigner, *Group Theory and Its Application to the Quantum Mechanics of Atomic Spectra* (Academic, New York, 1959; Inostrannaya Literatura, Moscow, 1961).
10. L. D. Landau and E. M. Lifshitz, *Course of Theoretical Physics*, Vol. 3: *Quantum Mechanics: Non-Relativistic Theory* (Nauka, Moscow, 1974; Pergamon, New York, 1977).
11. N. Bloembergen, Physica (Amsterdam) **15**, 386 (1949).
12. E. B. Fel'dman, R. Brüschweiler, and R. R. Ernst, Chem. Phys. Lett. **294**, 297 (1998).
13. E. B. Fel'dman and M. G. Rudavets, Chem. Phys. Lett. **311**, 453 (1999).
14. V. I. Klyatskin, *Stochastic Equations and Waves in Randomly-Inhomogeneous Media* (Nauka, Moscow, 1980).
15. W. Zhang and D. G. Cory, Phys. Rev. Lett. **80**, 1324 (1998).

Translated by V. Sakun

JETP Letters, Vol. 75, No. 12, 2002, pp. 638–641. Translated from Pis'ma v Zhurnal Éksperimental'noĭ i Teoreticheskoĭ Fiziki, Vol. 75, No. 12, 2002, pp. 763–767.

Fine Structure of Ferromagnetic-Resonance Spectra of Disperse Magnets

O. N. Mart'yanov*, R. N. Li, and V. F. Yudanov***

** Boreskov Institute of Catalysis, Siberian Division, Russian Academy of Sciences, pr. Akademika Lavrent'eva 5, Novosibirsk, 630090 Russia*

*** Budker Institute of Nuclear Physics, Siberian Division, Russian Academy of Sciences, pr. Akademika Lavrent'eva 11, Novosibirsk, 630090 Russia*

e-mail: oleg@catalysis.nsk.su

Received May 8, 2002

The technique of ferromagnetic resonance (FMR) was used for the investigation of nickel powders dispersed in a diamagnetic solid matrix. The fine structure of FMR was studied, which was observed against a background of broad featureless FMR lines of conventional unoriented polycrystals. A model is suggested according to which the narrow lines observed appear in the FMR spectra because of jumplike changes in the resonance conditions caused by a sharp change in the magnetization of the sample due to a change in the external magnetic field. In contrast to the Barkhausen effect, the fine structure detected in the FMR spectra in this case is observed in stronger fields characteristic of the processes of magnetization rotation. It is shown that the physical origin of magnetization jumps in this case may be magnetic interparticle interactions as well as complex anisotropy of particles. © *2002 MAIK "Nauka/Interperiodica".*

PACS numbers: 75.50.Tt; 76.50.+g; 75.60.-d

The application of the method of ferromagnetic resonance (FMR), which is very informative in many cases, for studying disperse magnets is restricted by strong line broadening arising because of the chaotic orientation of magnetically anisotropic particles that comprise the solid [1]. As a result, a nonsymmetrical absorption line is usually detected with a width that is caused by the anisotropy of magnetic interactions. New opportunities for obtaining information on the structure of disperse magnets are now emerging, which are based on an analysis of additional very weak and unusually narrow FMR lines.

We studied samples of powder nickel prepared by dispersion in a molten paraffin matrix with subsequent cooling to room temperature. The agglomerates that could be formed when using this procedure were destroyed by ultrasonic treatment of molten suspensions. According to electron-microscopic data, particles with dimensions from 0.2 to 10 μm were present in the samples. The fraction of fine particles increased significantly after the ultrasonic treatment. The FMR spectra were detected using a Bruker-EMX 3-cm radio-frequency spectrometer. The samples were placed in the center of a rectangular resonator of the TE_{102} type (with the magnetic component of the microwave field perpendicular to the direction of the dc magnetic field). The first derivative of the absorption spectrum was written at a modulation frequency of the dc field equal to 100 kHz. The measurements were carried out at room temperature.

Figure 1 displays a Ni powder spectrum with a wide particle-size distribution (from 0.1 to 10 μm). Against the background of the wide spectrum, very weak and narrow lines can be detected (see inset), which are observed in a wide range of fields. Below, we will use the term "fine structure of FMR" (FS FMR) for this feature of the spectrum. To analyze the fine structure, it is convenient to subtract the wide smooth component using the standard function of the MICROCAL ORIGIN program. The procedure of smoothing is as follows: first, the Fourier transform of the spectrum is calculated; then, in accordance with given parameters,

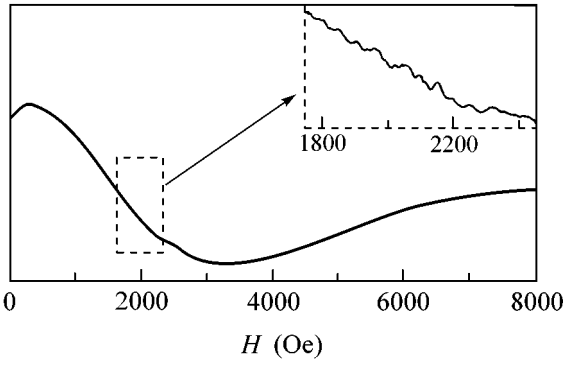

Fig. 1. Spectrum of ferromagnetic resonance of nickel powder in a paraffin matrix. According to electron microscopy, particles with sizes from 0.2 to 10 μm are present. Nickel content is ~5 wt %.

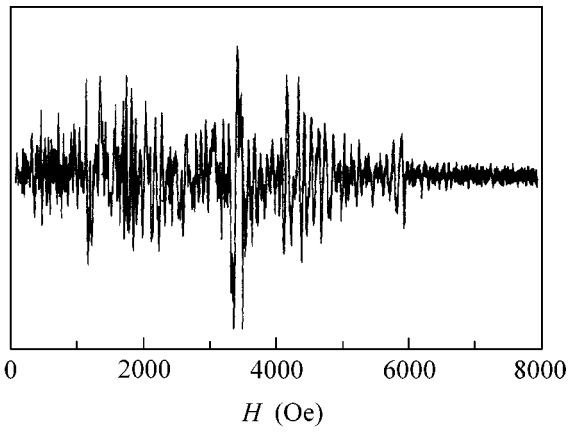

Fig. 2. Fine structure of the spectrum of ferromagnetic resonance of nickel powder in a paraffin matrix. The spectrum was obtained after the procedure of subtracting the broad smooth component. Nickel content in the sample is ~5 wt %.

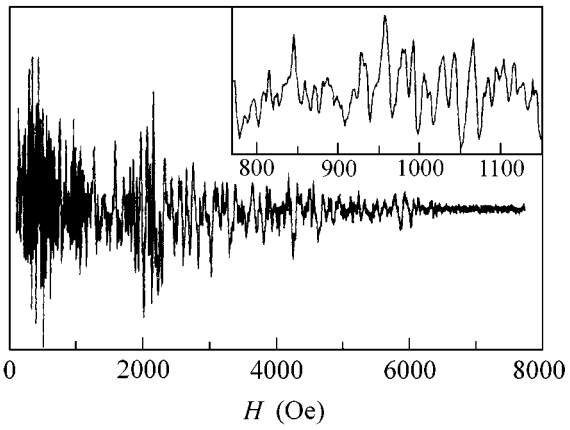

Fig. 3. Fine structure of the spectrum of ferromagnetic resonance of nickel powder prepared using ultrasonic dispersion in a molten paraffin matrix. Nickel content in the sample is ~1 wt %.

higher harmonics are excluded (higher than a certain specified one), and the reverse transformation is performed. The resulting spectrum of the fine structure is calculated as the difference between the experimental and smoothed spectra (Fig. 2). Note that the fine structure of FMR can be registered in the spectra even without the application of some additional mathematical procedures at a sufficiently good signal-to-noise ratio.

The number of lines in the fine structure (Fig. 2) can reach a few hundred, and the range of observation can vary from virtually zero fields to magnetic fields close to those maximally attainable in the EPR spectrometer used. The width of the narrowest lines is a few oersteds (see inset in Fig. 3).

The spectra observed are characterized by a strong orientation dependence, although the envelope of the fine structure of FMR is retained. With a change in the position of the sample in the resonator of the spectrometer, the positions and the shapes of individual lines change in a random manner, but the natural criterion of their physical reality is the strict reproducibility found in independent series of detection.

The fine structures possess properties that are unusual for nonuniformly broadened FMR spectra; namely, they are very sensitive to external actions on the sample such as changes in the gas atmosphere, temperature, light illumination, etc. [2].

The type of the fine structure of FMR is determined to a significant degree by the conditions of the preparation of the disperse samples. It has been established that the variety of fine structures of FMR of ferromagnetic powders arises as a consequence of the different significance of magnetic interparticle interactions. Thus, the disintegration of aggregated particles of nickel powder in a paraffin bath by ultrasonic dispersion at the content of the ferromagnetic phase ~1 wt % leads to a substantial simplification of the fine structure of the spectrum (Fig. 3). The lines of various widths that were present in the fine structure of FMR of the sample before dispersion (Fig. 2) turn out to be grouped in certain ranges of the magnetic field (Fig. 3). In each such range, we can distinguish a certain value of the magnetic field that corresponds to a maximum intensity of the fine-structure lines.

A comparison of the observed spectra with data from the literature shows that the appearance of the fine structure of FMR is related to the processes of magnetization of isolated particles comprising the sample. Kittel *et al.* [3] showed experimentally and theoretically that, to magnetize an isolated spherical particle, its magnetic self field of demagnetizing should be overcome, which is on the order of $H_{cs} \approx 2K_\alpha/J_s$ for single-domain particles and $H_{cm} \approx 4\pi J_s/3$ for multidomain particles (here K_α is the magnetocrystalline anisotropy constant and J_s is the saturation magnetization). In the case of metallic nickel, the corresponding values of magnetic fields are $H_{cs} \sim 550$ Oe for single-domain particles and $H_{cm} \sim 2100$ Oe for multidomain particles.

It is seen that these values correspond well to the maxima of the regions of the observed fine structure of the spectrum. Thus, the range of narrow lines in weak fields corresponds to single-domain particles, whereas the region of wider lines with a maximum in a field of ~2100 Oe corresponds to multidomain particles. For the case of nonspherical particles, deviations from the above values are observed, which are related to the effect of the demagnetizing shape factor. The absorption lines in higher fields can be attributed to the processes of magnetization of the coarsest agglomerated particles that have an irregular shape and a large demagnetizing factor.

Qualitatively, this assumption is confirmed in experiments. As was described above, upon the preparation of the samples of metallic nickel, the powder placed in

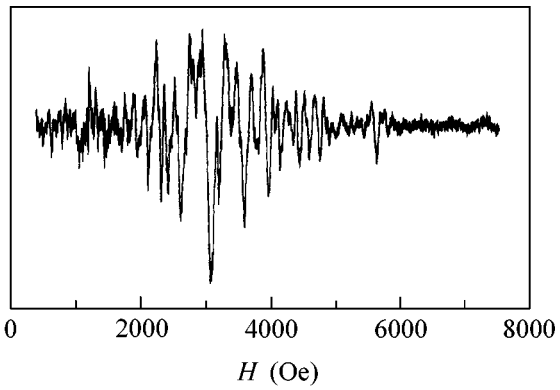

Fig. 4. Fine structure of the spectrum of ferromagnetic resonance of nickel powder prepared by mechanically stirring the powder in a paraffin bath without ultrasonic dispersion. Nickel content in the sample is ~ 1 wt %.

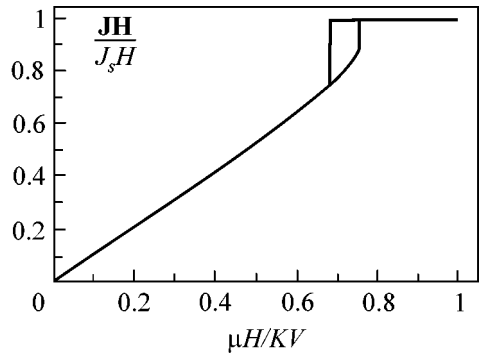

Fig. 5. Variation of the projection of the total magnetic moment of a system of two particles onto the direction of the magnetic field as a function of an external magnetic field. The particles possess magnetic anisotropy and are related by a dipole–dipole interaction. The Hamiltonian of the system and its parameters are given in the main text.

the paraffin matrix is subjected to ultrasonic dispersion, which, according to electron microscopy, leads to an increase in the amount of isolated particles with sizes from several hundred angstroms to a micron. In the sample that was stirred mechanically in the paraffin matrix without ultrasonic dispersion, the number of particles less than a micron in size was substantially smaller. The fine structure of FMR for a sample prepared in this manner is shown in Fig. 4. As is seen, no low-field region with narrow lines is present in the spectrum. This agrees with the absence of a noticeable amount of fine particles in this sample.

Usually, the magnetization processes do not lead to the appearance of new lines of small width in the FMR spectra. It is also known that the FMR line of a single-crystal Ni has a width of at least ~10^2 Oe [4]. Narrow lines are supposed to appear in the FMR spectra because of a jumplike change in the resonance conditions upon the magnetization of ferromagnetic particles. One of the possible mechanisms of such changes is the irreversible rotation of the magnetization vector, which leads to the appearance of hysteresis.

In the classical case of a uniaxial ferromagnetic crystal, the jump in magnetization due to an increase in the magnetic field can occur only once. For such a jump to be repeated, the crystal should be placed in a magnetic field of the opposite direction. However, in the case of a real polycrystal, this condition may not be necessary because of the effects of interparticle interactions or the presence of isolated particles of irregular shape.

To illustrate the possibility of the appearance of hysteresis and related jumps of magnetization in positive magnetic fields, we consider a simple model system consisting of two identical single-domain particles placed in a magnetic field. We assume that both particles exhibit axial anisotropy, which may have either a geometrical (shape anisotropy) or crystallographic (magnetocrystalline anisotropy) origin. With allowance for this anisotropy and the dipole–dipole interaction, the energy of the system is written as follows:

$$E = E_K + E_{\rm dd} + E_H = -\frac{KV}{\mu^2}[(\mu_1\mathbf{n}_1)^2 + (\mu_2\mathbf{n}_2)^2] + \frac{d^2\mu_1\mu_2 - 3(\mathbf{d}\mu_1)(\mathbf{d}\mu_2)}{d^5} - \mathbf{H}(\mu_1 + \mu_2),$$

where K is the effective anisotropy constant, V is the volume of an isolated particle, $\mu_{1,2}$ are the vectors of the magnetic moments of the particles ($\mu = |\mu_1| = |\mu_2|$), $\mathbf{n}_{1,2}$ are the directions of the easy axes of the particles, and $\mathbf{d}$ is the vector characterizing their mutual arrangement. Simulation shows that hysteresis in such a system can arise upon a change in the magnitude of the magnetic field even its changing to the opposite direction. Consider, for example, the case where the vector of the magnetic field $\mathbf{H}$ is oriented along the vector $\mathbf{d}$ the easy axes are parallel to one another ($\mathbf{n}_1 = \mathbf{n}_2 = \mathbf{n}$), and the angle between $\mathbf{n}$ and $\mathbf{H}$ is 82°. With the dipole–dipole interaction defined as $\mu^2/d^3 = KV$, the hysteresis is observed near the field $H = 0.7KV/\mu$ (see Fig. 5). The jump of the magnetization projection onto the direction of the magnetic field is related to the irreversible rotations of the magnetic moments at $H = 0.678KV/\mu$ and $H = 0.748KV/\mu$. Figure 6 displays the rotations of the vectors of magnetic moments upon a decrease in the magnetic field from $H = 5KV/\mu$ to zero. In the field $H = 0.678KV/\mu$, the "collinear" minimum disappears and the system passes into an "anticollinear" state. As the field increases from zero, the "anticollinear" minimum disappears at $H = 0.748KV/\mu$ and the system passes into a collinear state.

Thus, to observe a hysteresis loop, it is sufficient to change the field in the range $H = 0.6$–$0.8(KV/\mu)$ without changing its direction to the opposite. An obvious and important circumstance is that, upon the irreversible rotation of the vectors of the magnetic moments of par-

ticles, there occurs a jumplike change in the resonance conditions of the system. This naturally leads to a change in the absorption of the microwave field, which is detected as the appearance of additional narrow lines in the FMR spectrum.

The above mechanism permits us to explain the experimentally observed strong angular dependence. For example, as the angle between **n** and **H** decreases by 2° (to 80°), the hysteresis loop in Fig. 5 shifts by a distance of an order of its width. In the other regions, the curve changes only slightly.

In the above-described system, such a situation is by no means unique; a hysteresis in positive fields is observed for other system parameters as well. An interesting situation arises when the magnetic field is perpendicular to **d** at the strength of the dipole–dipole interaction $\mu^2/d^3 = 1.5KV$ and the angle between **n** and **H** equals 5°. In this case, as the magnetic field changes from zero, there occur two irreversible rotations of the vectors of the magnetic moments of particles at $H = 1.56KV/\mu$ and $H = 2.03KV/\mu$ and, during the second rotation, the magnetization projection onto the direction of the magnetic field decreases.

It follows from the above analysis that the condition for the appearance of hysteresis is as follows: $\mu H \sim KV \sim \mu^2/d^3$. This explains the appearance of a fine structure of FMR in fields corresponding to the magnetic saturation of single-domain particles ($H_{cs} \sim 550$ Oe) [3].

A consideration of the process of magnetization of an isolated particle shows that the appearance of hysteresis in positive fields is possible even in the absence of interparticle interaction in the presence of magnetocrystalline anisotropy or a complex shape anisotropy of particles.

A well-known example in which the magnetocrystalline anisotropy of a particle leads to the appearance of hysteresis in positive fields is when an isolated particle with a cubic symmetry is placed in an external magnetic field applied along the crystallographic direction [111] [5]. Using numerical simulation, we showed that in this case the hysteresis is observed only if the vector of the applied field falls into a narrow solid angle (of about 1°) centered at this direction. Since the probability that the field will have such a direction is small, this mechanism cannot explain the fine structure of FMR with a large number of lines in a broad range of magnetic fields that is observed in the system under consideration.

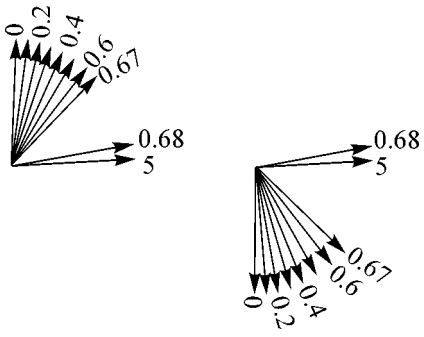

Fig. 6. Rotation of the vectors of magnetization of the particles on changing the magnetic field from $H = 5KV/\mu$ to zero. At $H = 0.678KV/\mu$, the irreversible rotation of the magnetization vectors related to the disappearance of the "collinear" minimum occurs.

At the same time, the existence of complex shape anisotropy of particles can lead to the appearance of hysteresis in positive fields for most randomly oriented noninteracting ferromagnetic particles in a disperse sample.

The appearance of lines of a fine structure of FMR in stronger fields, near magnetic saturation of multidomain particles, also is related to irreversible rotations of magnetic moments, which in this case are determined by changes in the number of domains in multidomain particles.

ACKNOWLEDGMENTS

This work was supported in part by the Russian Foundation for Basic Research (project no. 02-03-33322) and by INTAS (grant for young scientists no. YSF 01/1-14).

REFERENCES

1. E. Schloemann, J. Phys. Chem. Solids **6**, 242 (1958).
2. V. F. Yudanov, O. N. Martyanov, and Yu. N. Molin, Chem. Phys. Lett. **284**, 435 (1998).
3. Ch. Kittel, J. K. Galt, and W. E. Campbell, Phys. Rev. **77**, 725 (1950).
4. D. S. Rodbell, Physics **1**, 179 (1965).
5. N. S. Akulov, *Ferromagnetism* (GITTL, Moscow, 1939).

Translated by S. Gorin

JETP Letters, Vol. 75, No. 12, 2002, pp. 642–645. Translated from Pis'ma v Zhurnal Éksperimental'noĭ i Teoreticheskoĭ Fiziki, Vol. 75, No. 12, 2002, pp. 768–771.

Characteristic Features of the Pseudogap and Superconducting States of $YBa_2Cu_3O_{7-x}$

O. V. Misochko*, N. Georgiev, T. Dekorsy**, and M. Helm****

** Institute of Solid State Physics, Russian Academy of Sciences, Chernogolovka, Moscow region, 142432 Russia*

*** Institute for Ion Beam Physics and Materials Research, Forschungszentrum Rossendorf, P.O. Box 510119, D-01314 Dresden, Germany*

e-mail: misochko@issp.ac.ru

Received May 13, 2002

The relaxation dynamics of the lattice and low-energy quasiparticles in a $YBa_2Cu_3O_{7-x}$ superconductor are studied by the light reflection technique with femtosecond temporal resolution in a wide temperature range. It is shown that, for $T > T_c$, there exist two temperature regions with qualitatively and quantitatively different excitation dynamics, and the transition between these regions is of a hysteretic nature. It is also found that the character of changes observed in the charge carrier relaxation dynamics in the superconducting state testifies to the presence of an anisotropic gap with nodes at the Fermi surface. © *2002 MAIK "Nauka/Interperiodica".*

PACS numbers: 74.25.Kc; 74.72.Bk; 74.76.Bz; 78.47.+p

For the past few years, one of the major problems in high-temperature superconductivity (HTSc) has been the study of the physics of the pseudogap state, which exists in the metallic phase at temperatures $T^* > T_c$ [1, 2]. Today, this problem seems to be among the most topical ones in the physics of high-temperature superconductivity, and its solution will undoubtedly contribute to the elucidation of the microscopic mechanism of HTSc. The width of the pseudogap state region $T^* - T_c$ in the phase diagram depends on the carrier concentration. It is maximal for underdoped compounds and decreases to zero at a certain critical carrier concentration; the latter is somewhat higher than the concentration at which the critical temperature T_c is maximal. Recent theoretical papers suggest an inhomogeneity of the pseudogap phase and the existence of the temperature crossover, which separates the regions of the pseudogap states with different dynamic properties of quasiparticles [3–5]. Progress in laser technology has made it possible to decrease the laser pulse duration down to a few femtoseconds, and this has opened up new research prospects by making studies of quasiparticle dynamics and lattice vibrations accessible in real time. Such studies, whose typical example is the pumping technique with subsequent probing by two laser pulses separated in time, are actively performed on HTSc systems [6–9]. The understanding of the mechanism underlying the establishment of equilibrium after its perturbation by a laser pulse gives an insight into the characteristic features of the dynamics of charge carriers and crystal lattice excitations, as well as the dynamics of their interaction. Using the pump–probe technique, we performed detailed studies of the relaxation dynamics of the lattice and charge carriers in the temperature range covering both superconducting and pseudogap states. The aim of our studies was to determine the degree of homogeneity of the phase diagram region for $T > T_c$ and to reveal the characteristic features of the superconducting state.

The studies of the optical response were performed on an optimally doped (T_c = 88 K) epitaxial film of $YBa_2Cu_3O_{7-x}$ (Y123) grown on a $SrTiO_3$ substrate. The film thickness was 350 nm, and its *c* axis was perpendicular to the substrate plane. The sample was placed in an optical helium cryostat, which allowed the measurements in the temperature range 4–310 K. The measurements in the time domain were done using a fast scan system [6] and sapphire titanate laser pulses (λ = 780 nm) with a duration of less than 50 fs and a repetition frequency of 78 MHz. The polarizations of the exciting and probe pulses were orthogonal to each other and lay in the film plane. In the experiment, the differential reflection from the excited and nonexcited samples, $\Delta R(t) = R(t) - R_0$, was measured as a function of time *t* between pumping and probing in a wide temperature range.

Figure 1 shows a typical optical response obtained from the excitation and subsequent probing of the Y123 film by the femtosecond pulses. The excited electron state relaxes to the equilibrium state within the time of order of picoseconds. The decay of the photoinduced differential reflection has a non-exponential character and may be described by a sum of two, fast and slow, exponentials: $\Delta R/R_0 = A(T)\exp(-t/\tau_A) + B(T)\exp(-t/\tau_B)$. Fast oscillations shown in the inset in Fig. 1 and associated with the coherent phonons [6, 7] are superimposed on this electronic decay. For the identification of the phonon modes, the data obtained in the time domain

were numerically transformed to the frequency domain by using the Fourier transform. This paper studies both the oscillatory component of the optical response caused by the excitation of coherent optical phonons and the nonoscillatory response related to the charge carrier relaxation.

In the superconducting state, two fully symmetric phonon modes generated by the corresponding displacements of the Ba and Cu ions (see Fig. 2) [6, 7] are detected in the spectrum of coherent phonons. An increase in temperature leads to a decrease in the amplitude of the Ba mode. Therefore, the Cu mode dominates in the spectrum in the vicinity of the superconducting transition, which can be easily traced by comparing the amplitudes of the coherent phonons related to Ba and Cu. At helium temperatures, the electron relaxation is governed by the slow component, which demonstrates a weak singularity at T_c. The quantity $\Delta R/R_0$ continues decreasing above T_c; however, at temperatures above $T > T_1^* = 160$ K, the photoinduced response abruptly changes its behavior. The fast component of the electron relaxation exhibits a change of sign and reduces to a spike whose duration does not exceed that of the laser pulse. The slow component also changes sign and considerably slows down. Simultaneously, the spectrum of coherent phonons changes, becoming similar to the spectrum observed in the superconducting state. A further increase in temperature above $T_2^* = 220$ K results in the recovery of the character of the photoinduced response observed in the temperature range T_c–T_1^*. Interestingly, the temperatures T_1^* and T_2^* corresponding to sharp changes in the relaxation dynamics of charge carriers and crystal lattice exhibit a hysteretic character. When approaching the superconducting transition from above, the changes in the photoinduced response are observed at $T_2^* = 175$ K and $T_1^* = 115$ K. The results obtained for the relaxation dynamics of the charge carriers and lattice are summarized in Fig. 3.

The idea of the inhomogeneity of the pseudogap state of HTSc was suggested theoretically and may be explained as a consequence of the local pairing and delocalization of the electron pairs [5]. In addition, the inhomogeneous state may originate from weak and strong regimes of the almost antiferromagnetic Fermi liquid [4] or from the formation of a charge inhomogeneity (stripe fluctuations) with the subsequent appearance of superconductivity in individual stripes [3]. The results obtained do not allow one to give preference to either of the above models. First of all, this is related to the fact that the hysteretic behavior has been predicted by none of the models; it still remains unclear whether different models differ from each other and have any fundamental limitations in this respect. However, certain features of the relaxation dynamics may be explained by each theory. For example, the acceleration

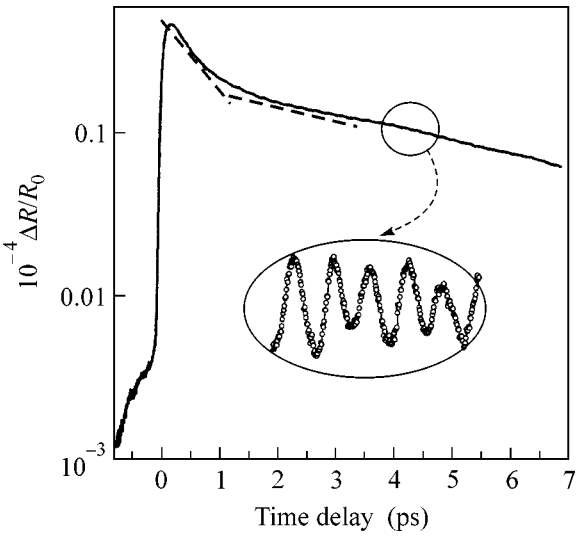

Fig. 1. Time-resolved differential reflection $\Delta R/R_0$ (on a logarithmic scale) for $YBa_2Cu_3O_{7-x}$ at room temperature. The dashed lines show the fast and slow relaxation channels. The inset magnifies the oscillations caused by the coherent phonon excitation.

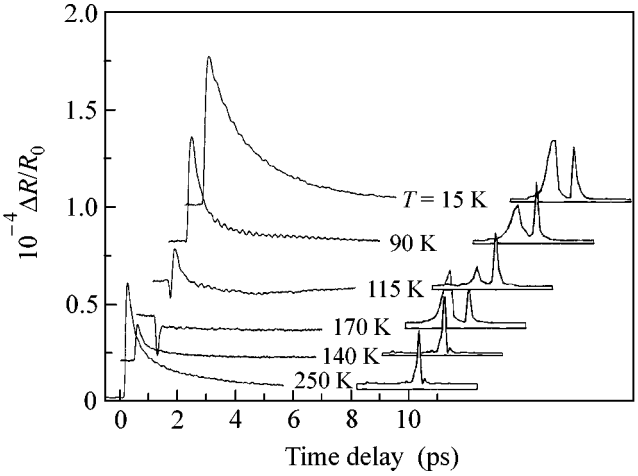

Fig. 2. Temperature dependence of the time-resolved differential reflection $\Delta R/R_0$. The Fourier transforms of the oscillatory parts are shown on the right of each transient curve. The two pronounced peaks at frequencies of 3.5 and 4.5 THz correspond to the fully symmetric A_g phonons generated by the Ba and Cu ion displacements.

of the fast component and deceleration of the slow component within the temperature range T_1^*–T_2^* may be evidence for the appearance of local short-lived electron pairs whose constituents are localized. The disappearance of (decrease in) the slow component at $T < T_1^*$ may be interpreted as the beginning of the electron pair motion over the crystal. The similarity of the coherent

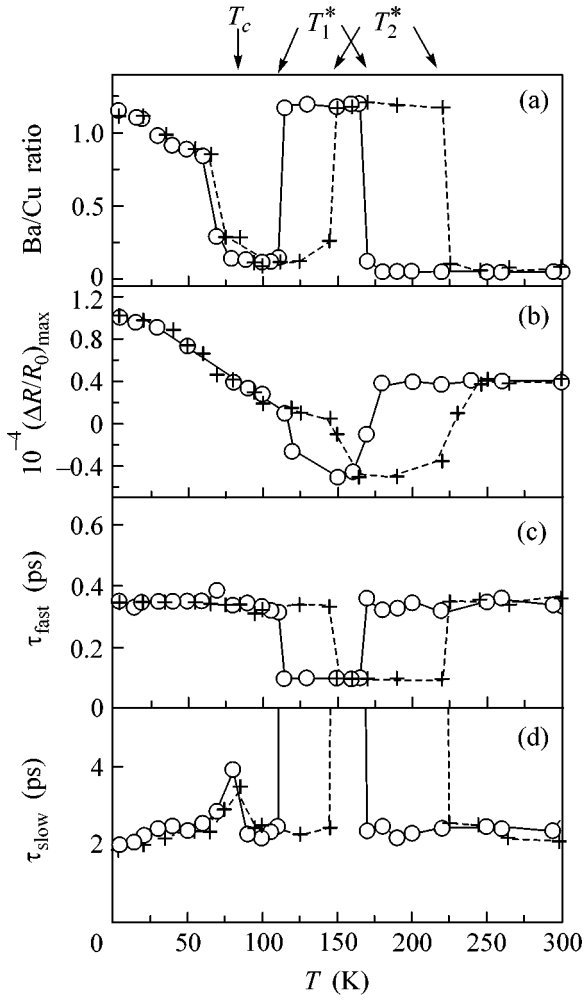

Fig. 3. Parameters of the relaxation dynamics of the excitations and lattice versus the temperature. The circles correspond to the data obtained with decreasing temperature, and the crosses, with increasing temperature. (a) Ratio of the phonon amplitudes of the Ba and Cu modes in the periodogram; (b) extremum of the differential reflection $(\Delta R/R_0)_{max}$; (c) fast relaxation time; and (d) slow relaxation time.

phonon spectra for the temperature ranges T_1^*–T_2^* and $T < T_c$ also supports the hypothesis of the formation of local electron pairs, because the increase in the Ba phonon amplitude is usually attributed to the breaking of Cooper pairs [6, 7]. However, in the range T_1^*–T_c, where, according to the theory in [5], the pairs are itinerant, the spectrum of coherent phonons exhibits a similarity to the spectrum observed at temperatures above the second crossover T_2^*. It remains unclear why the delocalized but still incoherent pairs cease interacting with the lattice, whereas the localized pairs and Cooper pairs, which constitute the superconducting condensate, demonstrate this kind of interaction. Nevertheless, the similarity of the coherent dynamics of the lattice in the pseudo-gap and superconducting states enables one to assume that the electron–phonon interaction is needed to explain the experimental data. As an alternative explanation, the upper crossover could be assigned to the beginning of the weak regime of the pseudogap state, when the hot spots start appearing at the Fermi surface. The lower crossover then could be attributed to the appearance of the strong regime, in which the Fermi surface starts loosing its parts in some regions of the momentum space [4]. However, the changes in the coherent phonon spectrum can hardly be explained in terms of a nearly antiferromagnetic Fermi liquid.

In contrast to the pseudogap state, the superconducting state exhibits no hysteresis, and the characteristics of the relaxation dynamics coincide within the experimental error for both increasing and decreasing temperature. This result is quite natural, because the superconducting transition in the absence of a magnetic field is of second order, whereas the hysteresis is characteristic of the first-order transitions only. However, it should be noted that the ratio between the slow (*B*) and fast (*A*) components in the superconducting state is temperature-dependent (it increases as *T* decreases). The fact that the slow component predominates in the superconducting state is determined by the appearance of the gap in the spectrum of excitations. Breaking the Cooper pairs with a laser pulse leads to the appearance of quasiparticles whose relaxation is determined by the relaxation of the superconducting gap to the equilibrium state. If we attribute the fast dynamics to the carriers in the cold spots, which are located at the diagonals of the Brillouin zone, and the slow dynamics, to the carriers in the vicinity of the hot spots, which are located at the zone faces where the superconducting gap takes its maximal values, we should expect that the superconducting gap continues demolishing the Fermi surface in the superconducting state as well. Such an association of the two different dynamic times with the location of quasiparticles in the Brillouin zone is supported by the following experimental fact [10]: it was found that the dependence of the slow component on the pump power exhibits a saturation, whereas no saturation is observed for the fast component, whose amplitude grows linearly with the power of the exciting pulses. This fact enables us to attribute the slow component to the breaking of Cooper pairs, whose density is finite in the condensate, and to assign the fast component to the quasiparticles in the vicinity of the nodes of the superconducting gap. The variation of the ratio *B*/*A* in the superconducting state testifies to (1) the existence of nodes of the superconducting gap, because the fast component is finite at the lowest temperatures, and (2) the dependence of the anisotropy of the gap on temperature, which dramatically disagrees with the predictions of the Bardeen–Cooper–Schrieffer theory, in which the anisotropy of the gap is found to be temperature-independent as a result of the factorization of the wave vector and temperature in the equation for the superconducting gap [11]. The conclusion that an anisotropic superconducting gap with nodes at the Fermi surface exists agrees

well with the experimental results obtained by other optical techniques [11], although it differs from the data on the gap obtained from earlier time-resolved measurements [8].

Thus, by using the pumping–probing technique with femtosecond resolution, we observed two temperature crossovers in the normal state of an optimally doped Y123 high-temperature superconductor. The crossovers manifest themselves as sharp changes in the relaxation dynamics of the charge carriers and the lattice and exhibit a hysteresis in temperature. The existence of such crossovers testifies to the inhomogeneity of the pseudogap state. In addition, we have found that, in the superconducting state, the energy gap has nodes and its anisotropy depends on temperature.

This work was supported by the Russian Foundation for Basic Research, project no. 01-02-1640.

REFERENCES

1. T. Timusk and B. Statt, Rep. Prog. Phys. **62**, 61 (1999).
2. M. V. Sadovskiĭ, Usp. Fiz. Nauk **171**, 539 (2001).
3. V. J. Emery, S. A. Kivelson, and O. Zachar, Phys. Rev. B **56**, 6120 (1997).
4. J. Schmalian, D. Pines, and B. Stojkovic, Phys. Rev. B **60**, 667 (1999).
5. P. Devillard and J. Ranninger, Phys. Rev. Lett. **84**, 5200 (2000).
6. W. Albrecht, Th. Kruze, and H. Kurz, Phys. Rev. Lett. **69**, 1451 (1992).
7. O. V. Misochko, K. Kisoda, K. Sakai, and S. Nakashima, Phys. Rev. B **61**, 4305 (2000).
8. C. J. Stevens, D. Smith, C. Chen, *et al.*, Phys. Rev. Lett. **78**, 2212 (1997).
9. J. Demsar, B. Podobnik, V. V. Kabanov, *et al.*, Phys. Rev. Lett. **82**, 4918 (1999).
10. R. A. Kaindl, M. Woerner, T. Elsaesser, *et al.*, Science **287**, 470 (2000); R. A. Kaindl, Ph.D. Dissertation (Humboldt University, Berlin, 2000).
11. E. Ya. Sherman, O. V. Misochko, and P. Lemmens, in *Spectroscopy of High-T_c Superconductors*, Ed. by N. M. Plakida (Taylor & Francis, London, 2002), p. 97.

Translated by E. Golyamina

JETP Letters, Vol. 75, No. 12, 2002, pp. 646–650. From Pis'ma v Zhurnal Éksperimental'noĭ i Teoreticheskoĭ Fiziki, Vol. 75, No. 12, 2002, pp. 772–776.

Josephson Effect in S_FXS_F Junctions[1]

N. M. Chtchelkatchev, W. Belzig*, and C. Bruder*

Landau Institute for Theoretical Physics, Russian Academy of Sciences, ul. Kosygina 2, Moscow 117940, Russia
e-mail: nms@landau.ac.ru

** Departement Physik und Astronomie, Klingelbergstr. 82, Universität Basel, 4056 Basel, Switzerland*

Received May 16, 2002

We investigate the Josephson effect in S_FXS_F junctions, where S_F is a superconducting material with a ferromagnetic exchange field, and X is a weak link. The critical current I_c increases with the (antiparallel) exchange fields, if the distribution of transmission eigenvalues of the X layer has its maximum weight at small values. This exchange-field enhancement of the supercurrent does not exist if X is a diffusive normal metal. At low temperatures, there is a correspondence between the critical current in an S_FIS_F junction with collinear orientations of the two exchange fields, and the AC supercurrent amplitude in an SIS tunnel junction. The difference in the exchange fields $h_1 - h_2$ in an S_FIS_F junction corresponds to the potential difference $V_1 - V_2$ in an SIS junction; i.e., the singularity in I_c [in an S_FIS_F junction] at $|h_1 - h_2| = \Delta_1 + \Delta_2$ is the analogue of the Riedel peak. We also discuss the AC Josephson effect in S_FIS_F junctions. © *2002 MAIK "Nauka/Interperiodica".*

PACS numbers: 74.50.+r; 74.80.-g; 75.70.-i

The presence of a magnetic exchange field in bulk superconductors [1, 2] and in superconductor (S)–ferromagnet (F) multilayers reduces the critical temperature T_c, i.e., suppresses superconductivity (see, e.g., [3] and references therein). Similarly, an exchange field suppresses the proximity effect: superconducting correlations spread into the F layer of superconductor–ferromagnet structures for a shorter distance than into the normal layer of a superconductor–normal metal structure [4]. Hence, it is natural to expect that the supercurrent in a junction will be suppressed by an exchange field in the superconductors or by the presence of ferromagnetic layers between the superconducting banks. Surprisingly, it was shown recently that the supercurrent can be strongly enhanced in a number of situations, e.g., in an S_FIS_F junction formed by two "ferromagnetic superconductors" (S_F), whose exchange fields are oriented in an antiparallel way [5, 6], and in SFIFS junctions [7, 8]. There is still no simple intuitive understanding of this exchange-field supercurrent-enhancement (EFSE) effect, nor of what conditions favor this effect. In what follows, we investigate the Josephson effect in S_FXS_F junctions for different choices of the scattering layer X, for example, when X is a diffusive normal metal or an insulator, and find the conditions favoring the EFSE effect.

In this letter, we show that the EFSE effect exists in S_FXS_F junctions if the distribution of transmission eigenvalues of the X layer has its maximum weight for small values. If the transparency increases, we find that the effect becomes less pronounced; it disappears when the transparency is close to unity. If X is a diffusive normal metal, there is no exchange field enhancement of the supercurrent. At zero temperature, we find a correspondence between the critical current $I_c(V = 0, h_1 - h_2)$ of an $S_{F1}IS_{F2}$ junction with collinear exchange fields $h_{1(2)}$ and the AC supercurrent amplitude $\mathrm{Re}\,I_c(V)$ of an SIS tunnel junction. Both quantities coincide if the voltage V across the junction is equal to $h_1 - h_2$. Thus, the peak singularity of $I_c(V = 0, h_1 - h_2)$ at $|h_1 - h_2| = \Delta_1 + \Delta_2$ has the same nature as the Riedel peak in SIS contacts at $|eV| = \Delta_1 + \Delta_2$ [9–12]. Here, $\Delta_{1(2)}$ are the superconducting pair potentials of the two contacts.

To derive the results listed above, we relate the supercurrent through the S_FXS_F junction to the scattering matrix of the region X, and then use statistical properties of this scattering matrix. The model considered is illustrated in Fig. 1. It consists of a scattering region (hatched) between two superconducting S_F layers.

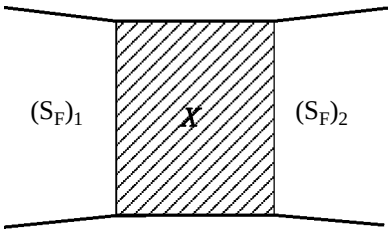

Fig. 1. Sketch of the device showing the EFSE effect; two ferromagnetic superconductor layers S_F are characterized by BCS order parameters $\Delta_{1(2)}$ and exchange fields $\mathbf{h}_{1(2)}$. The scattering region X (e.g., an insulator or a diffusive normal metal) separates the two S_F layers.

[1] This article was submitted by the authors in English.

Examples of S_F layers include superconductors with ferromagnetic impurities [1] or superconductor–ferromagnet (normal metal) multilayers, where the superconducting (and ferromagnetic) order parameter is induced by the proximity effect [5, 13]. They can be described by adding an exchange field to the BCS model [14, 15]. Then the self-consistency equation at zero temperature shows that the superconducting order parameter $\Delta(h) = \Delta(0)$, if the exchange field $h < \Delta(0)$, and $\Delta(h) = 0$ otherwise. In this paper, we assume that $|h| \le \Delta(0)$ in the two "ferromagnetic superconductor" leads.

The supercurrent is calculated using the quasiclassical Green's function technique. We assume that the junction is short, i.e., that the traversal time τ through the region X is such that $\hbar/\tau$ exceeds the superconducting order parameters $\Delta_{1,2}$ of the S_F layers. Then, following [16, 17], we relate the supercurrent I to the Keldysh Green's functions, and, finally, to the retarded quasiclassical Green's functions $\hat{R}_{1,2}$ in the bulk of the S_F layers and the eigenvalues $\mathcal{T}_n$ of $tt^\dagger$, where t is the matrix transmission amplitude of the X layer:

$$I = \frac{1}{4e}\int de \mathrm{Tr}[\hat{\tau}^{(3)}\hat{I}(E)]\tanh\left(\frac{E}{2T}\right), \tag{1a}$$

$$\hat{I} = \frac{e^2}{\pi\hbar}\sum_n 2\mathcal{T}_n \frac{[\hat{R}_1, \hat{R}_2]}{4 + \mathcal{T}_n(\{\hat{R}_1, \hat{R}_2\} - 2)}, \tag{1b}$$

$$\hat{R}_{1,2}(E) = \frac{i}{\sqrt{(\Delta_{1,2})^2 - (E + \boldsymbol{\sigma}\cdot\mathbf{h}_{1,2})^2}} \times \begin{pmatrix} E + \boldsymbol{\sigma}\cdot\mathbf{h}_{1,2} & e^{i\varphi_{1,2}}\Delta_{1,2} \\ -e^{-i\varphi_{1,2}}\Delta_{1,2} & -E - \boldsymbol{\sigma}\cdot\mathbf{h}_{1,2} \end{pmatrix}. \tag{1c}$$

Here, $\hat{\tau}^{(3)}$ is the Pauli matrix acting in Nambu space, the trace is taken over the Nambu and spin spaces, and $\varphi_{1,2}$ is the superconducting phase corresponding to the S_F layers. Equations (1a)–(1c) are valid for both ballistic and dirty S_F layers.

To derive Eqs. (1a) and (1b), we used the general Zaitsev boundary conditions [16, 17] for the Green's functions rather than the Kupriyanov–Lukichev dirty-limit approximation [18], which is valid for small $\mathcal{T}$ (see, e.g., [19] and references therein). Using the Zaitsev boundary condition leads to the anticommutator of the Green's functions in the denominator of Eq. (1b), which plays an important role here and cannot be neglected. Due to this anticommutator, the EFSE effect is suppressed in S_FIS_F junctions with large transparencies $\mathcal{T}$ and in S_FXS_F junctions, in which X is a dirty normal metal (see, e.g., Fig. 3).

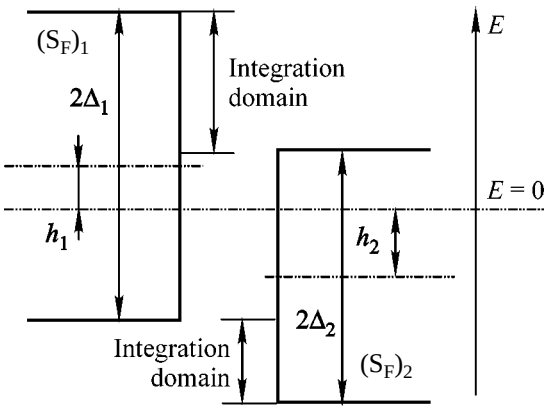

Fig. 2. The integration domain shown gives the main contribution to the supercurrent in an $(S_F)_1I(S_F)_2$ junction according to Eq. (7). The supercurrent shows a Riedel singularity when $|h_1| \longrightarrow \Delta_1$, $|h_2| \longrightarrow \Delta_2$.

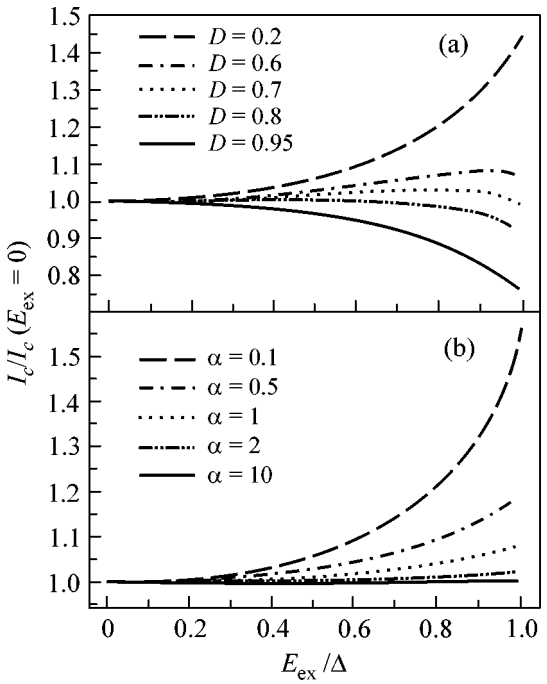

Fig. 3. Exchange-field dependence of the critical current in an S_FXS_F junction with $\Delta_1 = \Delta_2$ and $E_{ex} = h_1 = -h_2$. (a) X is an insulator with transparency D. For $D \ge 0.7$, the supercurrent-enhancement effect disappears. (b) X is a disordered normal metal with conductance G_N and the tunnel junction has conductance G_T; $\alpha = G_T/G_N$. The supercurrent-enhancement effect disappears for $\alpha \gg 1$.

If $\mathbf{h}_1 \parallel \mathbf{h}_2$, Eq. (1b) reduces to:

$$I(\varphi) = \sum_{\sigma = \pm 1}\int d\mathcal{T}\,\rho(\mathcal{T})\frac{e}{\hbar}T\sum_\omega \frac{d}{d\varphi}\ln[g(i\omega, \varphi, \sigma, \mathcal{T})]. \tag{2}$$

Here,

$$g(E, \varphi, \sigma, \mathcal{T}) = (1 - \mathcal{T})\sin(a_1)\sin(a_2) + \frac{1}{2}\mathcal{T}(\cos(\varphi) - \cos(a_1 + a_2)), \quad (3)$$

where $\varphi = \varphi_1 - \varphi_2$, $\rho(\mathcal{T}) = \sum_n \delta(\mathcal{T} - \mathcal{T}_n)$ is the distribution of transmission eigenvalues, $\omega = 2\pi T(k + 1/2)$, $k = 0, \pm 1, \ldots$ are Matsubara frequencies, and $a_{1,2} = \arccos[(E + \sigma h_{1,2})/\Delta_{1,2}]$ represent the phases picked up at an Andreev reflection from the S_F layers. Equations (2) and (3) can be also derived using the scattering theory developed in [20].

In the general case $\mathbf{h}_1 \nparallel \mathbf{h}_2$, the supercurrent is given by

$$I(\varphi) = I^{(p)}(\varphi)\cos^2\left(\frac{\theta}{2}\right) + I^{(a)}(\varphi)\sin^2\left(\frac{\theta}{2}\right), \quad (4)$$

where the indices *p*, *a* correspond to the parallel and antiparallel configurations of the exchange fields and θ is the angle between $\mathbf{h}_1$ and $\mathbf{h}_2$. Equation (4) can be derived from Eqs. (1a)–(1c) using the following identity for an analytic function *L* of two variables:

$$\mathrm{Tr}L[(\boldsymbol{\sigma}\cdot\mathbf{a}), (\boldsymbol{\sigma}\cdot\mathbf{b})] \equiv \frac{1}{2}\sum_{\sigma_{1(2)} = \pm 1}\left(1 + \sigma_1\sigma_2\frac{\mathbf{a}\cdot\mathbf{b}}{|\mathbf{a}||\mathbf{b}|}\right)L[\sigma_1|\mathbf{a}|, \sigma_2|\mathbf{b}|], \quad (5)$$

where the trace is taken over the spin degrees of freedom. The last identity can be proved by a series expansion.

Using Eqs. (2)–(4), we can work out the effect of ferromagnetic interactions on the supercurrent in a number of structures.

We will concentrate below on the case where the exchange fields are collinear. Suppose that X is a tunnel barrier. Then $\rho(\mathcal{T}) = N\delta(\mathcal{T} - D)$, where $D \ll 1$, *N* is the number of channels [$N = k_F^2 A/4\pi$, where *A* is the area of the junction cross section, and k_F is the Fermi wavevector in S]. It follows from Eq. (2) that

$$I(\varphi) = \sin(\varphi)\frac{\pi}{e}(R_N)^{-1}\Delta_1\Delta_2 \times T\sum_\omega \mathrm{Re}\frac{1}{\sqrt{(\Delta_1)^2 + (\omega + ih_1)^2}\sqrt{(\Delta_2)^2 + (\omega + ih_2)^2}}, \quad (6)$$

where $R_N = (NDe^2/\pi\hbar)^{-1}$ is the normal-state resistance of the junction. If $\mathrm{sgn}(h_1h_2) > 0$, Eq. (6) gives $I^{(p)}$, and, in the opposite case, $I^{(a)}$ [see Eq. (4)]. For $\Delta_1 = \Delta_2$, $h_1 = -h_2$, Eq. (6) reproduces the corresponding results of [5].

It follows from Eq. (6) that, at small temperatures, $T \ll \min\{\Delta_1, \Delta_2\}$, as long as $|h_1| < \Delta_1$, $|h_2| < \Delta_2$, the supercurrent does not depend on $h_1 + h_2$. It grows with $h_1 - h_2$ and diverges logarithmically when $|h_1 - h_2| \longrightarrow \Delta_1 + \Delta_2$. To illustrate this, we write Eq. (6) in the real-time representation:

$$I(\varphi) = \frac{\Delta_1\Delta_2}{4R_N}\sin(\varphi)\sum_{\sigma = \pm 1}\int_{-\infty}^{\infty} dE \tanh\left(\frac{E}{2T}\right) \times \mathrm{Im}\frac{1}{\sqrt{((\Delta_1)^2 - (E + h_1\sigma)^2)((\Delta_2)^2 - (E + h_2\sigma)^2)}}. \quad (7)$$

The integration domain is shown in Fig. 2. Equation (7) and Fig. 2 show that the exchange fields $h_{1(2)}$ shift the Fermi energies of the two superconductors by $\sigma h_{1(2)}$. The potentials $V_{1(2)}$ applied to the superconducting banks of an SIS junction shift the Fermi energies in a similar manner. In particular, it turns out that the amplitude $\mathrm{Re}I_c(V)$ of the AC Josephson supercurrent [which is proportional to $\sin(2eVt/\hbar)$] of an SIS junction is equal to the critical current $I_c = I(\varphi = \pi/2)$ in Eqs. (6) and (7) after the substitution $h_{1(2)} \longrightarrow eV_{1(2)}$. At zero temperature, the critical current $I_c = I(\varphi = \pi/2)$ defined by Eq. (7) can be expressed through the elliptic function **K** [10, 11, 21]. If we define $h \equiv h_1 - h_2$, then, within the interval $|h| < |\Delta_1 - \Delta_2|$,

$$I_cR_N = \frac{2e\Delta_1\Delta_2}{\sqrt{(\Delta_1 + \Delta_2)^2 - h^2}} \times \mathbf{K}\left(\sqrt{\frac{(\Delta_1 - \Delta_2)^2 - h^2}{(\Delta_1 + \Delta_2)^2 - h^2}}\right). \quad (8)$$

If $|\Delta_1 - \Delta_2| < |h| < \Delta_1 + \Delta_2$, then

$$I_cR_N = e\sqrt{\Delta_1\Delta_2}\mathbf{K}\left(\sqrt{\frac{4\Delta_1\Delta_2}{h^2 - (\Delta_1 - \Delta_2)^2}}\right). \quad (9)$$

For $h_1 = h_2 = 0$, $\Delta_1 = \Delta_2$, Eq. (9) leads to $I_cR_N = e\Delta\pi/2$, i.e., to the usual result of the critical current of an SIS Josephson junction [12].

For $|h|$ close to $\Delta_1 + \Delta_2$, integral (7) has a singularity. The singular part of the current is

$$I_cR_N \sim \frac{e\sqrt{\Delta_1\Delta_2}}{2}\ln\left(\frac{\Delta_1 + \Delta_2}{||h| - (\Delta_1 + \Delta_2)|}\right). \quad (10)$$

If the temperature is close to the critical temperature of the S_F layer, the supercurrent depends on $h_1 + h_2$, as well as on $h_1 - h_2$, and there is no EFSE effect, in agreement with [5]. In this case, the correspondence of the exchange field in S_FXS_F junctions and the voltage in SIS junctions is no longer valid.

The main point of the above discussion is that the supercurrent is strongly enhanced by the exchange field in the tunneling regime, i.e., when the scattering region X is an insulator with small transparency. Below, we investigate whether the enhancement effect is seen in

other types of S_FXS_F junctions, e.g., when the layer X is a diffusive normal metal.

If $\Delta = \Delta_1 = \Delta_2$, $h \equiv h_1 = -h_2$ (antiparallel magnetizations), Eq. (3) can be simplified:

$$g(E, \varphi, \sigma, \mathcal{T}) = \frac{2-\mathcal{T}}{2\Delta^2}\sqrt{(\Delta^2 - E^2 - h^2)^2 - 4E^2h^2} + \frac{\mathcal{T}}{2}\left(\cos(\varphi) + \frac{h^2 - E^2}{\Delta^2}\right). \quad (11)$$

The current can be evaluated using Eq. (2).

Let us first turn to the case when the distribution of transmission eigenvalues $\rho \propto \delta(\mathcal{T} - D)$. As shown above, the enhancement effect exists as long as $D \ll 1$. If the transparency D becomes larger, we find from Eq. (2) that the EFSE effect becomes less pronounced; it disappears when the transparency is close to unity. This is illustrated in Fig. 3a, where the critical current of an S_FXS_F junction with $\Delta \equiv |\Delta_1| = |\Delta_2|$ is shown as a function of the exchange field $E_{ex} \equiv h_1 = -h_2$ at different transparencies D. The relation between the transparency and the normal-state resistance is given by $D = R_{Sh}/R_N$, where the Sharvin resistance $R_{Sh} = (e^2k_F^2A/4\pi^2\hbar)^{-1}$, and A is the area of the junction.

Another possibility is that X is a dirty normal wire of conductance G_N, and an insulating layer with conductance G_T crosses the wire [this insulating layer, for example, can be situated at the S_F–X interface]. In this case, the distribution of the transmission eigenvalues $\rho(\mathcal{T})$ is known [22]; for example, if $G_T/G_N \gg 1$, then $\rho(\mathcal{T}) = (\pi\hbar G_N/e^2)/\mathcal{T}\sqrt{1-\mathcal{T}}$ [23]. The graph of the critical current versus the exchange field is shown in Fig. 3b for a set of values of $\alpha \equiv G_T/G_N$. It follows from this figure that, in the metallic regime $\alpha \gg 1$, when both small and large transmission eigenvalues give the main contribution to the current, EFSE is suppressed. If X consists of two insulating barriers separated by a dirty normal wire, $\rho \propto 1/\mathcal{T}^{3/2}\sqrt{1-\mathcal{T}}$, there is a weak EFSE effect, and the relative supercurrent enhancement does not exceed 10%.

Figure 4 shows the relative contribution of the discrete spectrum (Andreev levels) and the continuous spectrum to the supercurrent. It turns out that the EFSE effect is mostly due to the continuous spectrum; the contribution of the discrete spectrum to the supercurrent decreases with the exchange field, while the contribution of the continuous spectrum increases. If X is an insulator, the continuous spectrum gives the main contribution to the supercurrent (see Fig. 2), and there is a pronounced EFSE effect.

Finally, we discuss the AC Josephson effect in S_FIS_F structures. Similar to tunnel SIS junctions [10–12], the current consists of three parts: $I(t) = I_1(t) + I_2(t) + I_3$, where $I_1(t) = \mathrm{Re}[I_c(V, h)]\sin(2eVt/\hbar)$ is the supercurrent,

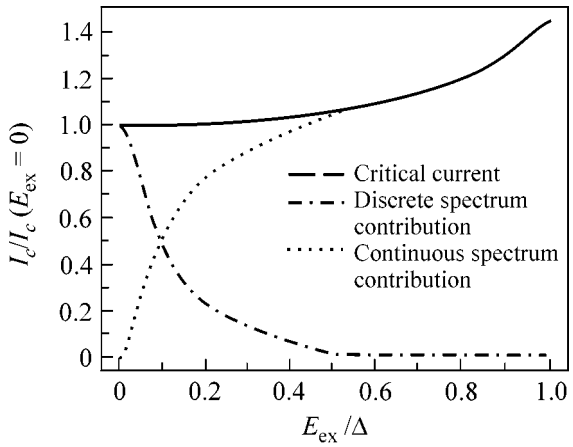

Fig. 4. The critical current in an S_FXS_F junction with $\Delta_1 = \Delta_2$, $E_{ex} \equiv h_1 = -h_2$, $\rho(\mathcal{T}) \propto \delta(\mathcal{T} - D)$, and $D = 0.2$. The figure shows the relative contributions to the critical current from the discrete spectrum (Andreev levels) and the continuous spectrum.

$I_2(t) = \mathrm{Im}[I_c(V, h)]\cos(2eVt/\hbar)$ the interference current, and I_3 the quasiparticle current; here, $h = h_1 - h_2$. We concentrate on the behavior of I_1 and I_2; the quasiparticle current was studied in [13]. The complex supercurrent amplitude $I_c(V, h)$ in an S_FIS_F junction can be calculated in a way similar to an SIS junction [10, 11]. At zero temperature, it has the remarkable property that

$$I_c(V, h) = \frac{1}{2}(I_c(V + h/e, 0) + I_c(V - h/e, 0)). \quad (12)$$

By setting $V = 0$, we find again that the DC critical current of an S_FIS_F junction coincides with the real part of the AC supercurrent amplitude of an SIS junction if we replace eV by h. Using Eq. (12), we can also discuss the AC Josephson effect of the S_FIS_F junction. In an SIS junction, $\mathrm{Re}I_c(V)$ has a Riedel singularity at $|eV| = \Delta_1 + \Delta_2$; but in the S_FIS_F case, the Riedel singularity appears at $|eV \pm (h_2 - h_1)| = \Delta_1 + \Delta_2$ (we assume a collinear orientation of the exchange fields $h_{1,2}$). In an SIS junction, $\mathrm{Im}I_c(V)$ vanishes for $|eV| < \Delta_1 + \Delta_2$ and jumps to $\pi\sqrt{\Delta_1\Delta_2}/2R_N$ at $|eV| = \Delta_1 + \Delta_2$ [12]. In contrast, in an S_FIS_F junction, $\mathrm{Im}I_c(V)$ jumps at $|eV \pm (h_2 - h_1)| = \Delta_1 + \Delta_2$ [see Fig. 5], and the jump is half as large as in the SIS case.

In conclusion, we have shown that there is a pronounced exchange-field supercurrent-enhancement effect in S_FXS_F junctions if the distribution of transmission eigenvalues of the X layer has maximum weight at small values. If X is a diffusive normal metal, there is no exchange-field enhancement of the supercurrent. At small temperatures, there is a correspondence between the critical current in an S_FIS_F junction with collinear orientations of the exchange fields and the supercurrent amplitude in an SIS tunnel junction in the AC regime;

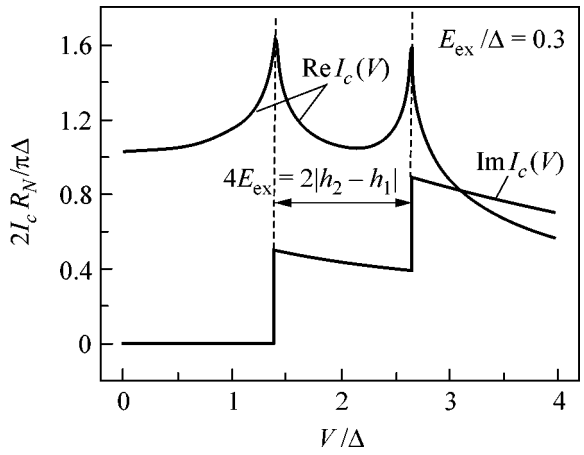

Fig. 5. Real and imaginary parts of the AC Josephson supercurrent amplitude $I_c(V)$ in an S_FIS_F junction at $T = 0$, $E_{ex} \equiv h_1 = -h_2 = 0.3\Delta$, and $\Delta_1 = \Delta_2 \equiv \Delta$. Riedel-type singularities are seen at $V = 2\Delta \pm 2E_{ex}$.

the difference in the exchange fields in an S_FIS_F junction is the analogue of the voltage in an SIS junction. Finally, we have also discussed the AC Josephson effect in S_FIS_F junctions.

We are grateful to V.V. Ryazanov, Ya. Fominov, A.A. Golubov, A. Iosselevich, M.V. Feigelman, and M. Skvortzov for stimulating discussions and useful comments on the manuscript. The work of N.M.C. was supported by the Russian Foundation for Basic Research (project nos. 00-02-16617, 02-02-16622, and 02-02-06509), the Forschungszentrum Jülich (Landau Scholarship), the Netherlands Organization for Scientific Research (NWO), the Swiss NSF, and the Russian Ministry of Science (project *Mesoscopic systems*). W.B. and C.B. thank the Lorentz Center in Leiden, where this manuscript was finished, and the Swiss NSF and the NCCR Nanoscience for financial support.

REFERENCES

1. G. Sarma, J. Phys. Chem. Solids **24**, 1029 (1963); D. Saint-James, G. Sarma, and E. J. Thomas, *Type II Superconductivity* (Pergamon, Oxford, 1969), p. 159.
2. A. I. Buzdin, L. N. Bulaevskiĭ, M. L. Kulic, *et al.*, Usp. Fiz. Nauk **144**, 597 (1984) [Sov. Phys. Usp. **27**, 927 (1984)].
3. Ya. V. Fominov, N. M. Chtchelkatchev, and A. A. Golubov, Pis'ma Zh. Éksp. Teor. Fiz. **74**, 101 (2001) [JETP Lett. **74**, 96 (2001)].
4. E. A. Demler, G. B. Arnold, and M. R. Beasley, Phys. Rev. B **55**, 15174 (1997).
5. F. S. Bergeret, A. F. Volkov, and K. B. Efetov, Phys. Rev. Lett. **86**, 3140 (2001).
6. V. N. Krivoruchko and E. A. Koshina, cond-mat/0104251.
7. N. M. Chtchelkatchev, W. Belzig, Yu. V. Nazarov, and C. Bruder, Pis'ma Zh. Éksp. Teor. Fiz. **74**, 357 (2001) [JETP Lett. **74**, 323 (2001)].
8. A. A. Golubov, M. Yu. Kupriyanov, and Ya. V. Fominov, Pis'ma Zh. Éksp. Teor. Fiz. **75**, 223 (2002) [JETP Lett. **75**, 190 (2002)].
9. E. Riedel, Z. Naturforsch. A **19**, 1634 (1964).
10. N. R. Werthamer, Phys. Rev. **147**, 255 (1966).
11. A. I. Larkin and Yu. N. Ovchinnikov, Zh. Éksp. Teor. Fiz. **51**, 1535 (1967) [Sov. Phys. JETP **24**, 1035 (1967)].
12. I. O. Kulik and I. K. Yanson, *The Josephson Effect in Superconductive Tunneling Structures* (Nauka, Moscow, 1970; Israel Program for Scientific Translations, Jerusalem, 1972).
13. D. H. Huertas-Hernando, Yu. V. Nazarov, and W. Belzig, Phys. Rev. Lett. **88**, 047003 (2002).
14. A. A. Abrikosov, *Fundamentals of the Theory of Metals* (Nauka, Moscow, 1987; North-Holland, Amsterdam, 1988).
15. Ya. V. Fominov, N. M. Chtchelkatchev, and A. A. Golubov, cond-mat/0202280.
16. A. V. Zaitsev, Zh. Éksp. Teor. Fiz. **86**, 1742 (1984) [Sov. Phys. JETP **59**, 1015 (1984)].
17. Yu. V. Nazarov, Superlattices Microstruct. **25**, 1221 (1999).
18. M. Yu. Kupriyanov and V. F. Lukichev, Zh. Éksp. Teor. Fiz. **94**, 139 (1988) [Sov. Phys. JETP **67**, 1163 (1988)].
19. W. Belzig, F. K. Wilhelm, C. Bruder, *et al.*, Superlattices Microstruct. **25**, 1251 (1999).
20. C. W. J. Beenakker, Phys. Rev. Lett. **67**, 3836 (1991).
21. I. S. Gradshteyn and I. M. Ryzhik, *Table of Integrals, Series, and Products* (Nauka, Moscow, 1971; Academic, New York, 1980).
22. Yu. V. Nazarov, Phys. Rev. Lett. **73**, 134 (1994).
23. O. N. Dorokhov, Solid State Commun. **51**, 381 (1984).

JETP Letters, Vol. 75, No. 12, 2002, pp. 651–658. Translated from Pis'ma v Zhurnal Éksperimental'noĭ i Teoreticheskoĭ Fiziki, Vol. 75, No. 12, 2002, pp. 777–785.

Chaos, Fractals, and Atomic Flights in Cavities

S. V. Prants

Il'ichev Pacific Oceanological Institute, Far East Division, Russian Academy of Sciences, ul. Baltiĭskaya 43, Vladivostok, 690041 Russia

Received April 25, 2002

A semiclassical study is carried out of the nonlinear interaction dynamics between two-level atoms and a standing-wave field in a high-finesse cavity. As a result of atomic movement or wave amplitude modulation, a dynamic local instability occurs in a strongly coupled atom–field system. The appearance of dynamical Hamiltonian chaos, fractals, and Lévy flights is demonstrated for the models of two experimental devices: a (micro)maser with thermal Rydberg atoms and a microlaser with cold atoms. Numerical simulation showed that the manifestations of classical chaos, atomic fractals, and flights can be observed in the appropriate real experiments. Attention is drawn to the prospects provided by work on the atom–field systems in the coupling-modulated high-finesse cavities for further investigation of the quantum–classical correspondence, quantum chaos, and decoherence. © *2002 MAIK "Nauka/Interperiodica".*

PACS numbers: 05.45.Mt; 42.50.Vk; 32.80.Pj

1. Atoms with long-lived operating transition states and a field mode of a high-finesse cavity form a strongly coupled nonlinear dynamical system with excitation exchange. A simple Jaynes–Cummings model accounts for the coherent periodic lossless excitation exchange [1]. Virtual processes [2], external perturbation [3, 4], and standing-wave modulation in a cavity [5, 6], generally speaking, destroy the periodicity and may induce Hamiltonian chaos in the semiclassical limit. The deterministic (dynamical) chaos in classical systems manifests itself by the exponentially fast divergence of the initially close trajectories in a closed phase-space domain. Quantum evolution is unitary, and no *bona fide* quantum chaos, in the sense of exponential instability, say, of the states in a finite quantum system can occur. However, measurements break the unitary evolution of quantum systems and show evidence of classical chaos, provided that the classical analog of the quantum system is chaotic. On the other hand, quantum evolution can suppress classical chaos and manifest itself in the dynamical localization and tunneling effects. These phenomena have been actively studied with atoms and photons in cavities and traps [7]. A strongly coupled atom–field system in a high-finesse cavity is an ideal object for the fundamental tests of quantum mechanics [8] (superposition principle, nonlocality, teleportation, wave-function collapse, nondemolition measurements, etc.) and for studying the quantum–classical correspondence, one of whose aspects amounts to the problem of quantum chaos [9].

Let us consider a system of N identical two-level atoms prepared by laser excitation with a given internal energy and using a velocity selector with a given motion velocity. Such a monokinetic "droplet" is injected into a high-finesse single-mode cavity, whereupon the internal atomic energy, time of flight through the cavity, and atomic velocity are measured at the cavity output. The condition for the strong coupling regime is expressed by the inequality $\Omega_0\sqrt{N} \gg T_a^{-1}, T_f^{-1}$, where $T_{a,f}$ are, respectively, the atomic and field relaxation times and Ω_0 is the amplitude of atom–field coupling coefficient (vacuum Rabi frequency). In the strong-coupling regime, oscillations arise as a result of multiple interaction exchange between the atoms and the field of their own radiation maintained by the high-finesse cavity. This process was observed experimentally even for single atoms and photons [8, 10].

In this work, two types of experimental devices are considered: a Rydberg atom maser and a microlaser. The first deals with the thermal highly excited (Rydberg) atoms with long-lived ($T_a \simeq 10^{-2}$ s) operating transition states and a giant electric dipole transition moment ($d_a \simeq 10^3$ a.u.). The superconducting microwave cavity of a Rydberg maser has a very high Q-factor ($Q \simeq 10^9$–10^{10}) and is distinguished by weakly relaxing photons in the cavity ($T_f \simeq 10^{-3}$–10^{-2} s). Due to the high atomic moment and despite the macroscopic dimensions of the cavity ($L \simeq 1$–10 cm), the vacuum frequency is on the order of $\Omega_0 \simeq 2\pi \times 10^5$ Hz, which is sufficient for establishing the strong-coupling regime [8]. In microlasers, conventional cooled atoms and high-finesse Fabry–Pérot cavities of micron size ($Q \simeq 10^5$–10^6), in which the vacuum Rabi frequency is as high as $\Omega_0 \simeq 2\pi \times 10^8$ Hz, are used [10].

When moving along the cavity axis r, atoms intersect the nodes and antinodes of the standing wave described by a certain function $f(r)$. The atom–field-coupling coefficient is modulated by the standing wave

with the frequency $k_f v_a$, where v_a is the atomic velocity. The simplest model Hamiltonian of this problem has the following form in the rotating-wave approximation:

$$\hat{H} = \frac{\hat{P}^2}{2m} + \hbar\omega_a \hat{R}_z + \hbar\omega_f \hat{a}^\dagger \hat{a} + \hbar\Omega_0 f(r)(\hat{a}^\dagger \hat{R}_- + \hat{a}\hat{R}_+), \quad (1)$$

where the collective operators of atomic momentum $\hat{P} = \sum_j \hat{p}_j$, of internal atomic energy $\hat{R}_z = \frac{1}{2}\sum_j \hat{\sigma}_z^j$, and of atomic dipole moment $\hat{R}_\pm = \sum_j \hat{\sigma}_\pm^j$, obeying the usual commutation rules $[\hat{R}_+, \hat{R}_-] = 2\hat{R}_z$ and $[\hat{R}_z, \hat{R}_\pm] = \pm\hat{R}_\pm$, and the operators of a single-mode field with the commutator $[\hat{a}, \hat{a}^\dagger] = 1$ are introduced. In this work, an essentially semiclassical approach is used in the description of the nonlinear dynamics for the coupled atom–field system with Hamiltonian (1). In the Heisenberg representation, a closed finite set of equations of motion is derived for the expectation values of the operators of characteristic quantities.

2. Thermal Rydberg atoms in a microwave cavity. Since the recoil energy of an atom emitting microwave photons is very low, a change in the kinetic energy in Hamiltonian (1) is ignored in this section (Raman–Nath approximation). Rydberg atoms fly through a high-finesse single-mode microwave cavity with the mode function $f(r) = \sin k_f r$ with a constant velocity v_a and emit and absorb photons. In this case, the atomic interaction with the radiation field is periodically modulated with frequency $k_f v_a$ by the standing wave. By factorizing the Heisenberg equations for the operators $\hat{a}^\dagger \exp(-i\omega_f t) \pm \hat{a}\exp(i\omega_f t)$, $\hat{R}_- \exp(i\omega_f t) \pm \hat{R}_+ \exp(-i\omega_f t)$, and $\hat{R}_z$, one arrives at the following closed system of Maxwell–Bloch equations

$$\dot{x} = \delta y - zy\sin\beta\tau, \quad \dot{y} = -\delta x - ze\sin\beta\tau, \quad \dot{z} = (xp + ye)\sin\beta\tau, \quad \dot{e} = -y\sin\beta\tau, \quad \dot{p} = -x\sin\beta\tau, \quad (2)$$

for the real averages

$$x = \frac{1}{N}\langle \hat{R}_- \exp(i\omega_f t) + \hat{R}_+ \exp(-i\omega_f t)\rangle,$$

$$y = \frac{i}{N}\langle \hat{R}_- \exp(i\omega_f t) - \hat{R}_+ \exp(-i\omega_f t)\rangle,$$

$$e = \frac{1}{\sqrt{N}}\langle \hat{a}^\dagger \exp(-i\omega_f t) + \hat{a}\exp(i\omega_f t)\rangle, \quad (3)$$

$$p = \frac{i}{\sqrt{N}}\langle \hat{a}^\dagger \exp(-i\omega_f t) - \hat{a}\exp(i\omega_f t)\rangle,$$

$$z = \frac{2}{N}\langle \hat{R}_z\rangle.$$

Note that the system of Eqs. (2) is different from the Maxwell–Bloch equations in the problem considered in [3, 4] in that it is written in the coordinate system rotating with frequency ω_f and normalized in time to the value $\Omega_0\sqrt{N}$. The parameter $\delta = (\omega_f - \omega_a)/\Omega_0\sqrt{N}$ is the normalized detuning and $\beta = k_f v_a/\Omega_0\sqrt{N}$ is the normalized modulation frequency caused by the atomic movement through the nodes and antinodes of the standing wave. The length of Bloch vector and the excitation number density are independent integrals of motion for Eqs. (2):

$$x^2 + y^2 + z^2 = 1, \quad W = e^2 + p^2 + 2z = 2(2n + z), \quad (4)$$

where n is the mean number of photons in the mode. Introduce new variables

$$u = \frac{1}{N\sqrt{N}}\langle \hat{a}^\dagger \hat{R}_- + \hat{a}\hat{R}_+\rangle = \frac{1}{2}(xe - yp), \quad v = \frac{i}{N\sqrt{N}}\langle \hat{a}^\dagger \hat{R}_- - \hat{a}\hat{R}_+\rangle = \frac{1}{2}(xp + ye), \quad (5)$$

which have, respectively, a meaning of the oscillation amplitude of atom–field interaction energy density and the rate of atomic population inversion density z. Using the integrals of motion (4), the five-dimensional system of Maxwell–Bloch equations (2) reduces to three equations

$$\dot{u} = \delta v, \quad \dot{v} = -\delta u - \frac{1}{2}(Wz - 3z^2 + 1)\sin\beta\tau, \quad \dot{z} = 2v\sin\beta\tau, \quad (6)$$

which can be called the nonlinear Bloch equations with the invariant $4(u^2 + v^2) + Wz^2 + 2z - 2z^3 = W$. Thus, a comparatively simple nonlinear dynamical system with one-half degrees of freedom underlies the dynamics of a Rydberg atom maser. For the atoms which are at rest or moving in the direction along which the cavity field is spatially uniform, i.e., for $\sin\beta\tau = 1$, Eqs. (6) have an additional independent integral of motion $C = 2u - \delta z$, and the equation for z

$$\ddot{z} = -\frac{\delta}{2}(C + \delta z) - \frac{1}{2}(Wz - 3z^2 + 1) \quad (7)$$

can be integrated in terms of elliptic functions. At the exact resonance ($\delta = 0$), the quantity $u = u_0$ is a constant for an arbitrary modulation of the vacuum Rabi frequency. The equation for inversion has the form

$$\dot{z} = \pm\sqrt{W - 4u_0 - Wz^2 - 2z + 2z^3}\sin\beta\tau \quad (8)$$

and can be exactly solved in terms of elliptic functions [4]. For a large detuning, $|\delta| \gg 1$, the smallness of the variable v and, hence, the smallness of the change in inversion z in the course of evolution follows from the simple considerations about the smallness of the $\delta^{-1}\dot{u}$

value. As a result, the variable u approximately satisfies a simple harmonic oscillator equation with a driving force. For the low modulation frequency, $\beta \ll 1$ (slow atoms), one has an approximate additional integral of motion $2u\sin\beta\tau - \delta z \simeq \text{const}$. These oscillations represent a virtually regular signal with weak amplitude and frequency modulations. In the opposite limit, $\beta \gg 1$, i.e., where the atomic velocity is so high that the modulation frequency far exceeds the Rabi frequency, the Rabi oscillations are the slow regular z oscillations superposed by the fast oscillations with frequency β and small amplitude $1/\beta^2$.

The analysis of chaos initiation in a strongly coupled semiclassical atom–field system in a cavity was carried out in a number of works [4, 6, 11, 12] for various mechanisms of modulation of the coupling coefficient. It is based on the Melnikov method of solving nonautonomous dynamical systems in the vicinity of their unperturbed invariant sets. The Maxwell–Bloch Eqs. (2) have two stationary points $S_\pm$ ($x_s = y_s = e_s = p_s = 0, z_s = \pm 1$), which correspond to the stationary points of the nonlinear Bloch Eqs. (6) ($u_s = v_s = 0, z_s = \pm 1$). In the absence of modulation, these points in the z–v plane are connected by a closed separatrix, whose stable and unstable saddle-point sets S_+ coincide. The modulation caused by one or other physical mechanism results in the splitting of this homoclinic set into two surfaces intersecting transversally infinitely many times in the respective Poincaré sections. It is this mechanism of formation of a highly intricate homoclinic pattern in the vicinity of the unperturbed separatrix which is responsible for the chaos initiation in the atom–field systems with modulation. The distance between the stable and unstable sets of saddle singular point S_+ determines the width of a stochastic layer appearing at the site of the unperturbed separatrix. For our system, this quantity, as calculated by the Melnikov method, has the form

$$M(\tau) \simeq \frac{2\pi|\delta|\beta^2}{\sinh(\pi\beta/\sqrt{4-|\delta|^2})}\cos\beta\tau. \qquad (9)$$

From this formula, several important conclusions can be drawn. The distance between the split surfaces changes sign with modulation frequency β, and hence, these surfaces intersect transversally infinitely many times. This occurs for β values as small (or large) as desired, although the width of stochastic layer decreases exponentially fast for small and large β. As expected, the surfaces do not split at the exact resonance $\delta = 0$, and the motion is fully regular.

Chaos in the deterministic systems is primarily characterized by the exponential sensitivity of motion to small changes of initial conditions. A measure of this sensitivity is given by the Lyapunov exponent

$$\lambda = \lim_{\tau\to\infty}\lambda(\tau), \quad \lambda(\tau) = \lim_{\Delta(0)\to 0}\frac{1}{\tau}\ln\frac{\Delta(\tau)}{\Delta(0)}, \qquad (10)$$

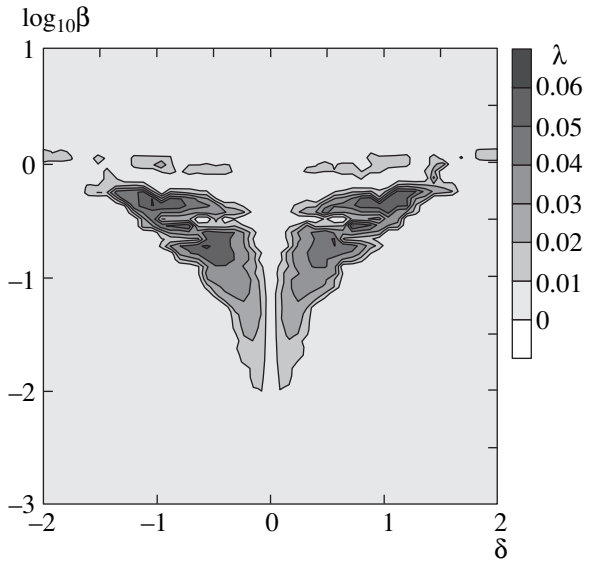

Fig. 1. The maximal Lyapunov exponent λ for Eq. (2) vs. the logarithm of velocity β of thermal atoms (in units of $\Omega_0\sqrt{N}/k_f$) and the detuning δ (in units of $\Omega_0\sqrt{N}$).

where $\Delta(\tau)$ is the distance (in the Euclidean sense), at the instant of time τ, between two trajectories that were close to each other at $\tau = 0$. The number of Lyapunov exponents is equal to the dimensionality of the system. If the maximal Lyapunov exponent is larger than zero, the element of phase volume increases exponentially fast in the respective direction (and decreases in the other direction, because the phase volume of the conservative system is an invariant).

The topographic maps of the maximal Lyapunov exponent were calculated in our works [3, 4–6, 11, 13, 14] for atom–field systems with various modulation variants. Figure 1 shows the λ map for the Rydberg atom maser obeying equations of motion (2) with the initial state $x_0 = y_0 = 0, z_0 = 1, e_0 = p_0 = 1$ corresponding to the fully excited atoms at the cavity input and the photon mean number density $n_0 = \frac{1}{2}$ at $\tau = 0$. The gray-shadowed regions correspond to the positive values of the maximal Lyapunov exponent in the corresponding ranges of both driving parameters (detuning δ and modulation frequency β). The range of most unstable Rabi oscillations of moving atoms is given by $|\delta| \lesssim 2$ and $0.01 \lesssim \beta \lesssim 2$. Inasmuch as the initial atomic and field values can be measured with only a finite accuracy (say, equal to Δz_{in} for the population inversion at the cavity input), the atomic states at the output can be predicted, within a certain confidence interval Δz, for a time not exceeding the so-called predictability horizon (correlation uncoupling time):

$$\tau_c \simeq \frac{1}{\lambda}\ln\frac{\Delta z}{\Delta z_{\text{in}}}, \qquad (11)$$

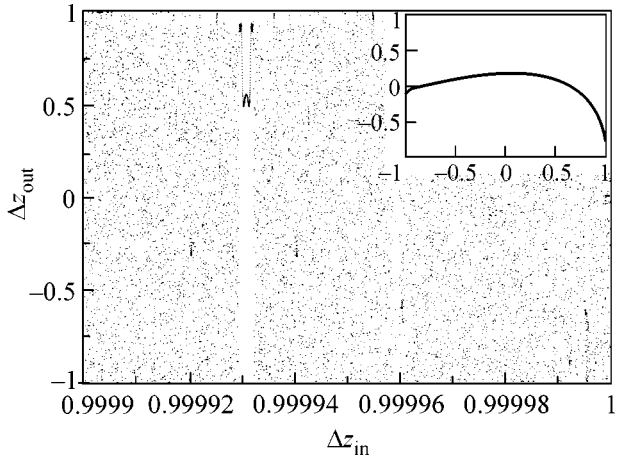

Fig. 2. Chaotic spreading of a small uncertainty $\Delta z_{in} = 10^{-4}$ in the atomic population inversion at the cavity input over the entire interval Δz_{out} of allowable values at the output ($\beta = 0.1$ and $\delta = 0.5$). Inset: regular dependence $\Delta z_{in}(\Delta z_{out})$ at the exact resonance ($\beta = 0.1$ and $\delta = 0$).

which shows very weak dependence on Δz_{in} and Δz and, hence, is as representative a characteristic of the system as the Lyapunov exponent. Since the maximal confidence interval lies in the range $|z| \le 1$, while $\lambda_{max} \simeq 0.1$, the predictability horizon of a Rydberg atom maser can be $\tau_c \simeq$ 20–30 dimensionless units or ≃20–30 Rabi oscillations.

A Rydberg atom maser is a promising device for observing the manifestations of dynamical chaos in the fundamental process of interaction between radiation and substance. Imagine experiments that are repeatedly carried out at the same conditions with the atomic ensemble prepared by a laser π-pulse in a collective excited state with $z_{in} \simeq 1$. The atomic state at the output, z_{out}, can be measured using the high-sensitivity selective atomic ionization technique [8]. The inevitable errors Δz in preparing the initial atomic state in the regular maser operation mode produce the output errors Δz_{out} of the same order. In the chaotic regime, the initial uncertainty increases exponentially, resulting in a complete uncertainty of the atomic output states in a reasonable time. The dimensionless atomic-flight time with a constant velocity v_a through a microwave cavity of length $L = m\lambda_f$ (m is the number of wavelengths) is $\tau_{out} = 2\pi m/\beta$. From Eq. (11), it follows that even a negligible initial error $\Delta z_{in} = 10^{-4}$ of atomic state would lead to a complete uncertainty $\Delta z_{out} \simeq 2$ at the output in time $\tau \simeq 200$ for $\lambda \simeq 0.05$. If $\Delta z_{in} = 10^{-2}$, then the probability of obtaining any value of z_{out} in the interval [–1, 1] is almost unity in time $\tau \simeq 100$. To feel the difference, it will suffice to carry out a control experiment at the exact resonance ($\delta = 0$), for which the motion is fully regular with any initial value and any atomic velocity. These considerations are illustrated in Fig. 2, where the dependence $\Delta z_{out}(\Delta z_{in})$ is shown for very small $\Delta z_{in} = 10^{-4}$ in the chaotic regime with $\lambda \simeq 0.04$. For comparison, the same dependence is demonstrated in the inset for $-1 \le \Delta z_{in} \le 1$ in the regular regime with $\delta = 0$, all other things being the same.

Let us discuss the characteristics of the chaotic regime that are expected for real Rydberg atom masers. In a high-finesse superconducting cavity with $Q \simeq 10^8$ and $L \simeq$ 1–10 cm, the vacuum frequency of the Rydberg atoms reaches $\Omega_0 \simeq 2\pi \times 10^5$ Hz [8]. For $N = 10^6$ Rydberg atoms, the period of collective oscillations is $T_R = 2\pi/\Omega_0\sqrt{N} \simeq 10^{-8}$ s, which is appreciably lower than all decoherence times. In the detuning range $|\delta| \lesssim 2$, the positive maximal Lyapunov exponent on the order of $0.005 \lesssim \lambda \lesssim 0.1$ was obtained numerically in the interval of dimensionless modulation frequency $0.01 \lesssim \beta \lesssim 1$, which corresponds to the atomic velocities $10^6 \lesssim v_a = 10^8\beta \lesssim 10^8$ cm/s. An atom with velocity $v_a \simeq 5 \times 10^6$ cm/s flies through a 10-cm cavity in a time on the order of 2 μs, which amounts to approximately $\tau_{out} \simeq$ 200 dimensionless units. Our calculations show that the complete mixing occurs in approximately the same time, so that any output value z_{out} is equally probable.

Let us dwell briefly upon the simplest, in our opinion, experimental scheme for observing the manifestations of semiclassical chaos with atoms in cavities. The idea is to periodically switch on and off the field in a cavity according to a certain law $f(t)$. Taking this modulation in the form $f(t) = \sin^2\omega_m t$ and assuming, for simplicity, that the atom flies along the cavity axis, where the field is uniform, one can use almost all the results presented above. The Maxwell–Bloch equations have the form of Eqs. (2), in which one should replace $\sin\beta\tau \longrightarrow \sin^2\beta_1\tau_1$, where $\tau_1 = \Omega_0 t$ is the new measure of time and $\beta_1 = \omega_m/\Omega_0$ is the dimensionless modulation frequency. Calculations show that the maximal Lyapunov exponent is positive in the same ranges of modulation frequency and detuning as in Fig. 1 but is somewhat smaller. One can expect that the manifestation of chaos occurs with a *single atom* if the frequency of switching on and off $\omega_m = \beta_1\Omega_0$ lies in the range $(0.01–1)\Omega_0$ Hz. The resulting "spread" of a small initial inversion uncertainty has the same character as in Fig. 2. Below, some estimates are given for the Rydberg atom micromasers (although a similar experiment is possible for ordinary atoms in a microcavity). Let the period of vacuum Rabi oscillations of one atom be $T_1 = 2\pi/\Omega_0 \simeq 2 \times 10^{-5}$ s and the field modulation period be $T_m = 2\pi/\omega_m \simeq 2 \times 10^{-4}$ s (i.e., $\beta_1 \simeq 0.1$). If the inversions of atoms entering the cavity one by one lie in the range $\Delta z_{in} \simeq 0.01$, then, for the detuning $|\delta| \simeq 1$, *any* output atomic state Δz_{out} becomes almost equally probable in the interval [–1, 1] at $t \simeq 2 \times 10^{-3}$ s, i.e., at $v_a \simeq 10^3$ cm/s and $L \simeq 2$ cm. The advantages of operating with a single atom are evident, because there is no need to take care

of producing monokinetic droplets consisting of many identically prepared atoms. Except for the pulsed cavity field, the scheme and parameters of the suggested experiment are quite standard (see [8]).

We also considered the variants of driving-parameter modulation for the quiescent atoms in a high-finesse cavity. In [5], the parametric exponential instability and the Hamiltonian chaos were observed for the Maxwell–Bloch equations with detuning modulation. The topographical λ maps showed a well-defined correlation of the chaos zones and the zones of different-order parametric resonances. In [6], a semiclassical model of atom–field interaction with the modulation of standing-wave node positions was analyzed, which can be implemented using an electro-optical modulator by changing cavity length. The Maxwell–Bloch equations have practically the same form as Eqs. (2) with the modulation function $1 + a\sin b\tau$, and their solutions are most unstable in approximately the same ranges of dimensionless detuning and modulation frequency b as for the moving atoms.

3. Cold atom in a Fabry–Pérot microcavity. The recoil energy of sufficiently cold atoms interacting with visible light is comparable to their kinetic energy. In this section, the nonlinear dynamics is described for a simple semiclassical model of interaction between a cold atom and a given mode of a high-finesse Fabry–Pérot microcavity. Let us choose the following quantum expectation values as dynamical variables: $\xi = k_f\langle\hat{x}\rangle$, $\rho = \langle\hat{p}\rangle/\hbar k_f$, $u = \langle\hat{a}^\dagger\hat{\sigma}_- + \hat{a}\hat{\sigma}_+\rangle$, $v = i\langle\hat{a}^\dagger\hat{\sigma}_- + \hat{a}\hat{\sigma}_+\rangle$, and $z = \langle\hat{\sigma}_z\rangle$. Then one obtains the following closed system of equations of motion from Hamiltonian (1) with $N = 1$ and mode function $f(r) = -\cos k_f r$[15]:

$$\begin{aligned}\dot{\xi} &= \alpha\rho, \quad \dot{\rho} = -u\sin\xi, \quad \dot{u} = \delta v,\\ \dot{v} &= -\delta u + \left[(2N_0 - 1)z - \frac{3}{2}z^2 + \frac{1}{2}\right]\cos\xi, \qquad (12)\\ \dot{z} &= -2v\cos\xi,\end{aligned}$$

where the dot stands for the differentiation with respect to the dimensionless time $\tau = \Omega_0 t$, and the driving parameters $\alpha = \hbar k_f^2/m\Omega_0$, $\delta = (\omega_f - \omega_a)/\Omega_0$, and $N_0 = \langle\hat{a}^\dagger\hat{a} + (\hat{\sigma}_z + 1)/2\rangle$ are the normalized atomic recoil frequency, the normalized resonance detuning, and the number of excitations, respectively. The system of Eqs. (12) generalizes the corresponding equations in [16, 17] to the case of arbitrary N_0. The integral of motion

$$E = \frac{\alpha\rho^2}{2} - u\cos\xi - \frac{\delta}{2}z \qquad (13)$$

reflects the energy conservation in the system.

At the exact resonance ($\delta = 0$), the slow translational variables ξ and ρ are separated from the fast atom– field variables u, v, and z. As a result, the system of equations acquires an additional conservation law $u = \text{const}$ and becomes integrable. The atom moves in the spatially periodic optical potential $u_0\cos\xi$, so that the motion of its center of mass obeys the simple equation $\ddot{\xi} + \alpha u_0\sin\xi = 0$. Depending on the energy E, the atom executes either the regular oscillations in a potential well or regular flight above the tops of potential hills. The atomic population inversion satisfies the equation of type (8) and represents a regular Rabi-oscillation signal modulated by the standing wave. In the case of nonzero detuning, the translational motion obeys the equation

$$\ddot{\xi} + \alpha u(\tau)\sin\xi = 0, \qquad (14)$$

where u is the function of time and all dynamical variables of the system. For the chaos to arise upon the atomic motion in the cavity with standing wave, the simplest harmonic oscillations of u with time are sufficient. Taking into account that the normalized Rabi frequency has the order of $\sqrt{\delta^2 + N_0} > 1$, which far exceeds the frequency of small translational oscillations $\sim\sqrt{\alpha u_0}$, the equations for the fast variables of the system of Eqs. (12) with $N_0 \gg 1$ reduce to linear equations of the Bloch type

$$\begin{aligned}\dot{u} &= \delta v, \quad \dot{v} = -\delta u + 2N_0 z\cos\xi,\\ \dot{z} &= -2v\cos\xi,\end{aligned} \qquad (15)$$

in which the function $\cos\xi$ can be set equal to a constant c on the time interval of many Rabi oscillations. The general solution to these equations for u has the form

$$\begin{aligned}u &= u_0\left[N_0\left(\frac{2c}{\Omega}\right)^2 + \left(\frac{\delta}{\Omega}\right)^2\cos\Omega\tau\right]\\ &+ \frac{\delta}{\Omega}v_0\sin\Omega\tau + \frac{2N\delta c}{\Omega^2}z_0(1 - \cos\Omega\tau),\end{aligned} \qquad (16)$$

where $\Omega = \sqrt{\delta^2 + (2c)^2 N_0}$ is the normalized Rabi frequency. For an atom fully excited at the cavity input ($z_0 = 1$) and for an arbitrary field state in the cavity ($u_0 = v_0 = 0$), the oscillation amplitude of atom–field interaction energy changes harmonically with the Rabi frequency. A nonlinear pendulum with harmonic modulation frequency (14) is the classical model for which the Hamiltonian chaos appears in the vicinity of the broken unperturbed separatrix [18]. Our calculation in [15] gives the following estimate for the width of stochastic layer:

$$\Delta \simeq 8\pi(\Omega/\omega)^3\exp(-\pi\Omega/2\omega), \qquad (17)$$

where $\omega = \sqrt{2\alpha N_0|\delta|}/\Omega$. The quantity Δ is a change in the unperturbed motion energy normalized to the separatrix value $E_s = \omega^2$. In our case, $\Omega/\omega \gg 1$. Note that Eq. (17) gives the lower bound for the layer width,

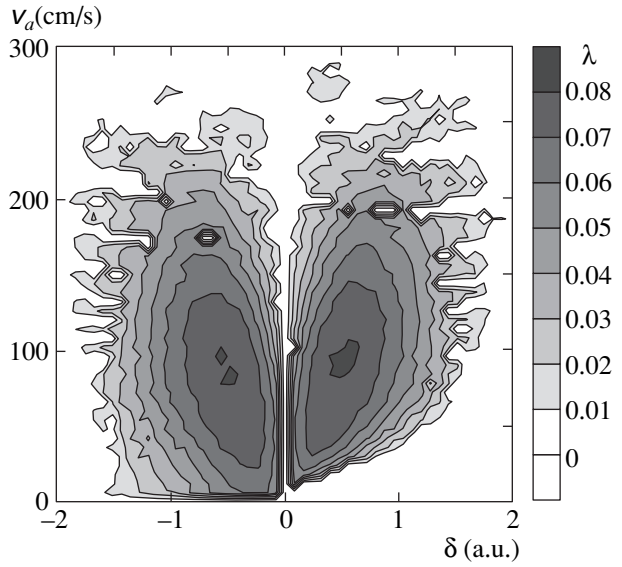

Fig. 3. The maximal Lyapunov exponent λ for Eq. (12) vs. the initial velocity v_a of a cold atom (in cm/s) and the detuning δ (in units of Ω_0).

because, generally, u is not a harmonic but a frequency- and amplitude-modulated signal. Small changes of energy give rise to relatively small changes in frequency. For motion energy that is much lower or much higher than E_s (i.e., near the potential well bottoms or high above the tops of potential hills), small changes in frequency give rise to small changes in phase during the period of translational oscillations. However, near the unperturbed separatrix, where the oscillation period tends to infinity, even small changes in frequency can result in considerable changes in phase. This is the reason for the exponential motional instability of the parametric nonlinear oscillator (14) and, hence, for the chaotic atomic motion in the field of a periodic standing wave.

Numerical simulations confirm these premises. Figure 3 shows the λ map as a function of detuning δ and initial atomic velocity v_a (cm/s) for $N_0 = 10$ and $\alpha = 10^{-3}$. The calculation of other λ maps in the coordinates v_a–α, v_a–δ, z_0–v_a, and α–N_0 allowed us to determine the ranges of driving parameters and initial conditions for which one could expect the maximal motional instability of real atoms in the microcavities: $\alpha \gtrsim 10^{-3}$, $N_0 \lesssim 10^2$, and $|\delta| \lesssim 2$. The strong-coupling condition $\Omega_0 T_{a,f}/2\pi \gtrsim 10^2$ is fulfilled in the visible range for the metastable 2S–2P transitions in helium and magnesium and the 3S–3P transition in calcium [19] placed in a high-finesse Fabry–Pérot cavity of micron size with $Q \gtrsim 10^6$ and $\Omega_0/2\pi \simeq 10^8$ Hz [10]. In experiments [10] with cold atoms, the authors managed to create an atomic trap in the field of a single photon in such cavities and to detect long atomic flights and small atomic oscillations in the potential well. Note that the observation time in these experiments far exceeded the relaxation times.

4. Atomic fractals and flights. A typical chaotic trajectory of a cold atom in a cavity consists of intervals of constant motion of different length (so-called Lévy flights) interrupted by random walks. Such an intermittency is typical of Hamiltonian systems with nonhomogeneous phase space. The Lévy flights appear due to the presence of "islands," to whose boundaries the chaotic trajectory can "stick" in the phase space for a rather long time. In the closed Hamiltonian system with nonhomogeneous phase space, the representative point on the chaotic trajectory sooner or later approaches, as closely as desired, the invariant curve (island boundary) that separates the regular and chaotic motions. Near this boundary, $\lambda \longrightarrow 0$, and the partially broken KAM tori (cantori) block the trajectory escape to the stochastic "sea." As a result, the trajectory very slowly moves away from the island boundary. It is worth noting that the Lévy flights occur not only with particles moving in the coordinate space. In the space of internal atomic and field coordinates, they appear as long portions of regular oscillations of these coordinates. We observed such flights in the Rabi signals from both cold and hot atoms flying with a constant velocity. Note that in the Rabi oscillations of atoms moving through the standing wave and quiescent atoms in the cavity with length modulation, structures arise which are associated with the presence of standing-wave nodes, in which the vacuum Rabi frequency is zero. These structures are clearly seen both in the signal [20] and in its wavelet spectra, giving grounds to call this chaos structural chaos [6, 12, 21].

The intermittency, the Lévy flights, and the structures fundamentally change the statistical properties of the chaotic motion [22, 23]. The motion predominantly in the region with complete mixing leads to normal diffusion and to exponential Gaussian and Poissonian distribution functions for the spatial and temporal diffusion, respectively. The intermittency gives rise to the anomalous diffusion described by the Lévy distribution functions with a power-law decrease at their wings and, hence, with infinite moments. It was found by computer simulation [24] that the positions of a cold atom in the optical potential evolve with time following the law $\langle \xi^{2m} \rangle \sim \tau^{\mu(m)}$, where the transport exponent $\mu(m)$ is, in the general case, different for different time intervals. With normal diffusion, the transport exponent for the second moment is unity; i.e., $\mu(1) = 1$. The Lyapunov exponent λ depends on the detuning δ (Fig. 3), and its value is a suitable measure of mixing in the system. For a relatively large λ ("good mixing"), the asymptotic value $\mu(1) \approx 1.13$ is close to the normal value. For small λ and weak mixing, the asymptotic value $\mu(1) \approx 2.2$ was found to correspond to the superdiffusion, i.e., to the ballistic atomic motion with acceleration. Figure 4 illustrates the evolution of several moments $\langle |\xi^{2m}| \rangle$ for $\lambda \simeq 0.02$ (the slopes of the lines are given for $\tau \gtrsim 10^3$) [24].

In the superdiffusion regime, the self-similarity is clearly seen; i.e., $\mu(km) = k\mu(m)$ for $k = 1, 2, 3$, and 4.

According to the Poincaré theorem, every trajectory of a closed conservative dynamical system (except for the trajectories of the set of measure zero) returns to an arbitrary vicinity of its initial point infinitely many times. The recurrence time distribution is a representative statistical characteristic of chaotic motion. For good mixing, the distribution is Poissonian, $P(\tau) = h^{-1}\exp(-h\tau)$, where h is the Kolmogorov–Sinai entropy. The motion with intermittency and Lévy flights leads to the power law, $P(\tau) \sim \tau^{-\gamma}$ at $\tau \longrightarrow \infty$. The algebraic asymptotic behavior of the Poincaré recurrence times is shown in the inset in Fig. 4 for the long atomic Lévy flights with $\gamma \gtrsim 2$. The exponents γ and μ are related to each other.

The intermittent chaotic dynamics with Lévy flights gives rise in the Hamiltonian system to the trajectories with fractal properties. Let two atomic counters be placed at the cavity input and output and let them detect the time τ_d of atom departure from the cavity. Let the atoms with given initial momenta ρ_0 (all other things being the same) be placed one by one in the middle of the cavity, and calculate the $\tau_d(\rho_0)$ dependence. This function has an obviously fractal character. Along with the regions of ρ_0 values where it is smooth, there are regions where $\tau_d(\rho_0)$ can by no means be resolved. These properties repeat for the initial momentum resolution as small as desired (Fig. 5). The fact that the curve becomes more complicated with a decrease in the sampling interval ϵ is the consequence of atomic dynamics in the optical potential rather than of the resolution. Evaluation of the curve "length" $T = \sum_i |\tau_{d,i+1} - \tau_{d,i}|$ as a function of ϵ yields the function $T(\epsilon) \sim \epsilon^{-d}$, where $d \simeq 0.84$ has the meaning of fractal dimension. The properties of this fractal are the subject of a separate study [25].

It should be emphasized that the random walk with Lévy flights appears in a fully deterministic system. The spontaneous radiation process, in which the atomic momentum changes chaotically, should seemingly be a Gaussian process. However, this is not necessarily so. In the experiments [26] on cooling atoms down to the energies lower than the recoil energy, Lévy statistics were observed, in which long intervals of constant momentum alternated with random jumps. The probability of an atom being held in a close vicinity of $\rho = 0$ for time τ represents a broad distribution decreasing at its wings following such a slow power law that the average time $\langle\tau\rangle$ diverges.

The two-level atoms in high-finesse cavities are ideal objects for studying the interrelation between the micro-, meso-, and macrocosms. By changing the number of atoms (photons), the resonance detuning, the spontaneous radiation rate, etc., one can pass from the dynamical regimes, in which the quantum effects are significant, to the regimes that are essentially classical.

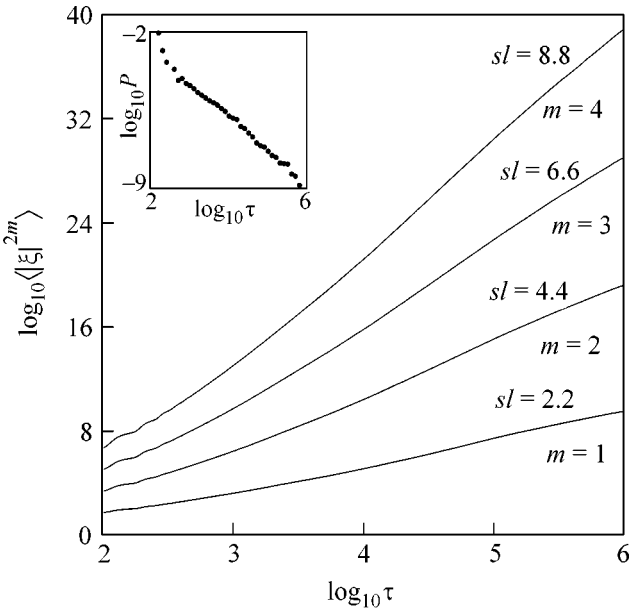

Fig. 4. Log–log plot of the evolution of moments $\langle|\xi|^{2m}\rangle$ of the coordinate of cold atom. Inset: the Poincaré recurrence time distribution.

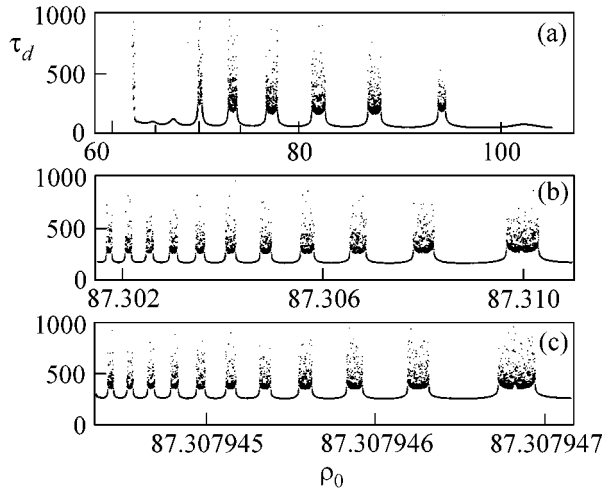

Fig. 5. Time τ_d of cold atom departure from the cavity (in units $1/\Omega_0$) vs. the atomic initial momentum (in units $\hbar k_f$) for the sequentially increasing resolution.

In this review, only the semiclassical conservative atom–field systems have been discussed. A further problem consists in the quantum description of these systems and the comparison of the semiclassical and quantum results on the regular dynamics and classical chaos. Of special interest is revealing how the noise and dissipation (mainly spontaneous radiation) influence the quantum dynamics, because they can destroy quantum interference and exhibit traces of dynamical chaos in the corresponding classical analog.

I am grateful to my collaborators L.E. Kon'kov, V.Yu. Sirotkin, and M.Yu. Uleĭskiĭ for assistance in numerical computations. This work was supported by the Russian Foundation for Basic Research, project nos. 99-02-17269 and 02-02-17796.

REFERENCES

1. E. T. Jaynes and F. W. Cummings, Proc. IEEE **51**, 89 (1963).
2. P. I. Belobrov, G. M. Zaslavskiĭ, and G. Kh. Tartakovskiĭ, Zh. Éksp. Teor. Fiz. **71**, 1799 (1976) [Sov. Phys. JETP **44**, 945 (1976)].
3. S. V. Prants and L. E. Kon'kov, Phys. Lett. A **225**, 33 (1997).
4. S. V. Prants, L. E. Kon'kov, and I. L. Kirilyuk, Phys. Rev. E **60**, 335 (1999).
5. S. V. Prants and L. E. Kon'kov, Zh. Éksp. Teor. Fiz. **115**, 740 (1999) [JETP **88**, 406 (1999)].
6. V. I. Ioussoupov, L. E. Kon'kov, and S. V. Prants, Physica D (Amsterdam) **155**, 311 (2001).
7. F. L. Moore, J. C. Robinson, C. F. Bharucha, *et al.*, Phys. Rev. Lett. **75**, 4598 (1995).
8. J. M. Raimond, M. Brune, and S. Haroche, Rev. Mod. Phys. **73**, 565 (2001); B. T. H. Varcoe, S. Brattke, M. Weidinger, and H. Walther, Nature **403**, 743 (2000).
9. B. Chirikov, Open Syst. Inf. Dyn. **4**, 241 (1997).
10. C. J. Hood, T. W. Lynn, A. C. Doherty, *et al.*, Science **287**, 1447 (2000); P. Münstermann, T. Fischer, P. Maunz, *et al.*, Phys. Rev. Lett. **82**, 3791 (1999).
11. S. V. Prants and L. E. Kon'kov, Phys. Rev. E **61**, 3632 (2000).
12. S. V. Prants, Opt. Spektrosk. **90**, 782 (2001) [Opt. Spectrosc. **90**, 701 (2001)].
13. S. V. Prants, L. E. Kon'kov, and E. V. Dmitrieva, Phys. Lett. A **237**, 283 (1998).
14. L. E. Kon'kov and S. V. Prants, Pis'ma Zh. Éksp. Teor. Fiz. **65**, 801 (1997) [JETP Lett. **65**, 833 (1997)].
15. S. V. Prants, Pis'ma Zh. Éksp. Teor. Fiz. **75**, 71 (2002) [JETP Lett. **75**, 63 (2002)].
16. S. V. Prants and L. E. Kon'kov, Pis'ma Zh. Éksp. Teor. Fiz. **73**, 200 (2001) [JETP Lett. **73**, 180 (2001)].
17. S. V. Prants and V. Yu. Sirotkin, Phys. Rev. A **64**, 033412 (2001).
18. G. M. Zaslavsky, R. Z. Sagdeev, D. A. Usikov, and A. A. Chernikov, *Weak Chaos and Quasiregular Patterns* (Nauka, Moscow, 1991; Cambridge Univ. Press, Cambridge, 1991).
19. C. S. Adams, M. Sigel, and J. Mlynek, Phys. Rep. **240**, 143 (1994).
20. S. V. Prants, Phys. Rev. E **61**, 1386 (2000).
21. S. V. Prants and V. I. Yusupov, Kvantovaya Élektron. (Moscow) **30**, 647 (2000) [Quantum Electron. **30**, 647 (2000)].
22. C. F. Karney, Physica D (Amsterdam) **8**, 360 (1983); B. V. Chirikov and D. L. Schepelyansky, Physica D (Amsterdam) **13**, 394 (1984).
23. M. F. Shlesinger, G. M. Zaslavsky, and J. Klafter, Nature **363**, 31 (1993).
24. S. V. Prants, M. Edelman, and G. M. Zaslavsky, submitted to Phys. Rev. E.
25. S. V. Prants and V. Yu. Sirotkin, submitted to Phys. Rev. Lett.
26. F. Bardou, J. P. Bouchaud, O. Emile, *et al.*, Phys. Rev. Lett. **72**, 203 (1994).

Translated by V. Sakun

JETP Letters, Vol. 75, No. 12, 2002, p. 659. Translated from Pis'ma v Zhurnal Éksperimental'noĭ i Teoreticheskoĭ Fiziki, Vol. 75, No. 12, 2002, p. 786.

Comment on "Cyclotron Resonance for Electrons over Helium in a Resonator"

V. S. Édel'man

Kapitza Institute for Physical Problems, Russian Academy of Sciences, ul. Kosygina 2, Moscow, 119334 Russia

Received April 8, 2002

PACS numbers: 76.40.+b

In [1], V.B. Shikin invoked the well-known phenomenon of resonance splitting in coupled resonators to carry out a model calculation on the mutual influence of electron resonance in a magnetic field and the electromagnetic resonance system where electrons are placed for measurements. Without numerical analysis of the experimental situation occurring in [2, 3], he concluded that some features of cyclotron resonance observed in [2] for electrons localized over helium are artifacts. Below, we show that this conclusion is erroneous. Though casting no doubt on the possible mutual influence of the coupled resonance systems (this was directly stated, in particular, in Section 2 of [2]), we present once more the arguments which can be formulated upon careful reading of [2] and which prove that this mutual influence is negligible.

1. As follows from Fig. 3, the relaxation time is $\tau = 5 \times 10^{-9}$ s at $n = 10^8$ cm^{-2} and, correspondingly, the parameter $\sigma_0 = 0.05$ (Eq. (14) in [1]), i.e., is much smaller than unity. For other electron concentrations, it becomes even smaller, either because of a decrease in n with a decreasing pressing field (the τ variations are small in this case) or because of the increase in the parameter $n\tau$ in pressing fields higher than 200–300 V/cm. Therefore, the statement made in [1] does not hold.

2. In [2], special precautions were taken for weakening electron coupling to the resonator field; the electron layer was brought closer to the resonator bottom to provide a comparatively weak (at a level of 10–20%) influence of the cyclotron resonance on the resonator Q factor (see Fig. 2). It was pointed out that the electron-induced shift of resonator eigenfrequency was small and disturbed (at a fixed frequency of the measuring signal) the signal passage through the resonator only by 10%. For a Q factor of 2000 and a frequency of 18.5 GHz, this corresponds to a frequency shift of less than 1 MHz or, when recalculated to the magnetic field, less than 0.3 Oe, which is two to three orders of magnitude lesser than the observed CR shifts under the action of pressing field. This gives an estimate for the "anticrossing" in the situation considered.

3. The fact that the data presented in Fig. 4 on the resonance shifts coincide for different helium layer depths (which is varied in different experiments by approximately 1.5 times; in energy terms, this corresponds to a change in the coupling constant more than twice), different frequencies (18.5 and 37.7 GHz), and different temperatures (from 0.36 to 1.2 K) (according to Eq. (20) in [2], this is accompanied by a change in τ by an order of magnitude) by no means fits to the scheme suggested by Shikin. Note also that in [3], where the results were obtained in the range of pressing fields <600 V/cm, the CR shift is appreciably larger than in our case and corresponds, with an accuracy of 10–20%, to Eq. (15) in [2] without the constant term. This may be due to the fact that the Wigner crystallization in [3] occurs at temperatures substantially lower than in [2].

4. Both the resonance shift and its linewidth for electrons over ^{3}He and ^{4}He are inversely related to their surface tensions (Fig. 4). One can hardly suggest any explanation for this observation other than the coupling to riplons and surface deformation.

5. The study of electron heating by measuring the signal (Fig. 5) showed that the relaxation time increases with electron temperature, whereas the resonance shift drops to zero and even changes sign in some cases (this correlates with a decrease in the CR shift with a rise in temperature [3]). If the author of [1] were right, all things would be quite the reverse.

These arguments are more than sufficient for considering the results of work [1] inconsistent.

REFERENCES

1. V. B. Shikin, Pis'ma Zh. Éksp. Teor. Fiz. **75**, 31 (2002) [JETP Lett. **75**, 29 (2002)].
2. V. S. Édel'man, Zh. Éksp. Teor. Fiz. **77**, 673 (1979) [Sov. Phys. JETP **50**, 338 (1979)].
3. L. Wilen and R. Giannetta, Phys. Rev. Lett. **60**, 231 (1988).

Translated by V. Sakun

0021-3640/02/7512-0659$22.00

JETP Letters, Vol. 75, No. 12, 2002, p. 660. Translated from Pis'ma v Zhurnal Éksperimental'noĭ i Teoreticheskoĭ Fiziki, Vol. 75, No. 12, 2002, p. 787.

Reply to Comment on "Cyclotron Resonance for Electrons over Helium in a Resonator"

V. B. Shikin

Institute of Solid-State Physics, Russian Academy of Sciences, Chernogolovka, Moscow region, 142432 Russia

Received May 15, 2002

PACS numbers: 76.40.+b

In my work [1], I suggested a simple model that allows the description of the dynamics of 2D electrons in a resonator. This model can be used to explicitly renormalize the resonator eigenfrequencies in the presence of a 2D electron layer and describe the anticrossing effect in a vertical magnetic field and, what is probably most interesting, determine the influence of a 2D electron system on the transmission coefficient for an external wave passing through the electron-"loaded" resonator (a version of the Fabri–Pérot analyzer).

The anticrossing phenomenon in a system "resonator + 2D electrons" was recently observed experimentally with details following from the description given in [1]. This communication is admitted as a plenary lecture at the LT-23 Japan, 2002.

As regards signal passage through a resonator with 2D electrons, the results of [1] are also useful in interpreting the data of the interesting work [2], which was pointed out in the comments at the end of [1]. The frequency shifts observed in [2] upon loading resonator with electrons, as well as the noticeable sensitivity of the amplitude of passing the signal to the depth of the helium layer in the resonator, can serve as an independent information source about the density of 2D electron systems, if one takes into account the results of [1]. However, these effects are mentioned in [2] too briefly and without any quantitative details.

As for the principal achievement of [2], namely, the as yet unexplained quadratic dependence of the CR line shift on the pressing field, starting practically at its zero value, it may well be that the anticrossing is immaterial in this case (the author of [2] insists on this), provided that the data on electron density are valid. In fact, there are indications [3, 4] that the method used in [2] for determining the 2D electron density from a given pressing field that holds electrons near the helium surface is not unambiguous. In other works with electrons in a resonator, the authors used more complex cells in order to determine the electron density more reliably (see [5]).

REFERENCES

1. V. Shikin, Pis'ma Zh. Éksp. Teor. Fiz. **75**, 31 (2002) [JETP Lett. **75**, 29 (2002)].
2. V. S. Edelman, Zh. Éksp. Teor. Fiz. **77**, 673 (1979) [Sov. Phys. JETP **50**, 338 (1979)].
3. V. Shikin, Pis'ma Zh. Éksp. Teor. Fiz. **70**, 274 (1999) [JETP Lett. **70**, 283 (1999)].
4. A. Dyugaev, P. Grigor'ev, and Yu. Ovchinnikov, Zh. Éksp. Teor. Fiz. **117**, 1251 (2000) [JETP **90**, 1089 (2000)].
5. L. Wilen and R. Gianetta, Phys. Rev. Lett. **60**, 231 (1988).

Translated by V. Sakun

0021-3640/02/7512-0660$22.00